Advanced Friction Stir Spot Welding of Aluminum Alloy to Transformation Induced Plasticity Steel

by
Kai Chen

A dissertation submitted in partial fulfillment
of the requirements for the degree of
Doctor of Philosophy
(Mechanical Engineering)
in the University of Michigan
2019

Doctoral Committee:

Professor Jun Ni, Chair
Professor Elijah Kannatey-Asibu Jr.
Professor Jwo Pan
Professor Alan Taub

Kai Chen
chenkai@umich.edu
ORCID iD: 0000-0003-2223-9859

ACKNOWLEDGEMENTS

I would like to express my sincere appreciation to my advisor Professor Jun Ni for his guidance, instruction and supervision of my research. Without his encouragement, I would not even consider the Ph.D. program in my study at the University of Michigan. I would also like to extend my sincere gratitude to my dissertation committee members, Professor Alan Taub, Professor Jwo Pan and Professor Elijah Kannatey-Asibu for spending their time and effort to review this dissertation.

I would express my special thanks to Dr. Xun Liu and Mr. Xianli Qiao for the support during my research. They are always helpful when I meet difficulties in the work. I also want to thank the United States Steel Corporation for providing the TRIP 780 steel, which is the major material used in my research. I also appreciate Yangbing Lou and Kevin Wilt for arranging the activities for the lab particularly I really enjoy the hotpot and picnic. I would also express my thanks to my friends at S. M. Wu Manufacturing Research Center: Dr. Baoyang Jiang, Luo Ying, Hao Lei, Huanyi Shui, Xin Weng and Zongtai Luo.

At last, I would show my appreciation for my parents and my wife Lei Yu. They are always supporting me with my work and study, especially in the difficult time that I have faced during these years.

TABLE OF CONTENTS

ACKNOWLEDGEMENTS ii
LIST OF FIGURES v
LIST OF TABLES x
ABSTRACT xi
CHAPTER 1 INTRODUCTION 1
  1.1 Background and Motivation 1
  1.2 Research Objectives 6
  1.3 Thesis Outline 8
CHAPTER 2 EXPERIMENTAL INVESTIGATION OF THE FSSW OF ALUMINUM ALLOY TO ADVANCED HIGH STRENGTH STEEL 10
  2.1 Literature Review 10
  2.2 Experimental Details 15
  2.3 Results and Discussion 18
    2.3.1 Effects of Plunge Speed on Force History 18
    2.3.2 Microstructure 20
    2.3.3 Microhardness 25
    2.3.4 Lap Shear Force 26
    2.3.5 Failure Mode 33
  2.4 Conclusions 37
CHAPTER 3 THERMAL MECHANICAL MODELING ON FRICTION STIR SPOT WELDING OF DISSIMILAR MATERIALS BASED ON COUPLED EULERIAN-LAGRANGIAN APPROACH 39
  3.1 Literature Review 39
  3.2 Analytical Formulations 43
    3.2.1 Governing Equations 43
    3.2.2 Lagrangian Step 45
    3.2.3 Penalty Method 46
    3.2.4 Mixture Theory 47
    3.2.5 Johnson-Cook Material Model 49
    3.2.6 Modified Coulomb's Friction Law 50
  3.3 Experimental Details 51
  3.4 Finite Element Model 52
  3.5 Results and Discussion 55
    3.5.1 Welding Geometry 55
    3.5.2 Axial Welding Force 59
    3.5.3 Thermal History 62

3.5.4 Model Validation Using A Different Tool Geometry 63
3.6 Conclusions 65
CHAPTER 4 KEYHOLE REFILLED FRICTION STIR SPOT WELDING OF ALUMINUM ALLOY TO ADVANCED HIGH STRENGTH STEEL 67
4.1 Literature Review 67
4.2 Experimental Configuration 71
4.2.1 Welding Procedure 71
4.2.2 Experimental Setup 72
4.3 Investigation of the Keyhole Refilled FSSW 74
4.3.1 Weld Geometry 74
4.3.2 Metallographic Analysis 78
4.3.3 Joint Lap Shear Force 80
4.3.4 Pure Circular Path Welding 84
4.3.5 Joint Failure Mode 86
4.4 Conclusions 89
CHAPTER 5 FRICTION STIR RESISTANCE SPOT WELDING OF ALUMINUM ALLOY TO ADVANCED HIGH STRENGTH STEEL 91
5.1 Literature Review 91
5.2 Experimental Configuration 95
5.2.1 Experimental Setup Details 95
5.2.2 Initial Experimental Setup Design 96
5.2.3 Experimental Setup Design Improvement 98
5.3 Results and Discussion 103
5.3.1 Effect of Electrical Pulse on Axial Welding Force 103
5.3.2 Comparison Between the Effects of Electrical Pulse and Direct Current 104
5.3.3 Effect of Current on Material Flow 106
5.3.4 Effect of Current on Welding Strength 109
5.4 Conclusions 116
CHAPTER 6 CONCLUSIONS AND FUTURE WORK 118
6.1 Conclusions 118
6.2 Future Work 119
BIBLIOGRAPHY 123

LIST OF FIGURES

Figure 2-1. Dimensions of the FSSW tool ... 15

Figure 2-2. Dimensions of lap shear test (unit: mm) ... 16

Figure 2-3 Illustration of the installation of thermocouples ... 18

Figure 2-4. Plunge force as a function of the plunge distance (Plunge speed 5mm/min, dwell time 10s) ... 19

Figure 2-5. Maximum plunge force at different plunge speeds ... 20

Figure 2-6. (a) Cross section view of the weld nugget (b) Geometry of the hook (c) Detailed view of the right end side of welding zone (Plunge speed 10mm/min, dwell time 5 s) 23

Figure 2-7. (a) Typical hook geometry on the left side (b) EDS line test on the swirling structure (c) Element weight percentage from EDS line test (Plunge speed 5 mm/min, dwell time 10 s) ... 23

Figure 2-8. Al-Fe phase diagram [87] ... 24

Figure 2-9. (a) Groove line shows up after etching (b) EDS line test from point A to point B (Plunge speed 10 mm/min, dwell time 3 s) ... 24

Figure 2-10. ROI Count for Zinc from EDS line test ... 24

Figure 2-11. (a) EDS line test on the coating of steel (b) Element distributions from the test result ... 25

Figure 2-12. Vickers hardness distribution (Plunge speed 10 mm/min, dwell time 5 s) ... 26

Figure 2-13. Joint shear force from different plunge speeds ... 27

Figure 2-14. Cross-sectional view of FSSW joint with plunge speed of 15mm/min ... 27

Figure 2-15: Illustration of the experimental setup for measuring the temperature ... 29

Figure 2-16: Temperature profile with different plunge speed: (a) 2 mm/min (b) 10 mm/min (c) 20 mm/min; (d) Peak temperature with different plunge speeds ... 29

Figure 2-17. Main effects of different plunge speeds and dwell time on joint shear force .. 32

Figure 2-18. Interaction plot of different plunge speeds and dwell time on joint shear force 33
Figure 2-19. (a) Cross nugget failure mode (b) Schematic illustration of tensile shear test. 34
Figure 2-20. Cross section view of the fracture: (a) At the beginning of tensile test: Cracks formed in the IMCs, (b) At the end of tensile test: Cracks propagate and fracture occurs 35
Figure 2-21. Illustration of the failure process in the right side of the nugget, where the aluminum is subjected to tensile stress 35
Figure 2-22. Illustration of the failure process in the left side of the nugget, where the aluminum is subjected to compressive stress... 36
Figure 2-23. Failure on the left side of the nugget... 36
Figure 2-24. (a) Failure happened at the tensile side while the compressive side is still connected (b) Enlarged view of the fracture region.. 36
Figure 2-25. SEM images of the fracture surface on the aluminum side 37
Figure 3-1. Two steps of the operator splitting algorithm in the CEL formulation [110] 45
Figure 3-2. Illustration of the penalty displacement in Penalty method 47
Figure 3-3. Schematic illustration of the mixture theory applied in this model [110].......... 49
Figure 3-4. Fixture setup for the welding process 52
Figure 3-5. Geometry and mesh of the workpiece in the model.. 53
Figure 3-6. Geometry and mesh of the welding tool in the model 54
Figure 3-7. Material assignment and boundary conditions in the model............................. 55
Figure 3-8. (a) Cross section view of the welding nugget (b) Geometry of the hook (c) Cross section view of the modeling result 56
Figure 3-9. Material distribution at different plunge depths.. 58
Figure 3-10. Comparison between experimental results with calculated force history........ 61
Figure 3-11. Aluminum distribution at the plunge depth of 1.0mm.................................... 61
Figure 3-12. Comparison between the experimental work and the numerical model 63
Figure 3-13. Comparison between experimental results with calculated force history with shoulder diameter of 6.5mm 65
Figure 3-14. Material distribution of extruded steel at a plunge depth of 1.61mm 65

Figure 4-1 Schematic illustration of the refilled friction stir spot welding process [121] 68
Figure 4-2 Schematic illustration of SRFSW process[131] 70
Figure 4-3. Schematic illustration of keyhole refilled FSSW process 72
Figure 4-4. Schematic illustration of the weld cross section of the keyhole refilled FSSW 72
Figure 4-5. Fixture setup for the keyhole refilled FSSW 74
Figure 4-6. Macroscopic view of the keyhole refilled FSSW (a) Top view (b) Cross section view (c) Welded sample before the tensile test 77
Figure 4-7. Enlarged view of material distribution around the original keyhole region 77
Figure 4-8. EDS analysis at the Al/Fe interface along line A-B in Figure 4-8 (a) 78
Figure 4-9. Cross section view of etched specimen: (A) Overall view of the hook on the left side (B) Enlarged view of region B (C) Enlarged view of region C (D) Enlarged view of region D 80
Figure 4-10. Force displacement curve with/without refilled keyhole during the lap shear test 82
Figure 4-11. Comparison of (a) Lap shear force and (b) Elongation distance with/without the refilled keyhole 83
Figure 4-12. Top view of the joint geometry from the pure circular path welding 85
Figure 4-13. Comparison of force-displacement curves with different welding processes .. 86
Figure 4-14. Comparisons of (a) Lap shear force and (b) Elongation distance with different welding processes 86
Figure 4-15. Failure modes for (a) FSSW (b) Pure circle path welding (c) Keyhole refilled FSSW 88
Figure 4-16. (a) Schematic illustration of the failure (b) Top view of the failure on steel side 89
Figure 4-17. Scanning Electron Microscopy (SEM) images on the fracture surface 89
Figure 5-1 Schematic illustration of electrically assisted FSW by Luo et al. [153] 93
Figure 5-2. Schematic illustration of electrically assisted FSW by Santos et al.[154] 94
Figure 5-3. Schematic illustration of electrically assisted FSW by Liu et al. [61] 94
Figure 5-4. Illustration of FSSW tool dimension and the definition of the plunge depth 96
Figure 5-5. Illustration of the initial experimental setup for the electrically assisted FSSW 97

Figure 5-6. Schematic illustration of different electrode positions for electrically assisted FSSW 97
Figure 5-7. (a) Current density distribution when both electrodes are placed on the top aluminum side (b) Current density distribution when the electrodes are placed on different base materials 99
Figure 5-8. Stress-strain curve during electrically assisted forging process of steel [156] .. 99
Figure 5-9. (a) Illustration of the experimental setup for electrically assisted FSSW (b) Schematic illustration of the current flow during the welding process 100
Figure 5-10. Simulation results for the current density distribution of the experimental setup 101
Figure 5-11. (a) Experimental setup for the electrically assisted friction stir spot welding (b) A typical welded sample 102
Figure 5-12. Comparison of the axial plunge force with and without the electrical current 104
Figure 5-13. Recorded current pulse signal during the FSSW welding process 105
Figure 5-14. Comparison of axial plunge force with the 560A DC, 900A pulse and zero current condition 106
Figure 5-15. (a) General cross section view of the welding region (b) Enlarged cross section view of the sample (c) EDS line test from point A to B 107
Figure 5-16. ROI counts for Zn through EDS line test 108
Figure 5-17. Zn flow pattern during the welding process (a) with direct current (b) without current 109
Figure 5-18. Comparison of shear strengths under the conditions of no current, 560A DC and pulse 109
Figure 5-19. Illustration of the material interaction between steel and aluminum 110
Figure 5-20. Vortex shape generated at the top of the hook (no current) 110
Figure 5-21. (a) Illustration of the mixing pattern between aluminum and steel at a deeper plunge depth (b) Cross section view of the inside of the hook (no current) 111
Figure 5-22. Enlarged cross section view of Fe/Al interface (a) without current (b) with direct current (c) with pulses 112

Figure 5-23. Corresponding EDS line test results along Fe/Al interface (a) without current (b) with direct current (c) with pulses 114
Figure 5-24**.** Cross-section view at the left side of hook (560A DC) 116
Figure 6-1 Illustration of the improved key-hole refilled FSSW process........ 121
Figure 6-2 Illustrations of keyhole refilled FSSW with spiral retreat configuration........ 121
Figure 6-3 Fracture surface of different welding configurations (a) Aluminum on the top (b) Aluminum on the bottom........ 122

LIST OF TABLES

Table 2-1. Chemical compositions of the base material Al 6061-T6 16

Table 2-2. Experimental design matrix.. 17

Table 2-3. ANOVA of the weld strength with different process conditions 32

Table 3-1. Material constants used in the Johnson-Cook’s model 50

Table 4-1. Process parameters for the conventional FSSW step 73

Table 4-2. Process parameters for the keyhole refilling step.. 74

Table 4-3. Comparisons of the lap shear force for Al/Fe FSSW 83

Table 5-1. Process parameters for the electrically assisted FSSW 102

ABSTRACT

In recent years, growing amount of attention has been drawn to studies of reducing vehicle weights in automotive industry considering both economic and environmental factors. One of the effective methods to achieve this goal is to replace steel components with multi-material vehicle structures. Joining of dissimilar materials is therefore very important to meet this demand. It is generally difficult to join dissimilar materials with the conventional welding technologies, as they have quite different physical and chemical properties. In addition, the formation of large amount of brittle intermetallic compounds (IMCs) is highly detrimental to joint quality.

Friction stir welding (FSW) is a solid state welding technique and can avoid bulk melting during the process. As a variant of friction stir welding, friction stir spot welding (FSSW) is a promising solution to make spot joints between dissimilar materials. However, limited studies have been conducted on the FSSW of dissimilar materials, specifically aluminum alloy to steel. When performing the FSSW, the keyhole left on the welding zone deteriorates the joint strength and the process requires a large plunge force to make a spot welding with the dissimilar materials.

To solve the existing issues, the FSSW process has been successfully applied to join aluminum alloy 6061-T6 to TRIP 780 steel. Cross sections of weld specimens show the formation of a hook with a swirling structure. A higher magnified SEM view of the swirling structure with EDS analysis reveals that it is composed of alternating thin layers of steel and Al/Fe intermetallic compounds (IMCs). To evaluate the effects of different process parameters including tool plunge speed and dwell time on the weld strength, the design of experiments (DOE) and analysis of variance (ANOVA) is used. It shows that dwell time is a more dominant parameter in affecting the weld strength than plunge speed. Furthermore, the investigation of failure after applying lap shear tests reveals that the cross nugget failure is the only failure mode.

A FSSW process model is developed in this study based on the Coupled Eulerian-Lagrangian (CEL) method, which considers the material flow at the dissimilar material interface and the interaction between the welding tool and workpiece. The force and thermal history generated by the numerical work also correspond well with the experimental data.

In the experimental investigation of applying the proposed keyhole refilled FSSW process to join aluminum alloy 6061-T6 to TRIP 780 steel, it is shown that the original keyhole area is filled with the aluminum alloy and no obvious voids can be found at the Al/Fe interface. The lap shear force produced by the keyhole refilled FSSW increased by 55.98% when compared to the conventional FSSW. Three bonding mechanisms can be concluded according to the experimental observations: (1) the keyhole is refilled by the aluminum alloy; (2) the bonding area is increased between the steel and aluminum; and (3) the hooks developed from the conventional FSSW process generate bonding between the steel and aluminum.

Finally, the electrically assisted FSSW process for joining aluminum alloy 6061-T6 to TRIP 780 steel is performed. The experimental results show that the application of electrical current reduces the axial plunge force and assists the material flow of the aluminum matrix during the welding process.

CHAPTER 1

INTRODUCTION

1.1 Background and Motivation

In recent years, a growing amount of attention has been given to studies of reducing vehicle weights in automotive industry due to both economic and environmental considerations. One promising line of inquiry involves replacing steel components with multi-material vehicle structures [1]. Aluminum alloy can be a promising candidate for partially replacing steel. However, this design requires joining dissimilar base materials, which in turn creates a challenge. One of the most critical challenges is that the base materials have extremely different physical and mechanical properties. Resistance spot welding (RSW) is the most widely used joining technique in automotive industry. However, the problem rises when welding the aluminum alloy with the RSW. First, the aluminum alloy has a higher thermal conductivity and higher electrical conductivity than that of steel, which requires a higher current density and shorter welding time in the welding process [2-5]. Then, the oxide film generated at the aluminum surface needs to be removed before the welding, which has a melting temperature of 2000^0C while the aluminum alloy only has the melting temperature around 660^0C [2]. In the meantime, welding the aluminum alloy requires higher electrode force [6], it also brings the problems of the inconsistent weld quality and short electrode life [7, 8].

The rapid development of high strength steels also attracts the attention of the automotive industry. The steels can be classified as high strength low alloy (HSLA), dual phase (DP), complex phase (CP), transformation induced plasticity (TRIP) and interstitial-free (IF) steels due to different mechanical properties and advantages. Most of them have superior properties, which result in a weight saving for the vehicle and increasing in the structural strength [9]. Among them, the DP and TRIP steels are named as advanced high strength steel (AHSS), which obtains a higher strength and more ductility. For the TRIP steel, it contains bainite and martensite with the retained austenite in the ferrite microstructure. The existing of the retained austenite enhances the ductility of the TRIP steel by transforming the austenite to martensite under stress. This phenomenon leads to an increase in strength, toughness and ductility of the steel [10-14].

The joining of dissimilar materials creates difficulties for conventional welding technologies, which rely on melting of the bulk materials. The conventional fusion welding of the dissimilar materials brings the problems including the formation of a significant amount of intermetallic compounds (IMCs), the generation of the porosity and low welding strength [15-18].

To overcome the challenges, solid-state welding was introduced as a promising technique due to its capability to minimize bulk melting during the welding process. This welding technique is considered as a “green” technology due to its energy efficiency and environmental friendliness. When compared to the conventional welding methods, no shielding gas is required and no consumable materials are needed [19]. Among the solid state welding technologies, the friction stir welding (FSW) and friction stir spot welding (FSSW) are widely used to join aluminum alloys. As the welding process generates a limited amount of heat, it can join the materials without bulk melting. Besides, it does not generate dendritic structures, which are undesirable in the fusion welding [20]. Especially for the FSSW, it has the potential to become an alternate for the RSW in welding the aluminum alloys. During FSSW, a rotating tool with a pin feature is gradually plunged into the base materials at a prescribed speed until the desired plunge depth is reached. The tool is then held rotating at that position for a short period of dwell time. Next, the tool is retracted and a weld is achieved. Lots of research have been conducted on welding the aluminum alloy through the FSSW, including aluminum alloy 5052 [21, 22], 5083 [1], 5754 [23, 24], 6061 [25-30], 6011 [31], 7050 [32] and 7075 [33]. The above research investigated the microstructure, process parameters, mechanical performance, tool geometry, different tool paths, thermal-mechanical modeling and corrosion. It is known that the joint strength produced by FSSW is dependent on welding process parameters, including the rotation speed, the plunge speed, the plunge depth and the dwell time [21, 34-39].

Abundant studies have been conducted on the FSSW of aluminum to conventional steel, including the welding of aluminum alloy 6016 to IF steel [40], 6061 to low carbon steel [41], 6061 to AISI 1018 [42], 6111 to DC04 steel [43], 1050 to hot stamped born steel [44] and 5083 to St-12 steel [45]. More and more attention has been paid to the FSSW of dissimilar materials in recent years.

Regarding the modeling work of the FSSW process, few models were developed for the FSSW of dissimilar material. Most of the modeling work with the similar material FSSW is based on the Arbitrary Lagrangian-Eulerian (ALE) approach [46-48]. The ALE modeling approach has the advantages of defining the sliding boundary condition at the tool-workpiece interface. It can also generate the temperature dependent material properties. The drawback of the ALE method is its poor capability of capturing the void formation during the welding process as the Lagrangian elements have to be completely filled with material in the modeling process[49]. Besides, the Lagrangian mesh moves together with the materials. When the base materials are under the large deformations such as during the FSSW process, the massive distortion of the mesh will make it difficult to generate a convergent solution [50]. The new Coupled Eulerian-Lagrangian (CEL) approach can be a promising solution for the problems with the large mesh distortion. The CEL approach is mainly based on the Eulerian approach, which means the Eulerian reference mesh remains constant and the material can move freely through the Eulerian mesh [50-54].

Because the base materials are undergoing severe plastic deformation during the solid state welding process in FSSW, it brings several inherent disadvantages, including a large axial plunge force, relative long welding time and insufficient material flow. The large axial plunge force results in intense reactions between the tool and work piece, which leads to severe tool wear after the welding process. Besides, the welding time ranges from 2 to 5 s, which is undesirable when compared to the RSW with the welding time of 10^{-1}s. In the meantime, the material flow during the welding process is not sufficient, which causes the voids in the welding area and deteriorates the join quality. Several attempts have been made to reduce the plunge force and minimize the tool wear from the literature, which includes the preheating before the welding process [55-58], ultrasonic assisted friction stir welding process [59, 60], electrically assisted friction stir welding process [61]. Most of the novel methods are based on the idea that a higher initial temperature for the base materials will reduce the plunge force and increase the welding speed. The concept of preheating material can also be introduced into the FSSW to improve the welding performance.

In addition, a large keyhole is left on the workpiece as an undesirable defect after retraction of the welding tool [33, 62, 63]. The existing keyhole will deteriorate the joint strength and increase the chance of material corrosion. Recently, some improvements have been done to solve the keyhole problem after the FSSW process, including the keyhole refilled FSSW [33, 64-66], the application of the pin-less welding tool [67-70], introducing the multi-tools welding process [62].

However, the solutions provided above are mainly focused on FSSW of the similar aluminum alloy. The keyhole refilled process for the dissimilar material FSSW still remains unsolved. To overcome the difficulty and enhance the weld performance, a novel keyhole refilled process has been proposed in this study.

1.2 Research Objectives

The purpose of this study is to investigate the fundamental mechanisms of the FSSW of aluminum alloy 6061 to Transformation Induced Plasticity (TRIP) 780 steel and apply novel methods to improve the joint quality and reduce the welding force. The specific objectives are summarized as the following:

1. Understanding the fundamental mechanisms of the FSSW of aluminum alloy to advanced high-strength steel: Experimental Friction Stir Spot Welding (FSSW) process will be conducted to join aluminum alloy 6061-T6 to TRIP 780 steel. Various operation conditions will be investigated during the welding process, including the rotation speed, the plunge speed and the dwell time. Cross sections of weld specimens will be analyzed and more attention will be paid to the study of the Al-Fe interface. A magnified Scanning Electron Microscope (SEM) view with the Energy Dispersive X-Ray Spectroscopy (EDS) analysis will be performed on the fracture surface. The joint strength will be evaluated through the mechanical tensile test and different failure modes will be summarized.

2. Thermal mechanical modeling of the FSSW process based on the Coupled Eulerian-Lagrangian (CEL) approach: The model will consider the material flow at the material interaction interface and also the interactions between the welding tool and workpiece. The generated material flow pattern will be compared with the experimental observations. The calculated results will be

validated by comparing with the experimental data, which includes the welding force, welding temperature and material distribution. A new tool geometry will also be applied into the model to further validate the accuracy of the model.

3. Investigation of the keyhole refilled FSSW process: An innovative keyhole refilled FSSW process will be developed for joining Aluminum Alloy 6061 to TRIP 780 steel. With the developed process, the original keyhole produced from the conventional FSSW process will be effectively refilled. Then, the optimal refilled configuration will be determined according to the tensile strength, material flow, microstructure of the fracture surface and fracture mode. The mechanical properties of the keyhole refilled FSSW and conventional FSSW will be compared. Finally, the joint mechanisms will be summarized for the keyhole refilled FFSW.

4. Investigation of the electrically assisted FSSW process: An efficient electrically assisted FSSW experimental system will be developed, which enables a high-density electrical current passing through the weld zone while the tool is only passively involved in the circuit. The applied high-density current will generate enough heat to soften the material and the corresponding electrical plastic effect will also be studied. Then, the effects of both pulsed and direct current on the formation of Intermetallic Compounds (IMCs) will be studied during the welding process. The resulting plunge force, material flow and hook formation will be compared between the electrically assisted FSSW and conventional FSSW. Finally, the effects of different current directions on the welding performance will also be investigated.

1.3 Thesis Outline

This thesis contains six chapters.

In Chapter 1, the motivation and objectives of this research is presented. The demand of reducing the vehicle weight requires a new welding process to join aluminum alloy to advanced high strength steel. The high welding force and undesirable keyhole are the common disadvantages when using the conventional FSSW process. Thus, innovative FSSW methods are proposed to reduce the welding force and increase the joint quality.

In Chapter 2, experimental tests are conducted to investigate the FSSW of dissimilar materials. Effects of operation parameters, including the plunge speed and dwell time, are investigated. The microstructure of the cross section view is shown and the failure mode is further analyzed. This chapter is based on the paper "Effects of Process Parameters on Friction Stir Spot Welding of Aluminum Alloy to Advanced High-Strength Steel", published in ASME Journal of Manufacturing Science and Engineering.

In Chapter 3, the thermal mechanical models of FSSW of dissimilar materials are developed using the Coupled Eulerian-Lagrangian (CEL) approach. In the developed models, the material flow, force history and temperature history are validated with the experimental data. This chapter is based on the paper "Thermal-mechanical modeling on friction stir spot welding of dissimilar materials based on Coupled Eulerian-Lagrangian approach," published in the International Journal of Advanced Manufacturing Technology: 1-11.

In Chapter 4, a keyhole refilled FSSW is performed. The novel method is described in details. In addition, the joint quality and ductility are compared with those of the conventional FSSW process. This chapter is based on the paper "Keyhole refilled Friction Stir Spot Welding of

Aluminum Alloy to Advanced High-Strength Steel", which is published in the Journal of Materials Processing Technology 249 (2017): 452-462.

In Chapter 5, the electrically assisted FSSW is performed. During this process, the produced joint microstructure, welding force and joint strength are compared with those of the conventional FSSW process. This chapter is based on the paper "Friction Stir Resistance Spot Welding of Aluminum Alloy to Advanced High Strength Steel ", which is accepted by the ASME Journal of Manufacturing Science and Engineering.

Chapter 6 provides the conclusion of this dissertation research and presents the future research directions.

CHAPTER 2
EXPERIMENTAL INVESTIGATION OF THE FSSW OF ALUMINUM ALLOY TO ADVANCED HIGH STRENGTH STEEL

2.1 Literature Review

The joint strength produced by the FSSW is dependent on welding process parameters, including the rotation speed, the plunge speed, the plunge depth and the dwell time. The effects of process parameters on the FSSW of similar aluminum alloys have been studied in numerous previous studies. Lathabai et al. [71] employed FSSW on aluminum alloy 6060-T5 and showed that the plunge depth had a profound effect on the joint strength as demonstrated by strong correlation with the dimension of the annular bond area between the two sheets. Karthikeyan et al. [34] applied the response surface method to study the effects of process parameters on friction stir spot welding of aluminum alloy 2024. They found that the plunge speed had the greatest influence on tensile shear fracture load followed by plunge depth, dwell time, and tool rotation speed. Zhang et al. [21] applied FSSW to join aluminum alloy 5052-H112 sheets. They showed that the maximum tensile-shear strength was achieved when rotation speed was 1541 rpm and dwell time was 5 s. In addition to research on aluminum, some researchers had performed FSSW on steel, the mechanical properties of which were quite different from those of aluminum alloys. Lakshminarayanan et al. [72] studied FSSW on low carbon steels. In their works, the tool rotating speed ranged from 1200 revolution per minute (rpm) to 1600 rpm. Their plunge depth, which was defined as the distance from the sheet top surface to the tool shoulder surface, varied from 0 to 0.2mm. Dwell time varied from 5 s to 25 s. They determined the maximum tensile shear strength was obtained under the operation condition of 1157 rpm rotating speed, 0.05mm plunge depth and dwell time of 22 s. They also showed that the dwell time was the most dominant parameter in determining joint properties. Aldanondo et al. [73] welded 2mm thick DP1200 ultra high strength steel through FSSW and reported that the dwell time and the plunge depth were the most critical parameters on influencing the shear strength of the joints. Bilici et al. [74] applied the FSSW to join the high-density polyethylene (HDPE) sheets. From their study, the thickness of the sheet was 4 mm and the weld strength was investigated by the lap shear tensile test. Three sets of process parameters were studied in their research, including the tool rotation speed, dwell time and the tool plunge depth. They also employed the signal to noise ratio (S/N), and the analysis of variance (ANOVA) to verify the importance of different process parameters. From their study, they concluded that the dwell time was the most dominant welding parameter for the weld strength, and the optimal weld strength was obtained when the tool rotation speed was 700 rpm, the dwell time was 60 s and the plunge depth was 6.2 mm. Yuan et al. [35] studied the effects of both tool design and process parameters on the welding strength. They used 1.0mm thick aluminum alloy 6016-T4 as the base material. Besides, they also investigated the differences between a conventional pin tool and off-center feature tool for the welding process. The microstructure of the weld, the lap-shear tensile test and the hardness were shown in their study. They concluded that the tool rotation speed and plunge depth were critical for the lap-shear separation loads. They also found that when the tool penetration depth was at 0.2mm, the weld reached the maximum separation load.

The welding of dissimilar aluminum alloys is also well studied in recent years. Tozaki et al. [37] welded 2017-T6 aluminum alloy and 5052 aluminum alloy with the FSSW. Both sheets had a thickness of 1.0 mm and a conventional cylindrical tool was used in their study. They studied the tool rotation speed and the dwell time as determining factors for the welding strength. From their results, they found the welding strength was positively correlated to the dwell time and it had a negative correlation with the tool rotation speed. Bozkurt et al. [75] welded aluminum alloy 2024-T3 and aluminum alloy 5754-H22 with the thickness of 1.6mm and 1.5mm respectively. The effects of the plate position, the plunge depth, the dwell time and the tool tilt angle on the joint strength were investigated. They concluded that it resulted in a higher joint strength when the aluminum alloy 5754-H22 was at the top position. They also found that a longer dwell time resulted in a higher strength when the dwell time ranges from 2 s to 10 s. Regarding the tool tilt angle, the authors mentioned that the optimum tool tilt angle was 0 if the aluminum alloy 5754-H22 was on the top.

Besides the FSSW between the similar aluminum alloy and dissimilar aluminum alloy, FSSW has been extended to join dissimilar metals such as the aluminum to the magnesium. Rao et al. [76] applied the FSSW to weld the magnesium alloy AM60B to aluminum alloys 6022-T4 with various tool rotation speeds and plunge depths. From their results, they found that the increasing tool rotation speed decreased the material mixing in the stir zone and it also resulted in a lower failure load. On the other hand, they also mentioned that the joint strength increased with higher plunge depth, which was due to the increased weld bond width. The formation of IMCs was also well investigated, while a continuous layer of IMCs resulted in a lower joint strength than a discontinuous layer of IMCs. Sato et al. [77] also welded aluminum alloy 5083 to magnesium alloy AZ31 with FSSW. It was found that a thick interfacial layer mainly composed of IMCs was formed during the welding process and the fracture propagated through the brittle IMCs during the lap shear tensile test. They also indicated that the joint strength increased with the increasing plunge depth at a rotation speed of 1500 rpm, while there was no difference between the joint strength for different plunge depth at a rotation speed of 2250 rpm. Chowdhury et al. [78] also joined the magnesium AZ31B-H24 to aluminum 5754-O with FSSW. Both of them had a thickness of 2.0 mm. The authors mentioned that the Al/Mg dissimilar weld was characterized by the formation of a distinctive interfacial layer with the existing IMCs. There were two distinct failure modes observed in the tensile tests, including the nugget pullout due to a higher cyclic load and the opening keyhole failure due to the lower cyclic loads.

A few studies have been conducted on solid-state welding of dissimilar materials, specifically aluminum alloy to conventional steel. Bozzi et al. [40] welded dissimilar materials of 1.2 mm aluminum alloy 6016 to 2 mm IF-steel. They found that the intermetallic compound (IMC) layer was necessary to guarantee the weld strength. However, if the thickness of the IMC layer exceeded a certain value, cracks were initiated and propagated easily through the brittle IMC, which led to weak weld strength. Chen et al. [43] applied the abrasion circle friction spot welding process for welding 1mm aluminum alloy 6111-T4 to DC04 steel. In their process, a probe tool moved along a circular path to abrade the steel sheet on the bottom. Regarding the reaction between steel and aluminum, no IMCs were found at their interface. Taban et al. [42] performed inertia friction welding of aluminum 6061-T6 and AISI 1018 steel with the diameter of 12.5 mm. The maximum joint strength reported was 250 MPa, and the IMC layer with a thickness of 350 nm was generated during the welding process. Jana et al. [79] investigated the friction stir lap welding of AZ 31B magnesium alloy to steel. The maximum joint force they reached was 6.3 kN. In their study, they used steels with a thickness of 1.5 mm and 0.8 mm, the test results showed that the 0.8mm steel generated a higher joint efficiency. Sun et al. [80] welded 1mm aluminum alloy 6061 to mild steel with the flat spot FSW technique. During flat spot FSW, a probe-less rotating tool was applied to flatten the weld surface after the creation of the spot welding. Applying this technique eliminated the keyhole defect, which improved the physical properties of the joints. The examination of particle formation revealed no IMC layer. Figner et al. [81] welded aluminum alloy 5754 to galvanized steel HX 340LAD. They found that increasing the spindle speed at the constant dwell time will lead to higher strength. It is mainly due to the fine dispersed particle observed in the cross section area. The authors also mentioned that a higher amount of IMC was observed when the dwell time increased at constant spindle speed. Liu et al. [82] applied FSW of aluminum alloy 6061 to TRIP 780/800 steel with a butt joint configuration. They showed that the maximum tensile strength achieved by FSW was about 85% of the base Al alloy. This was obtained under the following conditions: rotation speed of 1800 rpm, welding speed of 90 mm/min and tool offset of 1.63 mm. Hong et al. [83] welded 1.5 mm TRIP 780 sheet with 1.4 mm HSBS sheet with FSSW technique. The failure mode and fatigue behavior were examined in their paper. They found that the weld gap and the bend distance were significant in affecting the weld fatigue life.

Despite these studies on welding aluminum to conventional steel, few literature has reported FSSW of aluminum alloy to advanced high strength steel, which has much higher yield strength than conventional steel. Such work is important because the advanced high strength steel has a higher specific strength and strain hardening capacity, which makes it attractive for replacing the conventional steel in lightweight vehicles. The higher strain hardening capacity results in a larger plunge force during the welding process. Prior studies of plunge speed on welding strength between similar materials showed inconsistent results. Lathabai et al. [71] found that the plunge speed had little effect on the weld strength. However, Baskoro et al. [84] indicated that slower plunge speed would increase the joint strength. Less study to date has investigated plunge speed effects in FSSW between aluminum alloys to advanced high strength steel.

In this chapter, friction stir spot welding is applied for joining aluminum alloy 6061-T6 to one type of advanced high strength steel, TRIP 780/800 steel. To study the effects of plunge speed and dwell time on the weld strength, the rotation speed and the plunge depth are kept constant during the experimental process. Several combinations of the plunge speed and the dwell time are studied by applying the design of experiments method. Further analysis is done by checking the microstructure of the joint cross section and characterizing failure mechanisms.

2.2 Experimental Details

Aluminum alloy 6061-T6 is used in this study and the chemical compositions are listed in Table 2-1. The yield strength of the aluminum alloy 6061-T6 is 241 MPa. According to the previous work done by Liu et al. [85], the yield strength of the TRIP 780 steel is around 780 MPa and the ultimate tensile strength is around 1300 MPa. The hardness of the base materials are tested, and the corresponding results will be shown in the results and discussion section below. For the lap welding configuration, the aluminum sheet is placed on the top of the steel sheet. The thickness of both sheets is 1.5 mm. The FSSW tool is made of tungsten carbide with 10% cobalt and the hardness of the tool material is 91.8 HRA. The tool consists of a non-threaded cylindrical pin with flat shoulder surface and the detailed dimensions are presented in Figure 2-1.

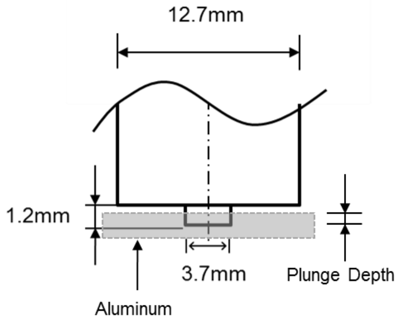

Figure 2-1. Dimensions of the FSSW tool

Tensile test specimens were prepared according to the JIS Z 3136:1999 standard and detailed dimensions were shown in Figure 2-2. During experiments, the tool axis was aligned with the center of the overlapped area. After welds, lap shear tensile tests were performed on a computer-assisted INSTRON tensile machine with a loading speed of 1mm/min. Three replicates were tested for each welding condition. A Kistler dynamometer was mounted below the workpiece for the measurement of the axial plunge force during the welding process. To further analyze the welding properties, the obtained welds were sectioned in the center and then mounted, ground and polished. Joint cross-sections were characterized using both optical and scanning electron microscope (SEM). Energy dispersive X-ray spectroscopy (EDS) analysis was further performed for determining elemental distributions at the Al-Fe interfaces. The fractographic examination was also performed on the broken tensile specimens using Philips XL-30 SEM. Hardness distribution on joint cross sections was measured with CLARK micro-hardness tester and a 100 g load was applied for 15 s.

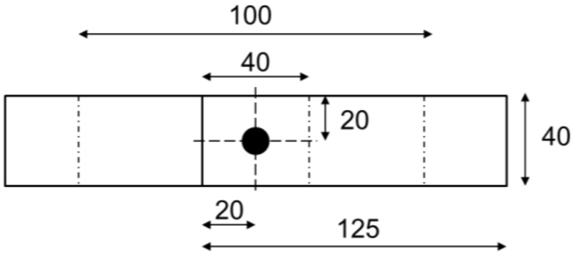

Figure 2-2. Dimensions of lap shear test (unit: mm)

Table 2-1. Chemical compositions of the base material Al 6061-T6

	Chemical Composition (wt.%)									
Material	Al	Mg	Si	Cr	Mn	Ti	Cu	Zn	Fe	other
Al6061-T6	95.1-98.2	0.8-1.2	0.4-0.8	0.05-0.4	<0.15	<0.15	0.05-0.4	<0.25	<0.7	Balance

Several experiments have been done before investigating the effects of process parameters, including changing the plunge speed from 2 mm/min to 20 mm/min while the others are kept as constant. In this research, the plunge speed and dwell time were examined in three levels. All experiments were performed under the same rotation speed and plunge depth, which was 2000 rpm and 0.4 mm into steel sheet respectively. The definition of the plunge depth is also illustrated in Figure 2-1. The investigated welding conditions are summarized in Table 2-2.

Table 2-2. Experimental design matrix

Experimental Order	Plunge Speed (mm/min)	Dwell Time (s)
1	5	1
2	5	5
3	5	10
4	10	1
5	10	5
6	10	10
7	15	1
8	15	5
9	15	10

The temperature during the welding process is measured through three individual thermocouples. A general way to place a thermocouple is drilling a small hole at the backing plate, which has a larger diameter than the thermocouple. In this way, the thermocouple can be inserted into the backing plate to measure the temperature during the welding process. One drawback for this method is that the thermocouples can not be fixed rigidly in the hole as the external force may push the thermocouple back into the hole. It may result in inaccurate results as the position of the thermocouple is quite critical for the temperature measurements. In order to prevent this issue, a different method is applied for the installation of the thermocouples, which is shown on Figure 2-3. It can be described as the following: First, the backing plate is sliced into two parts and the sliced surfaces are milled for further modification. Then, three slots are drilled on one side of the backing plate, the dimension of the slots is smaller than the thermocouples, which is to ensure the thermocouples can be rigidly fixed into the slots. Threaded holes are also made in both of the backing plate as shown in Figure 2-3 (a). Finally, the two pieces of backing plate are tighten with screws as the thermocouples are placed into the slots. In this way, the position of the thermocouples can be fixed rigidly and it can ensure the repeatability of the measurements. In the meantime, it can be confirmed that the thermocouples are touched closely to the back of the base material.

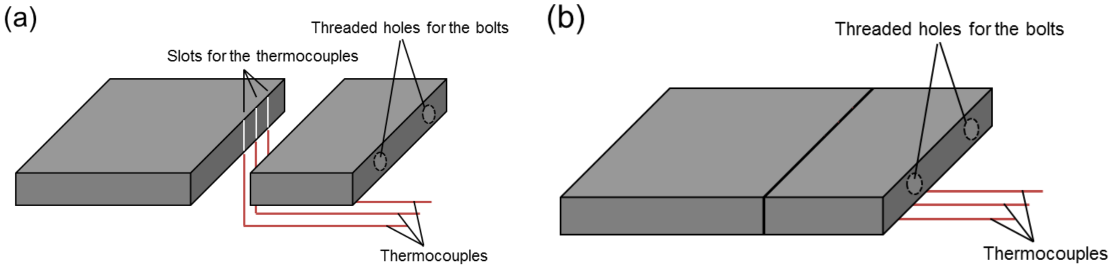

Figure 2-3 Illustration of the installation of thermocouples

2.3 Results and Discussion

2.3.1 Effects of Plunge Speed on Force History

Figure 2-4 shows a typical curve of the axial plunge force as a function of tool plunge distance. The peak plunge force is reached when the bottom surface of the pin penetrates 0.4 mm into steel, which corresponds to point 5 in the figure. The history of plunge force can be roughly divided into five regions. From the initial position to point 1, the rotating pin starts to touch aluminum top surface and gradually moves into the workpiece. During this stage, the plunge force increases due to the growing amount of deformation materials and only aluminum is stirred around the tool pin. From point 1 to point 2, as the pin travels deeper into aluminum, the heat generated from both friction and plastic deformation in the workpiece softens aluminum to an overheated level, which makes it easier for the pin to plunge further into the workpiece and results in a decreased plunge force. At point 2, the tool shoulder surface begins to touch the squeezed out aluminum. As the entire shoulder area starts to deform aluminum, plunge force increases again. After that, as the rotating shoulder moves deeper into aluminum, it deforms the material and acts as a pin with a larger diameter. Similar to the condition between point 1 and point 2, the heat generated from friction and severe plastic deformation will reach an overshoot level, which softens the material and decreases the force-increasing rate from point 3 to point 4. From point 4 to point 5, a certain amount of steel has been deformed by the tool pin. This portion of steel is then squeezed by the tool pin to flow upward, which is further suppressed by the tool shoulder. Therefore, the plunge force increases rapidly in this region. Finally from point 5 to point 6, which corresponds to the dwell period, the plunge force decreases as a consequence of continuing frictional heat generation at the interface between tool and workpiece without further deformation.

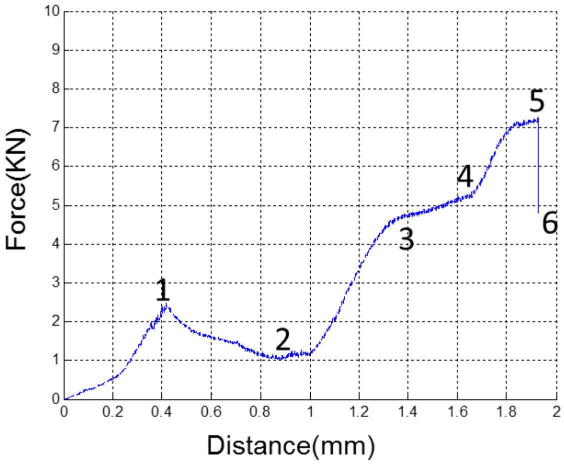

Figure 2-4. Plunge force as a function of the plunge distance (Plunge speed 5 mm/min, dwell time 10 s)

The effect of different plunge speeds on the maximum axial force at the end of plunge stage is studied and the relationship is shown in Figure 2-5. It can be observed that the maximum plunge force is positively correlated to plunge speed at all levels that have been investigated in this study. Since higher plunge speed provides less amount of heat during the welding process, the deformation resistance of materials remains high, which requires a larger maximum plunge force. In addition, the difference in maximum axial force due to different plunge speeds becomes smaller as the plunge speed increases. For example, the maximum plunge force increased by 1.07 KN when the plunge speed increased from 2 mm/min to 5 mm/min. On the other hand, the increment was only 0.26 KN when the plunge speed increased from 15 mm/min to 20 mm/min. In the power law, the n value of the aluminum alloy is 0.2, which indicates a larger resistance force at the higher strain rate. However, the temperature is also a critical factor in determining the plunge force in the welding process. The softening effect compensates the work hardening at the higher strain rate, which results in a lower increase rate as we observed.

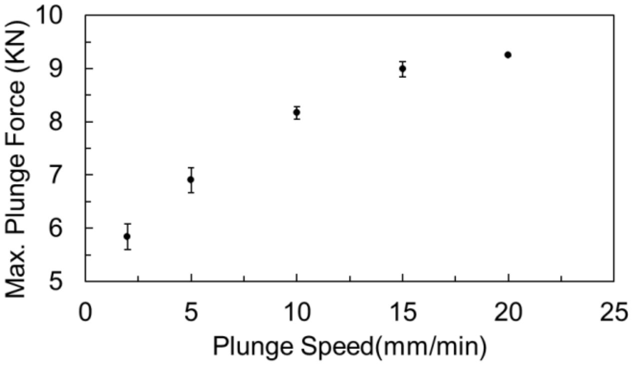

Figure 2-5. Maximum plunge force at different plunge speeds

2.3.2 Microstructure

One of the typical cross sections of the weld zone is shown in Figure 2-6 (a) and the corresponding welding parameters include plunge speed of 10 mm/min and dwell time of 5 s. Overall, there are no obvious cracks at the interface between steel and aluminum. Regarding the interaction between steel and aluminum, a hook feature is observed around the weld nugget, which is also reported by Bozzi and Figner [81, 86]. The enlarged view of this hook is presented in Figure 2-6 (b). The formation of the hook is primarily due to two factors. First, the downward squeezing motion of the pin extrudes the steel to flow upward. Second, the upward flow of steel is restrained by the larger compression force from tool shoulder surface. This portion of steel is therefore bent over and embedded into the relatively soft aluminum matrix, which finally forms the hook structure. Furthermore, a unique swirling structure layer can be noticed in the top boundary of the hook, as marked out by the region "A" in Figure 2-6 (b). This swirling structure can be observed in all the investigated conditions, as shown in Figure 2-7 (a), which corresponds to plunge speed of 5 mm/min and dwell time of 10s. In Figure 2-6 (a), the right side of the figure corresponds to the squeezed aluminum that accumulated around the periphery of tool shoulder region rather than the original aluminum sheet. It is mainly caused by the material flow driven by tool shoulder. As the shoulder surface is pressed into aluminum, the aluminum material below the tool is squeezed out, which flows upward surrounding the outside surface of the tool. In the meantime, a gap between the top aluminum sheet and bottom steel sheet is generated as indicated B in Figure 2-6 (c). Accordingly, the thickness of accumulated aluminum in this region is larger than 1.5 mm.

To analyze the swirling feature in details, a higher magnified SEM view is shown in Figure 2-7 (b). Elemental distribution of the swirling structure is obtained through EDS line scanning along the arrow line from point C to point D. The results are shown in Figure 2-7 (c). In the beginning interval of 0-2 µm, the weight percentage of Fe is almost 100%, which indicates point C is steel. In the next interval of 2-5 µm, a relatively constant weight percentage ratio between Al and Fe can be observed, which indicates the formation of intermetallic compounds (IMCs) in this layer. Finally, the Fe composition curve returns to a high level at the interval of 5-6 µm, which indicates point D is steel again. The thickness of this IMC layer is around 3 µm. Based on the Al-

Fe phase diagram, as shown in Figure 2-8 [87] and the Al-Fe atomic ratio from the EDS results, the composition of the IMC layer is likely to be Fe_2Al_5 or $FeAl_2$. From the observations above, the swirling structure is actually composed of alternating thin layers of steel and IMCs, which exhibits as a fence-shaped morphology. The formation of IMCs is mainly due to the combined condition of frictional heat generated from tool rotational motion as well as the large compression force at the Al/Fe interface. In the following analysis of lap shear tests results, it can be shown that the hook and IMC layer in the swirling feature are key factors that determine FSSW joint strength.

The material flow during welding process has also been investigated in this study. Figure 2-9 (a) shows a cross-sectional view located near the tool shoulder edge, which corresponds to Figure 2-6 (c). A groove line is observed in the view, which originates from the bottom of the aluminum and extends upward. To further obtain its elemental compositions, the EDS analysis is performed along the straight line shown in Figure 2-9 (b). The detected ROI count of Zinc from Figure 2-10 indicates that the groove line primarily consists of the zinc element. The Zinc element comes from the coating of the steel, as shown in Figure 2-11 for the original steel sheet. The EDS analysis shows a layer of Zinc coating on the steel surface with the thickness of around 5 μm. The observed zinc line on the shoulder edge region helps illustrate aluminum material flow during the welding process: as the plunge depth increases, the aluminum on the top region of the sheet is compressed by the tool shoulder and squeezed outward. In the meantime, under the condition of the combined high pressure and high temperature, the aluminum near the bottom region of the sheet is mixed with the Zinc coating on the steel. As the tool plunge depth further increases, the mixed materials flow outward and then they turn upward due to the constraints of the surrounding materials, which has a relatively low temperature and is harder to deform. In this perspective, the zinc groove line can be referred as a tracer for the movement of the aluminum on the bottom.

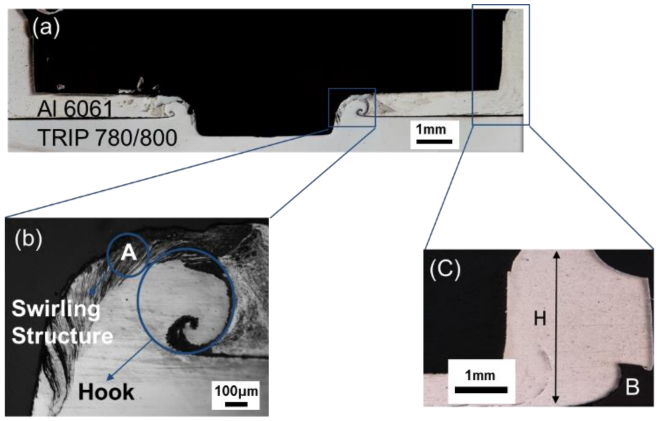

Figure 2-6. (a) Cross section view of the weld nugget (b) Geometry of the hook (c) Detailed view of the right end side of welding zone (Plunge speed 10 mm/min, dwell time 5 s)

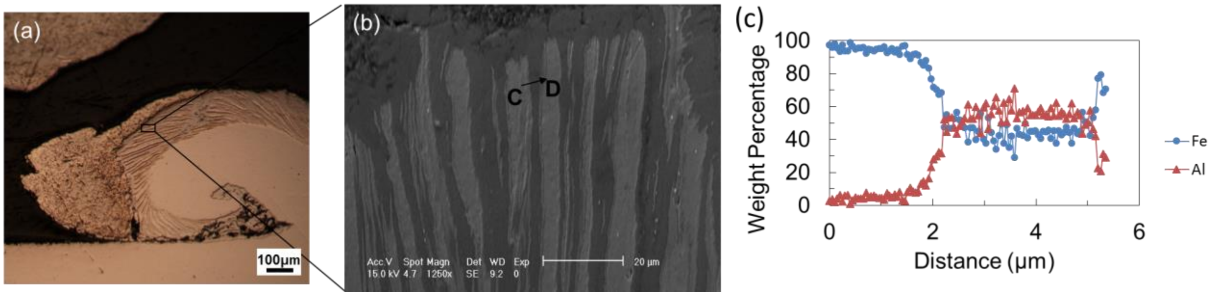

Figure 2-7. (a) Typical hook geometry on the left side (b) EDS line test on the swirling structure (c) Element weight percentage from EDS line test (Plunge speed 5 mm/min, dwell time 10 s)

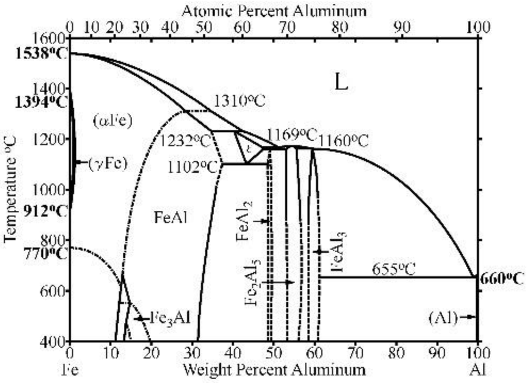

Figure 2-8. Al-Fe phase diagram [87]

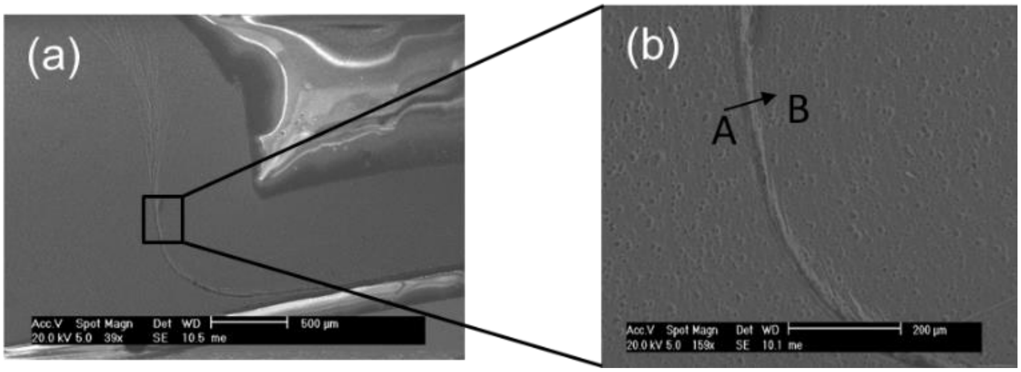

Figure 2-9. (a) Groove line shows up after etching (b) EDS line test from point A to point B

(Plunge speed 10 mm/min, dwell time 3 s)

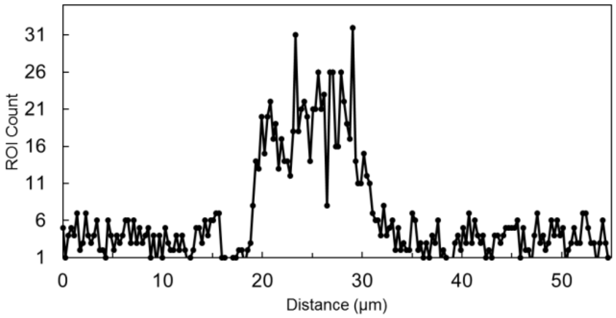

Figure 2-10. ROI Count for Zinc from EDS line test

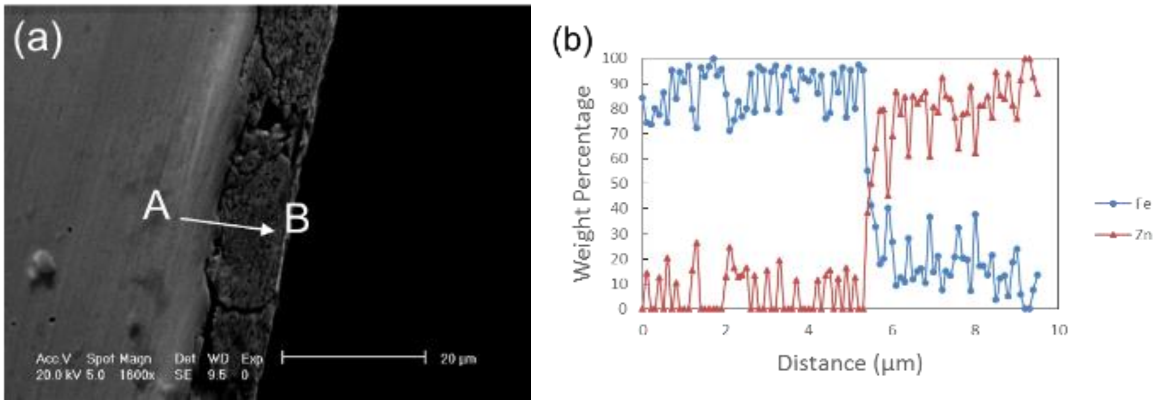

Figure 2-11. (a) EDS line test on the coating of steel (b) Element distributions from the test result

2.3.3 Microhardness

Hardness distribution on the joint cross section was measured and the corresponding results are shown in Figure 2-12. The results indicate that the hardness of the base steel is around 279 HV while that of the base aluminum alloy is only around 80 HV. However, a substantially higher hardness can be observed in the swirling structure region, which is approximately 400 HV on average and is 143% of that of the base steel. The hardness of Al-Fe IMC is generally at the range of 330 HV to 1013 HV [40, 88]. The hardness test is performed on the swirling structure, which is comprised of alternating thin layers of steel and IMCs. The tested results show that the hardness of the swirling structure is lower than that of the pure IMCs but higher than that of the steel. The associated high hardness indicates its brittle properties, which accordingly plays a major role in determining the overall weld strength.

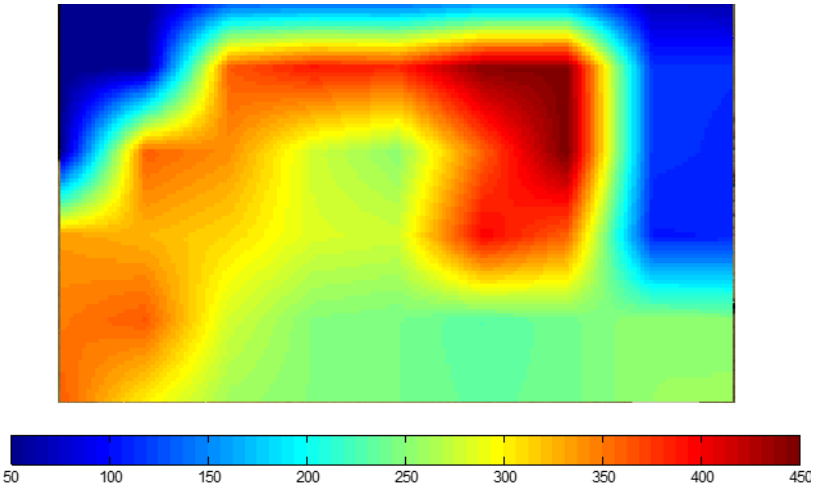

Figure 2-12. Vickers hardness distribution (Plunge speed 10 mm/min, dwell time 5 s)

2.3.4 Lap Shear Force

2.3.4.1 Effects of plunge speed on the joint strength

Effects of plunge speed on lap shear force of FSSW joints are shown in Figure 2-13 and the corresponding dwell time is 5 s. The shear force varies from 2443 N to 4083 N, which is approximately in the same range as that reported by Lathabai et al [71], where they performed FSSW for joining similar aluminum alloy 6060. The maximum shear force of 4083 N is achieved at a plunge speed of 10 mm/min. Moreover, it can be observed that joint shear force improves with increasing plunge speed from 2 mm/min to 10 mm/min. On the other hand, further increasing the plunge speed will reduce the joint strength. Plunge speed is closely related to the total amount of heat input during FSSW. Slower plunge speed corresponds to a longer contact period between shoulder and material, which therefore leads to a greater amount of heat generation. Accordingly, more IMC is generated at the interface between aluminum and steel and it results in an adverse effect on weld strength. In the meantime, when the plunge speed reaches an excessively higher value, axial plunge force increases as shown in Figure 2-5. The corresponding large plunge force will initiate cracks on the brittle IMCs in the swirling structure during the welding process, which are left as initial defects on the weld before tensile tests. Figure 2-14 shows the cross-sectional view of joint with the feature of the fractured hook, where the cracks occur on the swirling structure and significantly deteriorate joint quality. This joint is obtained under the plunge speed of 15 mm/min.

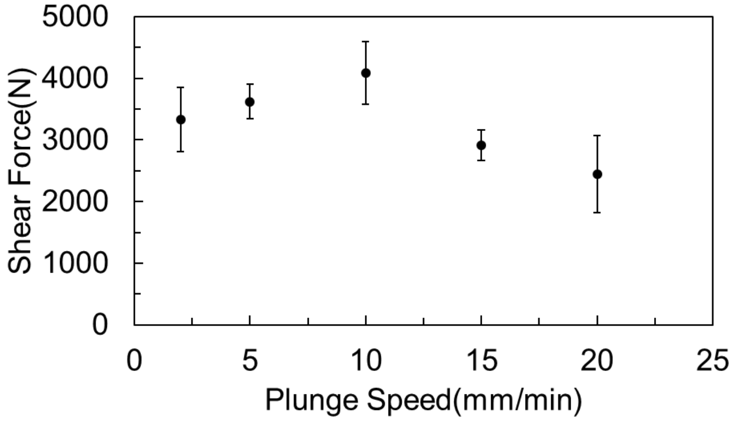

Figure 2-13. Joint shear force from different plunge speeds

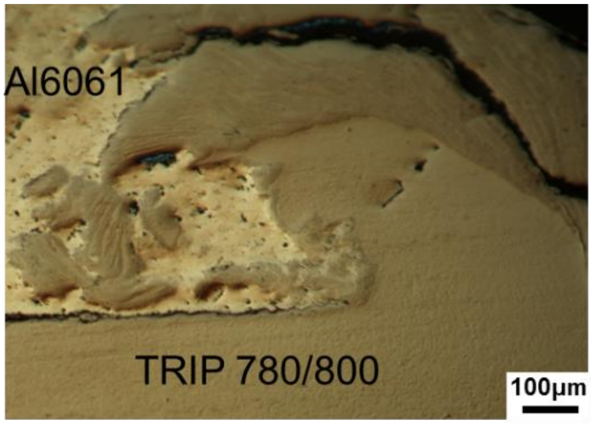

Figure 2-14. Cross-sectional view of FSSW joint with plunge speed of 15mm/min

2.3.4.2 Effects of the plunge speed on the thermal history

To further investigate the effects of the plunge speed during the welding process, three thermocouples are placed under the TRIP steel to monitor the thermal history. The experimental setup is shown in Figure 2-15. The distance from the thermocouples to the center of the welding zone is 1.5 mm, 3.0 mm and 4.5 mm, respectively. Each measurement is repeated for three times. The temperature is measured under the plunge speed of 2 mm/min, 10 mm/min and 20 mm/min, respectively.

The recorded temperatures profiles are shown in Figure 2-16. It can be noticed that the temperature profiles recorded at different locations follow a similar pattern during the welding process. The temperature profiles relate closely to the welding process and it can be divided into three regions. At the beginning of the welding process, only the rotating tool pin touches the top material and the heat is generated from the friction between the tool pin and the aluminum sheet. It can be observed from the temperature profile that the temperature increases slowly during this period. When the plunge depth increases gradually to a certain level, the tool shoulder touches the aluminum sheet, which significantly increases the contact surface and a lot of heat releases due to a significant amount of friction force. The slope of the temperature increases with a much higher heat generation rate at this period. Finally, when the heat generation rate equals to the heat dissipation rate in the welding process, the welding temperature remains in a steady value.

Comparing the temperature profiles under different plunge speeds, it can be seen that a higher plunge speed results in lower peak temperature. For a higher plunge speed, it results in a shorter time for both the heat generation and heat dissipation, which are competitive factors for the temperature history. The experimental results indicate that the heat generation is dominant when compared with the heat dissipation in the welding process.

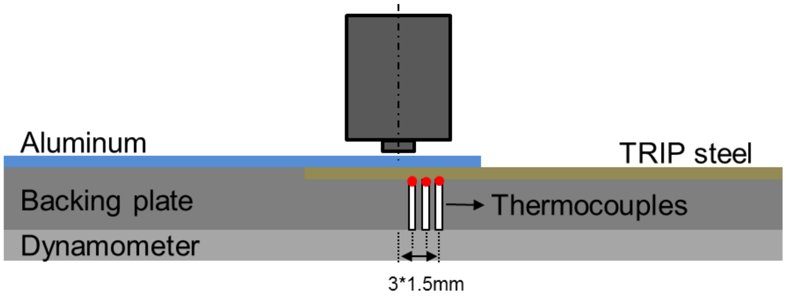

Figure 2-15: Illustration of the experimental setup for measuring the temperature

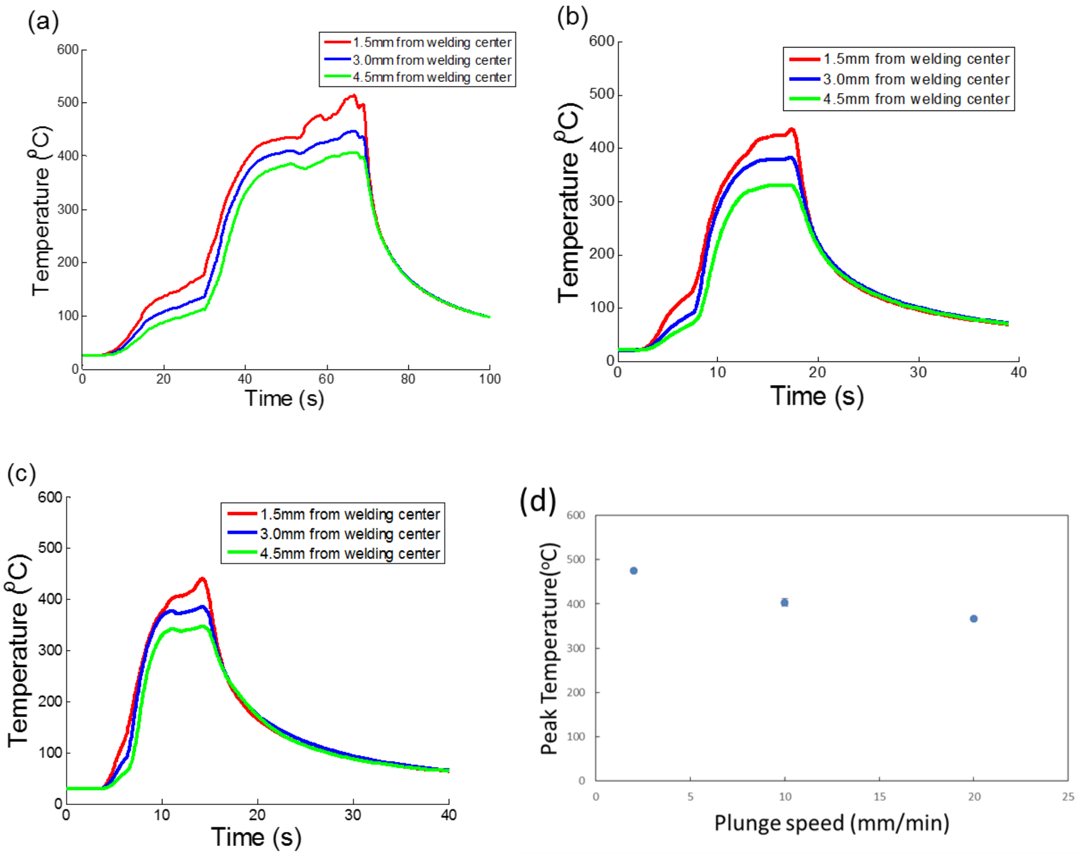

Figure 2-16: Temperature profile with different plunge speed: (a) 2 mm/min (b) 10 mm/min (c) 20 mm/min; (d) Peak temperature with different plunge speeds

2.3.4.3 DOE analysis on effects of weld parameters

To further understand the influence of dwell time and plunge speed on FSSW of aluminum alloy to TRIP steel, the design of experiments (DOE) method was applied. DOE is an efficient approach to identify the most crucial process parameter for the final output, understand interactions between different parameters and optimize process conditions. In this study, a three-level full factorial design was adopted to investigate the effects of dwell time and plunge speed on weld characteristics. The experimental matrix is listed in Table 2-2 in the previous section.

In addition, a statistical analysis of variance (ANOVA) was performed to evaluate the relative significance of different process parameters as well as their interactions on the joint tensile strength. The confidential level was set as 95% for all intervals. The calculated results of degrees of freedom (DF), the total sum of squares (SS), and the mean squares (MS) for each involved parameter are summarized in Table 2-3. Furthermore, the F value is determined as the average of mean square deviation due to each parameter divided by the mean of squared error, which is the ratio of "average between different treatments" to "average within one treatment". The P value is the probability that the null hypothesis is rejected when it is actually true and the null hypothesis is that there is no difference in mean values for different levels of a tested factor. Smaller P value means the parameter is a more significant factor in affecting the output.

From Table 2-3, among the investigated range of operation parameters, the dwell time is shown to be the most influential factor on joint tensile strength, followed by plunge speed and then the interaction of these two parameters. The P value for dwell time is only 0.002, which further indicates it as a dominant factor.

Main effects of different process parameters on joint tensile strength are shown in Figure 2-17. The total average joint strength obtained from all welding conditions is plotted as a baseline value for reference. From Figure 2-17 (a), it can be observed that the overall effects of plunge speed averaged from different levels of dwell time are consistent with the result in Figure 2-13, which is for a specific dwell time of 5s. Maximum joint strength can be achieved at an intermediate level of plunge speed and either too high or too slow plunge speed will reduce joint strength.

Figure 2-17 (b) shows the main effects of dwell time averaged under various plunge speeds. It can be observed that the shear force decreases monotonically as dwell time increases. The dwell time of both 1 s and 5 s yields a higher strength than the average baseline value. Comparing Figures 2-17 (a) and (b), dwell time has an evidently larger influence on the joint strength, as is also indicated by the result of F value in Table 2-3.

Interaction plot of the processing parameters is given in Figure 2-18. At dwell time of 1 s, the weld strength decreases with increasing plunge speed, which can be attributed to the associated large plunge force, as discussed in the previous session. The large plunge force increases the possibility of formation of cracks in the swirling structure thus the joint strength is reduced. For the dwell time of 5 s, the weld strength increases with the increasing plunge speed in the beginning but then decreases. This can be explained as the followings: at relatively low plunge speed, an excessive amount of heat can be generated during the plunge stage, which produces extra undesirable IMCs on the interface between steel and aluminum. The thick layer of brittle IMCs greatly deteriorates the joint quality. On the other hand, when the plunge speed reaches a higher value as 15 mm/min, the associated larger plunge force generates initial crack defects, as in the condition of a shorter dwell time. To reduce the prejudicial effects of both these factors, an intermediate value of plunge speed therefore corresponds to the best joint performance. Finally, for the case of 10 s dwell time, the weld strength increases as the plunge speed increases. It can be considered from the aspect that a longer dwell time increases the IMC thickness due to the larger amount of frictional heat input during dwell stage. Less heat generation with faster plunge speed in plunge stage can restrain IMCs formation and consequently improve joint strength. As described above, the effects of different process parameters on weld strength are closely related to both the associated heat input and the plunge force.

Table 2-3. ANOVA of the weld strength with different process conditions

Source	DF	SS	MS	F-Value	P-Value
Plunge Speed	2	1342589	671294	3.26	0.062
Dwell Time	2	3521958	1760979	8.55	0.002
Plunge Speed*Dwell Time	4	2404500	601125	2.92	0.05
Error	18	3705991	205888		
Total	26	10975038			

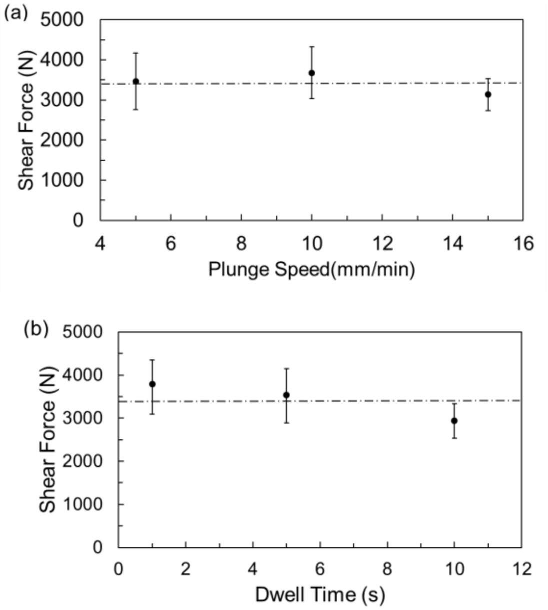

Figure 2-17. Main effects of different plunge speeds and dwell time on joint shear force

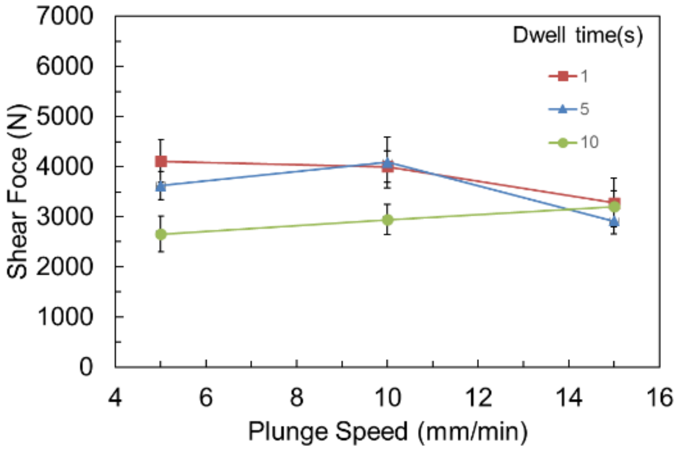

Figure 2-18. Interaction plot of different plunge speeds and dwell time on joint shear force

2.3.5 Failure Mode

According to the literature, there are two major failure modes for FSSW joints, including nugget pull out and cross nugget failure. Regarding nugget pull out failure, cracks are generated in the shoulder area and propagate around the weld nugget, which leaves the nugget intact and corresponds to a ductile fracture surface. Regarding the cross nugget failure, the fracture happens across the weld nugget and leaves a relatively brittle fracture surface [25, 89, 90]. In this study, the cross nugget failure was the only observed failure mode, as shown in Figure 2-19 (a). The left side of Figure 2-19 (a) shows a top view of the weld on a steel sheet and the right is a back side view of aluminum. The direction of the applied test load with regard to weld specimens is illustrated in Figure 2-19 (b). It can be noticed that on the right side of the nugget, the aluminum top sheet is subjected to tensile loading. This force tries to pull aluminum away from the nugget. Due to the existence of a considerable amount of brittle IMCs in the swirling structure, cracks are first initiated in this region, as shown in the cross sectional view in Figure 2-20 (a). It is obtained from an interrupted loading condition and corresponds to the beginning stage of tensile test. The cracks then propagate along the interface between the swirling structure and steel and the joint eventually failed as shown in Figure 2-20 (b). To further clarify the explanations above, the entire loading process on this right side of the nugget is illustrated schematically in Figure 2-21.

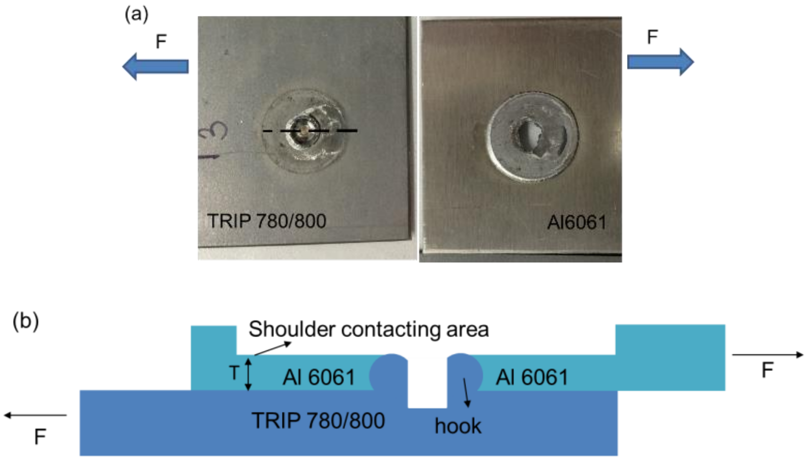

Figure 2-19. (a) Cross nugget failure mode (b) Schematic illustration of tensile shear test

On the left side of the nugget, the applied force is trying to push the aluminum sheet towards the nugget, which results in a compressive stress state in aluminum. As illustrated in Figure 2-22, the compressing force is applied to point 1 and then cracks are generated on the swirling structure in the top region of the hook. Based on the stress state analysis, the compressive stress results in a large shear stress component in the 45^o plane, which leads the cracks to propagate along this path and the fractured geometry is shown in Figure 2-23. It can also be noticed that the aluminum sheet was tilted upward with a small angle, which is more obvious in the bottom region as marked by point 2. A different failure mechanism on the left side was reported by Liyanage et al [41]. In their study, the fracture was initiated at the interface between aluminum and steel sheet and then propagated to the key hole. In this study, the formed hook provides a sufficiently high resistance to the compressive force, which helps prevent cracks from propagating to the keyhole.

Figure 2-24 (a) compares the relative strength between tensile and compressive side of the weld nugget. An enlarged view of the fracture region is provided in Figure 2-24 (b). It can be observed that the fracture was already initiated on the right tensile side while steel and aluminum were still connected on the left compressive side. This indicates that fracture first happened on the tensile side and the specimen eventually failed when the compressive side was completely sheared through. Figure 2-25 shows SEM analysis on the fractured surface at the backside of aluminum sheet. The cleavage characteristics imply a brittle fracture mechanism, which is very likely to be related to the fracture path through the IMC layer in the swirling structure of the hook.

Based on the previous discussions, there are three major factors that affect the joint strength. The first is hook geometry. A strong hook is necessary to avoid nugget fracture. The second factor is the remaining thickness of aluminum after penetration of the tool shoulder, which is denoted as T in Figure 2-19 (b). Increasing the remaining aluminum thickness can reduce the effectively applied loading stress on the weld cross section, which tolerates a higher loading force before the joint failure. The third one is the amount of IMCs in the swirling structure as it determines the fracture strength on the tensile side of the nugget.

Figure 2-20. Cross section view of the fracture: (a) At the beginning of tensile test: Cracks formed in the IMCs, (b) At the end of tensile test: Cracks propagate and fracture occurs

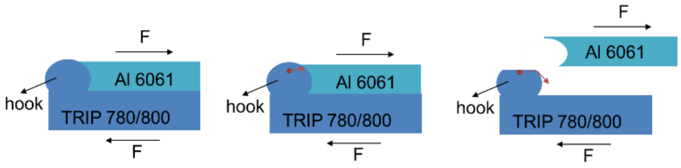

Figure 2-21. Illustration of the failure process in the right side of the nugget, where the aluminum is subjected to tensile stress

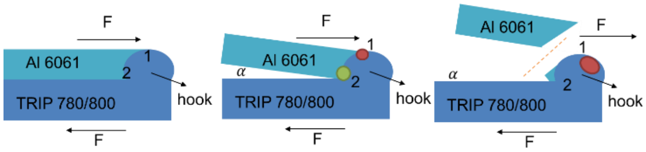

Figure 2-22. Illustration of the failure process in the left side of the nugget, where the aluminum is subjected to compressive stress

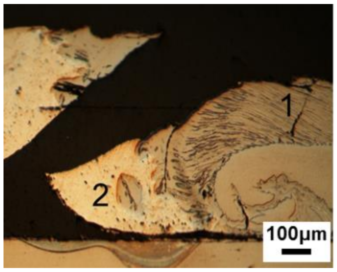

Figure 2-23. Failure on the left side of the nugget

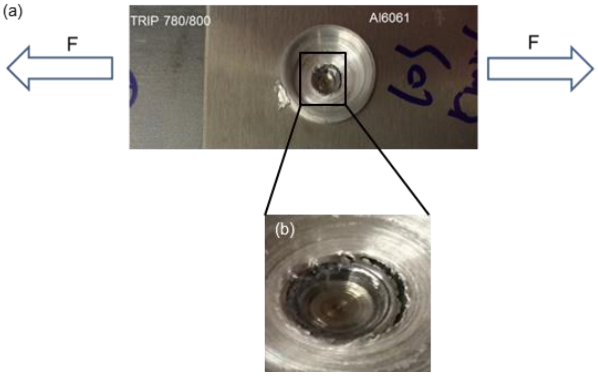

Figure 2-24. (a) Failure happened at the tensile side while the compressive side is still connected (b) Enlarged view of the fracture region

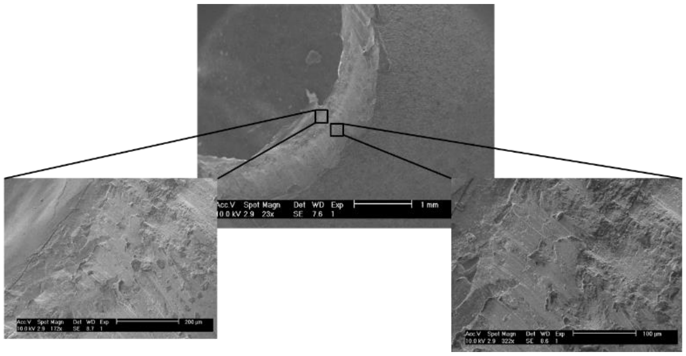

Figure 2-25. SEM images of the fracture surface on the aluminum side

2.4 Conclusions

Friction stir spot welding has been shown to be applicable for joining aluminum alloy 6061 to TRIP 780/800 steel. To understand the joining mechanism, the joint cross section was characterized using both an optical microscope and SEM. A hook feature with a swirling structure exists on the joint cross section. EDS analysis on the swirling structure shows that it is comprised of alternating thin layers of steel and IMCs. The bonding mechanisms of the FSSW between the steel and aluminum includes both the mechanical bonding and chemical bonding, which means that the steel inserts into the aluminum matrix and the IMCs are generated between the steel and aluminum interface.

Regarding the effects of different process parameters, a full factorial experimental design matrix has been established and the results are analyzed through the analysis of variance. It is shown that the dwell time is a more influential factor in determining joint strength when compared with plunge speed. The effect of plunge speed on the welding strength depends on the dwell time since the weld strength actually depends on the competing factors of heat generation and plunge force. Large amount of heat input under low plunge speed would result in the formation of excessive IMCs at Al/Fe interface and decrease the weld strength. On the other hand, large plunge force associated with high plunge speed can generate initial cracks in the IMCs, which become weld defects.

During tensile tests, cracks were first initiated in the IMCs on the tensile side and then propagated along the path between the swirling structure and the hook. The joint finally failed when the aluminum sheet in the compressive side of the weld nugget was sheared through along the 45^o plane. Furthermore, a cleavage feature occurs on the fractured surface and the cross nugget failure is the only observed failure mode.

CHAPTER 3

THERMAL MECHANICAL MODELING ON FRICTION STIR SPOT WELDING OF DISSIMILAR MATERIALS BASED ON COUPLED EULERIAN-LAGRANGIAN APPROACH

3.1 Literature Review

During the FSSW process, highly coupled thermal-mechanical material behavior is involved in the weld zone. Since the FSSW is basically a variant of FSW, modeling works about the FSW process can provide some insights to solve the highly nonlinear problem with severe mesh distortion associated with the FSSW process. The FSW process includes the plunge stage and the welding stage, both of which are well studied from the literature.

Regarding the welding stage, Nandan et al. [91] developed a three-dimensional thermo-mechanical model, which calculated the temperature and plastic flow fields during the FSW of mild steel. They applied the equations of conservation of mass, momentum and energy to solve the three-dimensional temperature and plastic flow fields. The temperature dependent thermal conductivity, specific heat and yield strength are also considered in the model. They observed that significant plastic flow occurred near the tool and convection was the primary mechanism of heat transfer. The temperature and torque value predicted by the model agreed well with their experimental results.

Zhu and Chao [92] studied the variation of the temperature and residual stress in friction stir welding of 304L stainless steel. In their study, the authors applied the finite element code WELDSIM to finish the simulation and two welding cases were studied. From their results, the authors determined the unknown heat source with the acquired data based on the experimental results. They also presented a good match with the experimental data and the corresponding residual stress was also investigated. They also indicated that the fixture in the FSW should be considered in the modeling work as the residual stress decreased significantly after the fixture was released. Regarding the energy transfer during the welding process, the authors mentioned that 50% of the total mechanical energy transferred to increase the temperature of the workpiece.

Cho et al. [93] also carried out a three-dimensional thermo-mechanical simulation for friction stir welding of 409 ferritic stainless steel. They found the heat was generated mainly near the interface between the tool and the workpiece and the shear deformation texture was significantly developed around the tool. The calculated temperature profile agreed well with their experimental data. They also indicated that the changes of the microstructure characteristics during the FSW process were predictable while adopting the developed numerical model.

Schmidt et al. [47] was able to model the friction stir welding process with ABAQUS/Explicit as they applied the Arbitrary Lagrangian-Eulerian (ALE) formulation and Johnson-Cook material law in their model. The steady-state solution of the heat generation and the plunging force correlated well with the experimental observations. They also indicated that the development of the sticking contact at the probe and matrix interface was critical to the success of modeling the welding process.

Chiumenti, et al. [94] also applied the ALE method to study the thermal and mechanical response of the FSW process. In their study, the streamline-upwind/Petrov-Galerkin(SUPG) formulation and the orthogonal subgrid scale (OSS) technique were implemented to stabilize the convective term in the energy equation. The triangular/tetrahedral meshes were used for the domain discretization. Besides, they applied a tool with a triflute pin in the model work and both the thermal and mechanical response was validated by the simulated results.

Kim et al. [95] developed a thermal-mechanical simulation of the friction stir welding of AA5083-H18 sheets through a commercial Finite Volume Method (FVM) code (STAR-CCM+). They proposed that a proper thermal boundary condition at the interface between the workpiece and the backing plate was critical to obtain the accurate temperature distribution. The authors also mentioned that the CFD was a useful tool to handle large deformation in the numerical model as well as reduced the computational cost when compared with the Lagrangian and ALE approaches. However, they also pointed out that it was difficult to handle realistic frictional boundary conditions at the interface and the rate sensitivity was also an important factor that should be taken into consideration.

Aval et al. [96] built up a model to predict the temperature and residual stress distribution during the friction stir welding of dissimilar aluminum alloys. The residual stress of the welded samples was measured using the hole-drilling technique. From their modeling work, the authors mentioned that around 10% to 12 % of the plastic deformation was transferred into the heat. They also indicated that the mechanical constraints produced by the welding fixture had a significant effect on the residual stress distribution and a higher amount of heat input per unit length resulted in a higher residual tensile stress.

Different from the welding stage, the plunge stage of the FSW is a transient process, which requires time-dependent variables in the governing equations and a larger computational capacity. Mandal et al. [46] studied the plunge stage of the friction stir welding through both experimental and numerical analysis, which was implemented in the ABAQUS/Explicit program. Johnson-Cook law was adopted to describe the material behavior and the ALE approach was utilized to eliminate the issue of excessive element distortion. A good correlation of axial force was observed between the modeling work and experimental results for the first 5 s of the plunge stage. In addition, they indicated that the model had the potential to analyze the tool wear during the welding process.

Awang et al. [97] used the ABAQUS/Explicit program to build up a finite element model to simulate and analyze the friction stir spot welding of Al alloy. The adaptive mesh techniques were employed to refine the mesh with severe distortion, which could avoid the numerical divergence and early abortion of the computation process. The mass-scaling algorithm was also adopted to improve the computational efficiency. The maximum temperature was over-predicted and the reason was likely to be the inaccurate value of the friction coefficient.

Zhang et al. [98] developed a finite element method to model the three-dimensional material flow in the FSW of Al 6061-T6 with the ABAQUS/Explicit program. In their study, they showed that the equivalent plastic strain distribution in the nugget zone could be affected by the variations of the axial load on the shoulder and the maximum material velocity could be increased with the increase of the translational velocity. Besides, the ALE methods are commonly used by other researchers [99-106] for the modeling of friction stir welding process.

In the existing modeling works, either similar material or dissimilar aluminum alloys are the commonly studied workpiece material types. A limited amount of numerical analysis was performed for welding of dissimilar materials, especially for the plunge stage. Liu et al. [107] studied the FSW for joining Al 6061 to TRIP 780 steel with the ABAQUS/Explicit program. Their estimated axial force correlated well with the experimental results at the beginning of the plunge stage. The calculated temperature and stress distribution on the workpiece at different plunge depths were also shown.

In this chapter, the FSSW process for joining aluminum alloy 6061-T6 to TRIP 780 steel is modeled based on the Coupled Eulerian-Lagrangian (CEL) approach. Compared with pure Lagrangian or the Arbitrary Lagrangian-Eulerian (ALE) approach, the CEL is an efficient approach for modeling manufacturing processes that involve severe material deformation. The results of the numerical analysis are compared with experimental measurements in the aspects of material distribution, axial force and thermal history. To further validate the developed model, a different FSSW tool geometry is investigated and the corresponding results are compared.

3.2 Analytical Formulations

3.2.1 Governing Equations

In the developed model, a multi-material Eulerian formulation is applied to the workpiece region, where different material properties are assigned to each Eulerian element. The governing equations that describe the conservation of mass, momentum and energy during the welding process are:

$$\frac{\partial \rho}{\partial t} + \boldsymbol{\nabla} \cdot (\rho \boldsymbol{v}) = 0 \qquad \text{Eq. 3-1}$$

$$\rho \left(\frac{\partial v}{\partial t} + \boldsymbol{v} \cdot \boldsymbol{\nabla} \boldsymbol{v} \right) = \boldsymbol{\nabla} \cdot \boldsymbol{\sigma} + \rho \boldsymbol{g} \qquad \text{Eq. 3-2}$$

$$\rho C_p \left(\frac{\partial T}{\partial t} + \boldsymbol{v} \cdot \boldsymbol{\nabla} T \right) = \boldsymbol{\nabla} \cdot (K \boldsymbol{\nabla} T) + \boldsymbol{\nabla} \cdot (\boldsymbol{\sigma} \cdot \boldsymbol{v}) + q'' \qquad \text{Eq. 3-3}$$

Where ρ is the material density, $\boldsymbol{v}$ is the velocity vector, $\boldsymbol{\sigma}$ is the deviatoric stress tensor, $\boldsymbol{g}$ is the gravity vector, C_p is the specific heat, K is the material thermal conductivity, T is the temperature, q'' is the volumetric heat generation rate. The mass conservation Equation (3-1) describes the relation between the net rate of mass outflow through the control surface and the mass change rate inside the control volume. In the momentum conservation equation, the change of momentum equals the summation of spatial time derivative of the Cauchy stress tensor with the product of material density and the gravity, which represent the effect of surface and body force on the momentum respectively. The energy equation contains the net flux of heat conduction into the element, the rate of work done on the element from the surface force as well as the volumetric heat generation rate. Operator splitting algorithm is commonly employed in the CEL formulation to split the governing equations into Lagrangian step and Eulerian step [108-110]. The general resulting equation for the Lagrangian step can be formed as:

$$\frac{\partial \varphi}{\partial t} = S \qquad \text{Eq. 3-4}$$

and the corresponding Eulerian step is:

$$\frac{\partial \varphi}{\partial t} + \boldsymbol{\nabla} \cdot \Phi = 0 \qquad \text{Eq. 3-5}$$

Where φ is a general solution variable, Φ is the flux function and S is the source term accordingly. Regarding equations (3-1) through (3-3), the corresponding solution variables are material density, velocity and temperature. The second term on the left side of the equations (3-1) through (3-3) are regarded as the flux function term Φ. The terms on the right side of the equations (3-1) through (3-3) are considered as the source term S. The calculation of Lagrangian step is similar to that in the general explicit finite element program, which determines the change of mass, energy, momentum and other relative terms based on the applied internal and external force. In the Eulerian step, the highly deformed mesh generated from the Lagrangian step will recover to its original shape. The transport algorithms [108] are applied to adjust the mass, energy and momentum for the flow of the material between adjacent elements. A graphical representation of the two steps is shown in Figure 3-1 below:

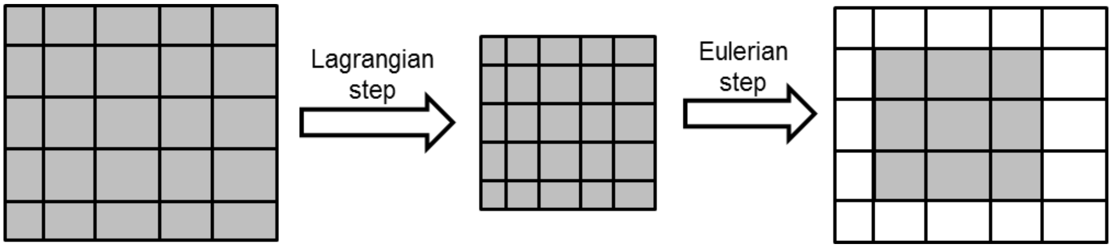

Figure 3-1. Two steps of the operator splitting algorithm in the CEL formulation [109]

3.2.2 Lagrangian Step

In the Lagrangian step, the central difference method is applied to update the spatial coordinate $\boldsymbol{x}$ and the velocity $\boldsymbol{u}$[109]. It essentially comes from the Taylor series expansion, where an arbitrary function f at $t^{n+1/2}$ can be evaluated as:

$$f^{n} = f^{n+1/2} - f'^{n+\frac{1}{2}}\left(\frac{1}{2}\Delta t^{n+\frac{1}{2}}\right) + \frac{1}{2} f''^{n+\frac{1}{2}}\left(\frac{1}{2}\Delta t^{n+\frac{1}{2}}\right)^{2} - \cdots \tag{Eq. 3-6}$$

$$f^{n+1} = f^{n+1/2} + f'^{n+\frac{1}{2}}\left(\frac{1}{2}\Delta t^{n+\frac{1}{2}}\right) + \frac{1}{2} f''^{n+\frac{1}{2}}\left(\frac{1}{2}\Delta t^{n+\frac{1}{2}}\right)^{2} + \cdots \tag{Eq. 3-7}$$

Then, the subtraction of the above two equations yields:

$$f^{n+1} - f^{n} = f'^{n+\frac{1}{2}}\left(\Delta t^{n+\frac{1}{2}}\right) + O\left(\frac{1}{2}\Delta t^{n+\frac{1}{2}}\right) \tag{Eq. 3-8}$$

Where $O(\frac{1}{2}\Delta t^{n+\frac{1}{2}})$ represents the truncation error in the central difference method. By replacing the arbitrary function f^{n} with the spatial coordinates $\boldsymbol{x}$ and the corresponding derivative term with the velocity $\boldsymbol{u}$ in Equation (3-8), the following can be obtained:

$$\boldsymbol{x}^{n+1} = \boldsymbol{x}^{n} + \Delta t \boldsymbol{u}^{n+1/2} \tag{Eq. 3-9}$$

Similarly, the change of velocity $\boldsymbol{u}$ can be described as:

$$\boldsymbol{u}^{n+1/2} = \boldsymbol{u}^{n-1/2} + \Delta t \boldsymbol{M}^{-1}\{\boldsymbol{F}_{int} - \boldsymbol{F}_{ext}\} \tag{Eq. 3-10}$$

Where $\boldsymbol{M}$ is the diagonal mass matrix, $\boldsymbol{F}_{int}$, $\boldsymbol{F}_{ext}$ are the internal and external force vector. $\boldsymbol{F}_{ext}$ is calculated from interaction between the tool and workpiece through penalty method, which is described below.

3.2.3 Penalty Method

In the developed model, the tool is treated as a rigid Lagrangian body and the workpiece is assigned with Eulerian elements. The penalty method [110-112] was employed to calculate the interaction force between the Lagrangian body and Eulerian elements. The underlying principles are described as the followings: the movement of the rigid tool compels the kinematic deformation of the workpiece, in return, a reactive force generated by the workpiece is applied to the tool. At the beginning of the calculation, the position of the tool is checked to ensure it is within the workpiece region. The penalty displacement is then calculated based on the relative motion of the tool and the workpiece. Finally, the reaction force applied to the tool can be expressed as:

$$\boldsymbol{F}_p = k_p \boldsymbol{d}_p$$

Eq. 3-11

Where $\boldsymbol{d}_p$ is the penalty displacement and k_p is the penalty stiffness. The penalty displacement $\boldsymbol{d}_p$ is described as the penetration depth of the tool into the workpiece, which is illustrated in Figure 3-2 and can be calculated based on Equation (3-12)

$$\boldsymbol{d}_p = \Delta t[\boldsymbol{v}_r - \sum_{i=1}^{4} N_i(r,s)\boldsymbol{v}_i] \cdot \boldsymbol{n}$$

Eq. 3-12

Where Δt is the time step, $\boldsymbol{v}_r$ is the velocity of the tool, N_i is the shape function for node i, r,s represent the current location of this node, $\boldsymbol{n}$ is the outward normal vector at the Lagrangian node. The penalty stiffness k_p can be calculated based on Equation (3-13):

$$k_p = \varepsilon \cdot \frac{\tilde{m}}{\Delta t^2}$$

Eq. 3-13

Where ε is a constant multiplier, $\widetilde{m}$ is the smaller value of Eulerian and Lagrangian mass. With the penalty force calculated above, the force applied at node i in the Eulerian element can be expressed as:

$$\boldsymbol{F}_{E,i} = N_i \boldsymbol{F}_p \qquad \text{Eq. 3-14}$$

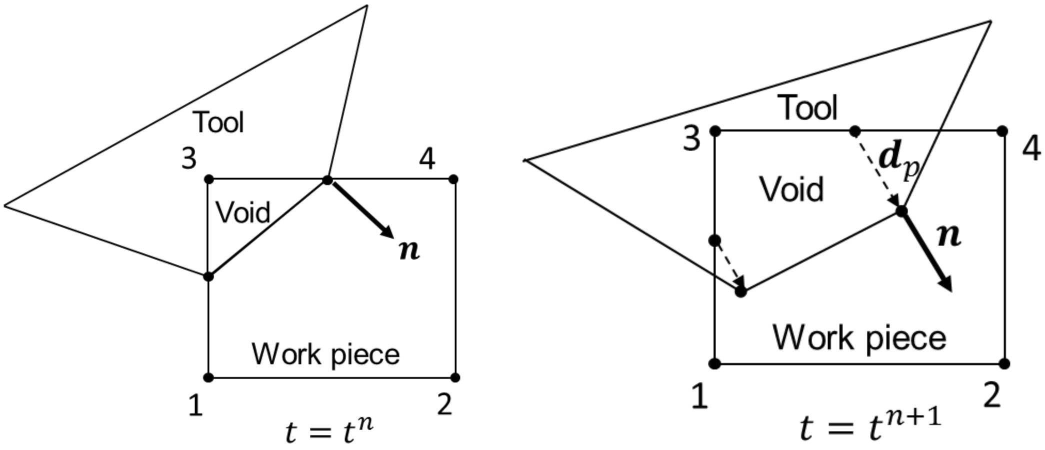

Figure 3-2. Illustration of the penalty displacement in Penalty method

3.2.4 Mixture Theory

Mixture theory [108, 113] is applied for modeling this dissimilar friction stir spot welding process, which accounts for the involved two materials in the weld zone, i.e., aluminum alloy and TRIP 780 steel. In the mixture theory, the deformation rate of materials in the element is equal to that of the unit element. The limitation of this same volumetric strain rate assumption is related to the void in the element. When the element experiences a compressive stress state, the void will also be compressed in the element. On the other hand, in the real situation, the volume of the void will reach zero when the compression ratio is high instead of only being reduced to a smaller value. To address this limitation, Benson [109] proposed a method, which permits the void material to be compressed preferentially when the element is in a compression state. In his method, the compression ratio is calculated by

$$R = max\left\{\frac{V^{n+1}}{V^{n}}, \frac{\min(V^{n+1}, \sum_{M=1}^{N_{material}} V_M^n)}{\sum_{\square=1}^{N_{material}} V_M^n}\right\} \qquad \text{Eq. 3-15}$$

where R is the compression ratio, V^n, V^{n+1} is the volume of element at steps n and $n+1$, V_M^n, V_M^{n+1} is the volume of material M at steps n and $n+1$, $N_{material}$ is the total number of materials in the element. Based on the compression ratio, the volume of the void after compression can be calculated as:

$$V_v^{n+1} = V^{n+1} - R\sum_{M=1}^{N_{material}} V_M^n - \sum_{v'=1}^{v-1} V_{v'}^n \qquad \text{Eq. 3-16}$$

where V_v^{n+1} represents volume of void at step $n+1$, and the value of v changes from 1 to the maximum number of voids in the model. v' represents the summation of the void from 1 to $v-1$, the last term in the Equation (3-16) turns to zero since there is only one kind of void involved in the modeling. The value of V_v^{n+1} is constrained to be a nonnegative value. The volume of each material inside the element after compression can be determined by：

$$V_M^{n+1} = RV_M^n \qquad \text{Eq. 3-17}$$

In this study, there are only two different materials and one type of void, the equations above can be simplified as:

$$R = max\left\{\frac{V^{n+1}}{V^{n}}, \frac{\min(V^{n+1}, V_{Al}^n + V_{Steel}^n)}{V_{Al}^n + V_{Steel}^n}\right\} \qquad \text{Eq. 3-18}$$

$$V_v^{n+1} = V^{n+1} - R(V_{Al}^n + V_{Steel}^n) \qquad \text{Eq. 3-19}$$

$$V_{Al}^{n+1} = RV_{Al}^n \qquad \text{Eq. 3-20}$$

$$V_{Steel}^{n+1} = RV_{Steel}^n \qquad \text{Eq. 3-21}$$

During the calculation, if at the time step $n+1$ the compressed element volume V^{n+1} is larger than the total volume of steel and aluminum at time step n, the void will be compressed at the same ratio as the element. Otherwise, the void will be removed from the element. For example, assuming the initial volume fraction of steel, aluminum and void in the unit element are 50%, 30%

and 20% and the total volume of the element is 1. After compression, the element volume is 0.9, which is still larger than the initial total volume of steel and aluminum before compression. In this case, the materials and void in the element are compressed at the same compression ratio and the corresponding volume of steel aluminum and void are 0.45, 0.27 and 0.18. In contrast, if the element volume is 0.7 after compression, the void will be removed and the volume of steel and aluminum in the element will be 0.7*5/8 and 0.7*3/8 respectively. A schematic illustration is shown below in Figure 3-3.

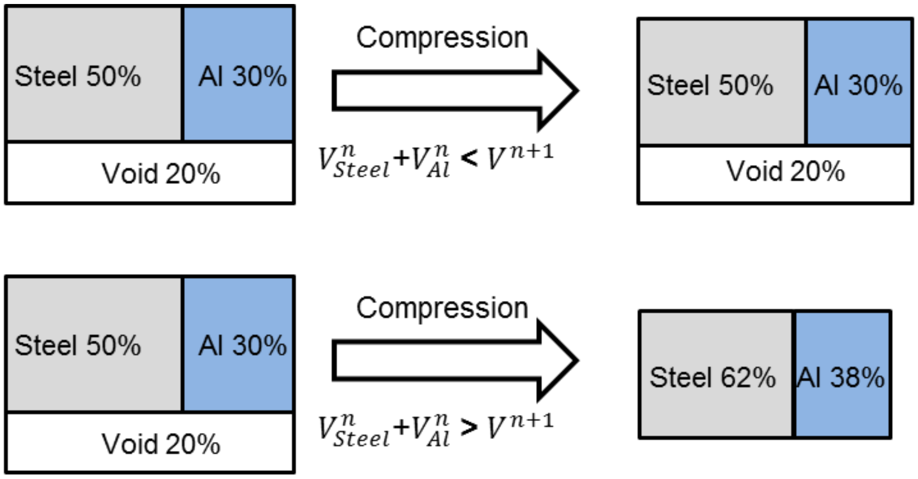

Figure 3-3. Schematic illustration of the mixture theory applied in this model [109]

3.2.5 Johnson-Cook Material Model

During FSSW process, materials in the welding zone are subjected to severe plastic deformation at both high temperature and relatively high strain rate. Johnson-Cook's constitutive law is therefore employed in this model to describe the effect of strain, strain rate and temperature on the material flow stress:

$$\sigma_e = \left(A + B\bar{\varepsilon}_{pl}^{n'}\right)\left(1 + C ln\frac{\dot{\bar{\varepsilon}}_{pl}}{\dot{\varepsilon}_0}\right)\left(1 - \hat{T}^{m'}\right) \qquad \text{Eq. 3-22}$$

$$\hat{T}^{m'} = \begin{Bmatrix} 0 \\ \frac{T-T_{ref}}{T_{melt}-T_{ref}} \\ 1 \end{Bmatrix} \quad for \quad \begin{matrix} T < T_{ref} \\ T_{ref} \leq T \leq T_{melt} \\ T > T_{melt} \end{matrix} \qquad \text{Eq. 3-23}$$

where $\bar{\varepsilon}_{pl}$ is the effective plastic strain, $\dot{\bar{\varepsilon}}_{pl}$ is the effective plastic strain rate, $\dot{\varepsilon}_0$ is the normalizing strain rate and its value is commonly chosen as 1 s^{-1}, T_{melt},T_{ref} are material melting temperature and reference temperature with the value of 20℃, A, B, C, n' and m' are material constants, which are listed in Table 3-1 based on literature. The first term of the equation 3-22 is basically the power law, which describes the effect of strain on the flow stress. The influence of the effective strain rate and temperature is accounted for by the second and third term respectively.

Table 3-1. Material constants used in the Johnson-Cook's model

Material	A	B	n'	C	m'	T_{melt} (℃)
Aluminum 6061 [114]	293.4	121.26	0.23	0.002	1.34	582
TRIP 780 steel [107]	780	1429	0.79	0.014	0.76	1400

3.2.6 Modified Coulomb's Friction Law

The frictional behavior at the interface between the tool and workpiece is described by the modified Coulomb's friction law, which takes into consideration of both sticking and sliding conditions [48, 115]. In the sliding condition, the frictional shear stress τ_{shear} is the product of friction coefficient and the contact pressure p, which is calculated based on the penalty method described in the previous session. However, if the friction shear stress calculated from this method is larger than the material shear flow stress, the sticking condition is indicated and the τ_{shear} is then assigned with the material shear flow stress. To consider the involved two materials, the variable α, which is the volume fraction of aluminum, is introduced. α is calculated from the mixture theory and the distribution is obtained through the Piecewise Linear Interface Calculation(PLIC) [116]. The described friction model can be expressed as:

$$\tau_{shear} = \begin{Bmatrix} [\alpha \cdot \mu_{Al} + (1-\alpha) \cdot \mu_{Steel}] \cdot p \\ \tau_{max} \end{Bmatrix} \quad \text{Eq. 3-24}$$

$$for \begin{matrix} [\alpha \cdot \mu_{Al} + (1-\alpha) \cdot \mu_{Steel}] \cdot p < \tau_{max} & sliding\,region \\ [\alpha \cdot \mu_{Al} + (1-\alpha) \cdot \mu_{Steel}] \cdot p > \tau_{max} & sticking\,region \end{matrix} \quad \text{Eq. 3-25}$$

Where

$$\tau_{max} = \frac{\alpha \cdot \sigma_{Al} + (1-\alpha) \cdot \sigma_{Steel}}{\sqrt{3}} \quad \text{Eq. 3-26}$$

$\sigma_{Al}, \sigma_{Steel}$ represent the flow stress of aluminum and steel, which are calculated by the Johnson-Cook's model. μ_{Al}, μ_{Steel} are the friction coefficients for the aluminum and steel.

3.3 Experimental Details

The overall experimental configuration is illustrated in Figure 3-4. The welding temperature is measured by several K-type thermocouples embedded below the workpiece. A Kistler dynamometer is mounted below the backing plate to measure the axial plunge force. The aluminum sheet is placed on the top of the steel. A steel plate with an extruded metal ring is applied to clamp the workpiece during the welding process, as shown in Figure 3-4. The thickness of both materials is 1.5mm. The welding tool is made of tungsten carbide with 10% cobalt and the hardness of the tool material is 91.8 HRA. The tool consists of a non-threaded cylindrical pin and a flat shoulder surface. The diameter of the shoulder is 12.7 mm and the diameter of the tool pin is 3.7 mm with a pin length of 1.2 mm. During the welding process, the tool axis is aligned with the center of the overlapping area of the aluminum and steel sheets.

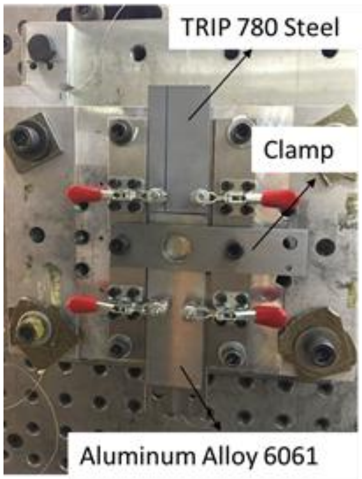

Figure 3-4. Fixture setup for the welding process

The measurement of temperature and welding force are repeated three times. The preset welding parameters include 2000 rpm for the rotation speed and 10 mm/min for plunge speed. The zero plunge depth is defined at the position where the end surface of the tool pin begins to touch the aluminum top surface. The total plunge depth into the workpiece is 1.9 mm and accordingly the plunge depth into steel is 0.4 mm.

3.4 Finite Element Model

The numerical analysis of the dissimilar materials FSSW process is performed in the Abaqus/Explicit program. To improve the computational efficiency, only the overlapped region of the workpiece is modeled with the dimensions of 40mm*40mm*4mm, as shown in Figure 3-5. The workpiece is meshed with 8-node thermally coupled Eulerian elements (EC3D8RT) and a total of 126,720 elements are generated. Generally, a higher mesh density is beneficial to the calculation accuracy. However, it will also increase the total computational time. In order to achieve a proper balance between computational time and calculation accuracy, a refined circular mesh is assigned in the center region of the welding zone with a diameter of 16mm, which is larger than the diameter of the tool shoulder. This enables a more accurate calculation of the material flow at the dissimilar material interface and better capture of the interaction between the tool and the workpiece. A relatively coarse mesh is assigned to the outside region of the workpiece to save the computational time.

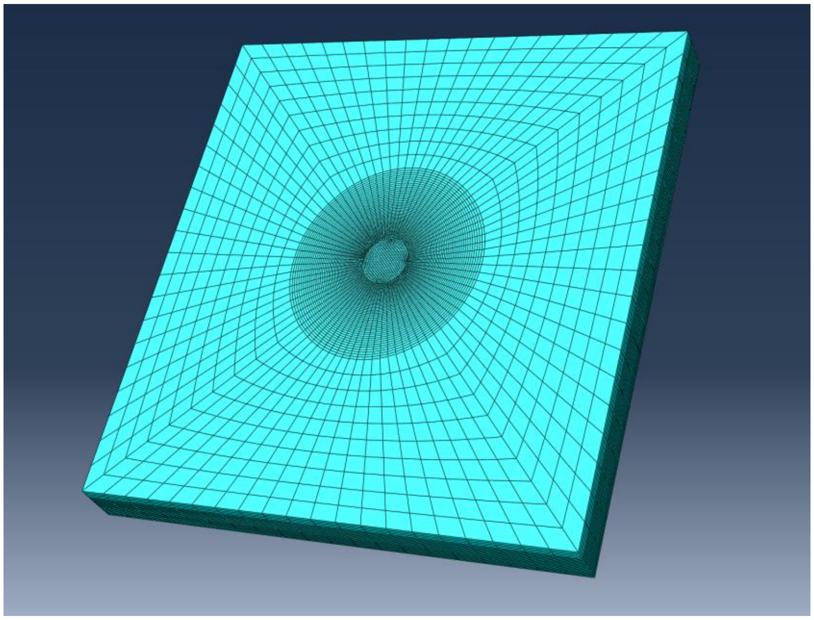

Figure 3-5. Geometry and mesh of the workpiece in the model

The welding tool is modeled as a rigid Lagrangian body and the tool geometry is the same as that in the experimental configuration. The chamfer on the tool is set as 5^{o}. The mesh of the tool is shown in Figure 3-6 and there are a total of 28,135 elements. The boundary conditions and initial temperature profiles are applied to the reference point of the tool, which is created at the center tip of the tool pin. The material assignment is schematically illustrated in Figure 3-7, which shows that the computational domain is split into three layers. The material properties of steel and aluminum are assigned to the bottom and middle layer with a thickness of 1.5mm and the top layer is left as a void in the model. The function of the void layer is to capture the material flow of the aluminum and steel, which can be extruded outside of the workpiece region due to the plunge motion of the tool. In this model, the rotation speed of the tool is 2000 rpm and the plunge speed is 10mm/min, which are the same as the experimental conditions. According to Ulysse et al.[117] and Al-Badour et al.[49], 90% of the plastic deformation energy is converted into the heat. Heat partition between the tool and workpiece is set as 0.5 [97, 118]. The interface between steel and aluminum is assumed to share the same temperature. The four sides and bottom surfaces of the workpiece are constrained with all degrees of freedom. Heat convection coefficient of the workpiece at the four sides and the top surface is 30 $w/(m^2 \cdot ℃)$ [119]. The heat transfer condition between workpiece and backing plate is also simplified with a lumped heat convection coefficient of 1000 $w/(m^2 \cdot ℃)$ [47, 120].

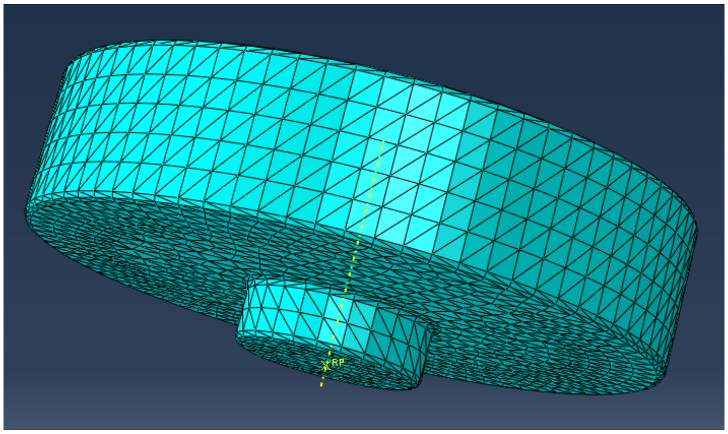

Figure 3-6. Geometry and mesh of the welding tool in the model

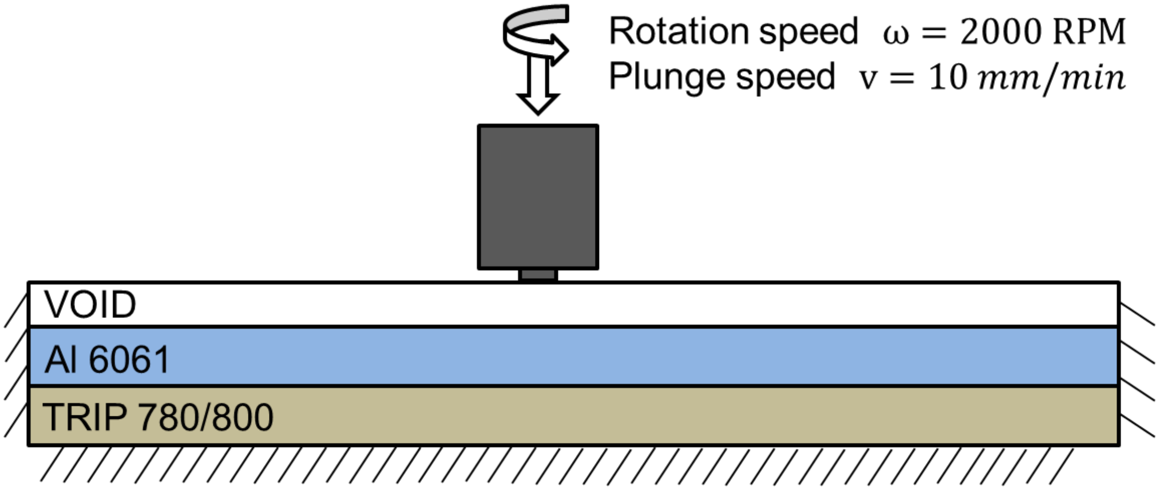

Figure 3-7. Material assignment and boundary conditions in the model

3.5 Results and Discussion

3.5.1 Welding Geometry

A typical cross section of the weld obtained from experiments and an enlarged view of the hook generated around the welding nugget are shown in Figures 3-8 (a) and 3-8 (b). At the same time, the material distribution at the end of the plunge stage calculated from the numerical model is shown in Figure 3-8 (c), where the steel is represented with red color and aluminum is shown in blue color.

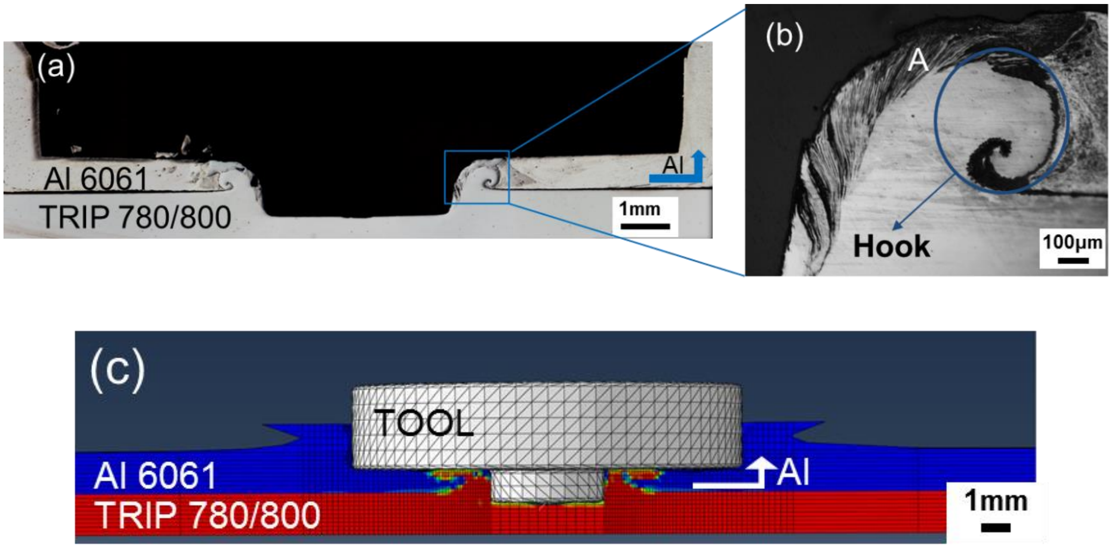

Figure 3-8. (a) Cross section view of the welding nugget (b) Geometry of the hook (c) Cross section view of the modeling result

Comparing the results obtained from the experiment and the modeling work, the overall material distribution from the modeling work is in good agreement with the experimental observation. From Figure 3-8(c), it can be noticed that the base material deforms due to the plunge motion of the rigid tool. The material assignment can be noticed from the cross section view of the modeling work. The top layer is assigned as void with a thickness of 1mm. The function of this void layer is to capture the material flow of the aluminum and steel that can be extruded outside of the workpiece region due to the plunge motion of the tool. The extruded aluminum can be captured only within the range of the void. It is the reason why there is only a limited amount of the extruded material can be seen in the modeling. In both Figure 3-8 (a) and Figure 3-8 (c), a hook structure is generated and the squeezed aluminum is accumulated around the tool. The hook mainly comes from the extruded steel, which is bent by the tool shoulder.

However, some discrepancies still exist regarding the hook geometry between the experimental work and modeling. A relatively larger hook is predicted in the numerical results when compared with that from experimental observations. Several possible reasons are related to the larger hook formation in the modeling results.

First is the inaccurate constitutive material model, which is insufficient to describe the material behavior, especially for the TRIP steel under the combined condition of high temperature and pressure. This inaccuracy accordingly will affect the material flow pattern. Second, the formation of IMC is not considered in this developed model. From the experimental cross section view in Figure 3-8 (b), IMCs formed at Al-Fe interface on the top side of the hook isolate the contact between steel and aluminum, which restrains the steel to flow further along the tool shoulder and results in a smaller hook structure. On the other hand, in the numerical model, the steel is extruded by the tool pin during the welding process, and the extruded steel flows along the tool pin and tool shoulder without generating any IMCs. Third is the simplified frictional behavior at the contact between tool and workpiece materials. In the sliding region, a constant friction coefficient as shown in Equation (3-24) can be inaccurate.

However, the separate effects of these three major factors on the material flow will need to be further investigated. The larger hook form in the model also results in a larger contact area between the tool shoulder and extruded steel. As can be shown in the following analysis of the force and thermal history, this macrostructure feature plays a major role in determining the maximum plunge force and temperature at the final stage of the welding process. To further understand the formation mechanisms of the hook structure, the material distribution at different plunge depths from the modeling results are extracted and shown in Figure 3-9.

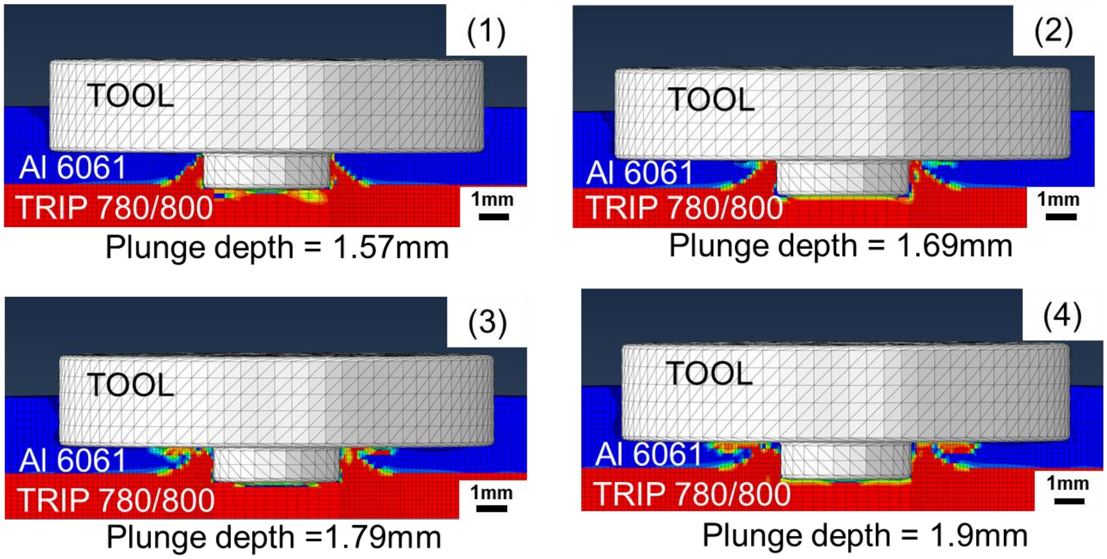

Figure 3-9. Material distribution at different plunge depths

From Figure 3-9 (1) – (4), it can be noticed that the hook is generated around the nugget zone due to the downward motion of the tool pin, which squeezes the steel and results in an upward flow of the materials. In the meantime, the axial compression motion from the tool shoulder will bend this portion of the extruded steel, which results in a hook structure. A certain amount of aluminum at top surface is also squeezed outward and accumulates around the tool shoulder, which is the same as that we observed from Figure 3-8(a).

As the plunge depth increases gradually, the steel at the bottom is extruded by the tool pin, which almost fully surrounds the pin at the plunge depth of 1.57mm. When the tool pin reaches a deeper position at 1.69mm, a portion of the extruded steel starts to be bent by the tool shoulder and embeds into the aluminum matrix. It is the moment when the initial hook is formed. Since the joint strength of FSSW of aluminum and steel primarily relies on the mechanical clamping via the hook and the material bonding via the intermetallic at the interface [81], the formation of this hook structure after plunge depth of 1.69mm will be beneficial for the FSSW joint. As the welding tool reaches a deeper plunge depth, more steel will be extruded by the tool pin, which results in a stronger hook structure. Finally, at the plunge depth of 1.9mm, the generated hook inserts into the aluminum matrix and it forms a solid mechanical bonding between the steel and aluminum.

3.5.2 Axial Welding Force

The force history obtained from the modeling work is plotted in Figure 3-10 together with the experimental measurements. The overall calculated force history is in reasonable agreement with the experimental data. The change of force as a function of plunge depth is a result of interactions between the moving tool and flowing materials. At the beginning of the welding stage, the axial force continuously increases. During this period, only the aluminum matrix is stirred as the tool pin touches the top surface of the aluminum and gradually moves into the workpiece. The axial force increases due to the growing amount of deformed aluminum. As the tool penetrates deeper into the aluminum matrix, the heat generated by the friction and plastic deformation will soften the aluminum, which decreases the plunge force. In the modeling results, the calculated force is larger than the experimental data at the plunge depth around 0.3mm.

From the modeling perspective, the inaccurate material properties of aluminum found in the literature and the simplified heat transfer coefficient can be a potential cause for this force difference, which may result in a lower welding temperature. From the experimental perspective, one of the possible reasons is related to the stiffness of the working machine. Since the backing plate of the machine is in a vertical position, the backing plate will be tilted with a small angle as the tool plunges into the workpiece, which decreases the measured force. When the plunge depth reaches 1.0mm, the plunge force starts to increase rapidly, which is observed from both the experiments and the numerical analysis. The tool pin length is 1.2mm, which indicates the tool shoulder does not touch the top surface of the aluminum matrix at this position. One of the possible explanations for this phenomenon is that the extruded aluminum in the top region starts to contact with the tool shoulder at the plunge depth of 1.0mm. As the contact reacting area increases drastically, the axial plunge force accordingly increases at a much faster rate. This hypothesis explanation can be shown by the modeling results at plunge depth of 1.0mm.

Figure 3-11 presents a cross-sectional view of the weld at this moment, which shows that the tool shoulder is compressing against the extruded aluminum in the top region. At the final stage of the force history, the force reaches the peak value as the tool shoulder fully contacts with the aluminum matrix and the tool pin penetrates into the steel on the bottom. The maximum force is overpredicted in the modeling work. There are several factors that need to be considered to account for the discrepancies between the calculated and measured force.

First, the contact between the hook and the tool shoulder is different. In Figure 3-8(b), the experimental results show that the tool shoulder touches the swirling structure on the top side of the hook, where the swirling structure is comprised of alternating thin layers of steel and IMCs. While in the modeling work, the tool shoulder contacts with the steel directly and ignores the formation of IMC, which will increase the welding force at the final stage. Second, the hook geometries are different. A backward curved hook structure can be observed from the weld cross section in Figure 3-8(b), while the hook distributes along the tool shoulder in the modeling results, which leads to a larger contact area and plunge force. Finally, the constitutive material model is less accurate for steel compared with that for aluminum. For the plunge depth from 1mm to 1.8mm, the tool shoulder area compresses the aluminum sheet. At the same time, the tool pin deforms a small amount of steel.

Regarding the large difference in the contact area of the tool shoulder surface and tool pin surface, the resistance force on the tool shoulder is likely to dominate in this part of the force history, which is more related to the material properties of the aluminum. In this way, the modeling data follows well with the experimental data. At a later plunge stage, a larger amount of steel is involved in deformation, its inaccurate material model starts to affect more the force history and therefore a larger deviation is observed. All of these are related to the limitations of the modeling work when trying to simulate the complex welding process. They include the ignorance of the formation of IMC, the larger volume of the hook and the inaccurate material model for workpiece materials.

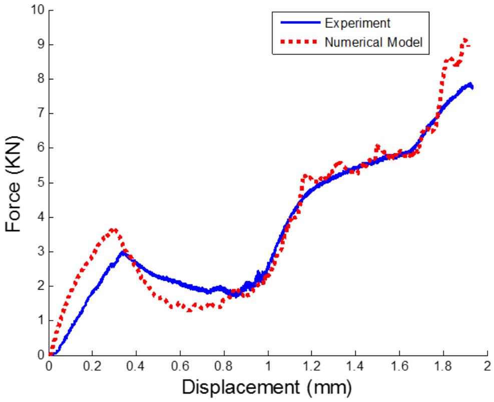

Figure 3-10. Comparison between experimental results with calculated force history

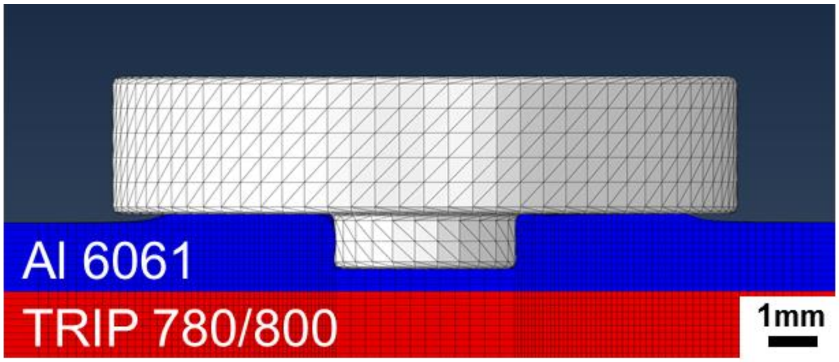

Figure 3-11. Aluminum distribution at the plunge depth of 1.0mm

3.5.3 Thermal History

The comparison between calculated thermal history data and the experimental measurements is shown in Figure 3-12. The temperature profile is measured at 1.5mm away from the welding center. The calculated results follow the trend of the experimental results well at the beginning stage of the welding process and the divergence starts at a relative deeper plunge depth, which is similar to the trend of the calculated plunge force. The change of thermal history is closely related to the axial welding force and material flow during the welding process. In the beginning of plunge stage, where the plunge depth is roughly between 0 and 0.3mm, the temperature increases with a relatively small rate and the corresponding force increases fast. During this period, the tool pin is inserted into the aluminum matrix, the compressed aluminum generates resistance force and a limited amount of heat is generated from the friction between tool pin and aluminum workpiece. It can also be noticed that the calculated temperature is relatively lower than the measured temperature, which can be a reason why the calculated plunge force is larger than the experimental force at the plunge depth of 0.3mm in the perspective of material thermal softening effect. As the plunge depth increases, a larger portion of the tool pin inserts into the aluminum matrix and more heat is generated from both the friction and plastic deformation, which increases the temperature of the bulk material and decreases the plunge force due to the thermal softening of the workpiece. A rapid increase of the temperature is observed at the plunge depth around 1.0mm. As shown in Figure 3-11, this is the position where the extruded aluminum touches the tool shoulder and it significantly increases the contact area as well as the frictional heat generation rate between the tool and the base material, which releases a much larger amount of heat. The temperature is overestimated at the final stage of the welding process. The possible reasons that lead to the discrepancies are similar to that for the force estimtion at the final stage, which are mainly due to the ignorance of the formation of IMC, the larger volume of the hook and the inaccurate material model for workpiece materials. The overestimated peak temperature can also be found from the numerical model at different distances from the welding center, which is shown in Figure 3-12(b).

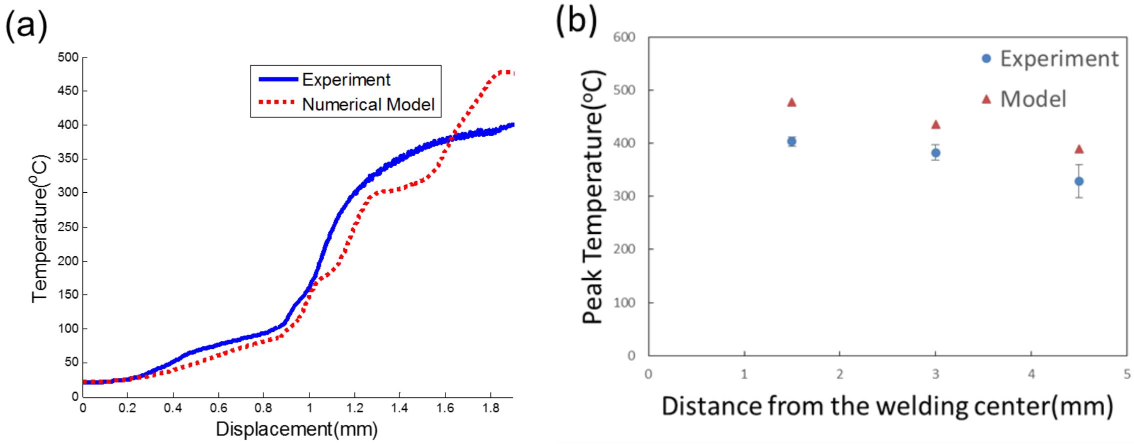

Figure 3-12. Comparison between the experimental work and the numerical model

3.5.4 Model Validation Using A Different Tool Geometry

The calculated force and thermal history of the previous tool geometry show good agreement with the experimental results. To further verify the developed model, a different tool geometry with a tool shoulder diameter of 6.5mm is investigated. The remaining welding parameters, including rotating speed, plunge depth and plunge speed are kept the same as the previous condition. The axial force recorded during the experiments is compared with the results from the numerical analysis in Figure 3-13. A good correlation can be observed with different tool geometry. Since the pin length of the new tool is the same as the previous one, the force curves share a similar trend at the beginning of the welding process between Figure 3-10 and Figure 3-13. At the plunge depth of 1 mm, a small amount of force increment also occurred in Figure 3-13 since the extruded aluminum starts to touch the tool shoulder. Compared with the force history from the previous tool geometry at the similar plunge depth, the force increment is relatively smaller in the current condition. The reason behind this is that the current tool has a smaller shoulder diameter, which results in a smaller contact area between the shoulder surface and the extruded aluminum. The force increases dramatically at the plunge depth of around 1.5mm, where the tool pin begins to touch the steel on the bottom. The similar phenomenon is not clearly observed in the modeling results for the previous tool due to the difference between the diameter of the tool shoulder, which further indicates that the resistance force from the deformation of the steel is dominant in the force history when using a smaller tool shoulder. The calculated force is slightly higher than the experimental measurement after the plunge depth of 1.61mm when the extruded steel touches tool shoulder in Figure 3-14. Different from the modeling result in Figure 3-10, the overestimated force starts at a relatively earlier plunge depth. This is again the result of the smaller shoulder diameter. Before the tool shoulder touches the steel, the axial force applied to the shoulder mainly comes from the resistant force due to the deformation of the aluminum. After the tool pin extrudes the steel, a portion of the aluminum contacting with the tool shoulder is replaced with steel, which increases the resistant force. For the tool with a smaller shoulder diameter, a relatively larger fraction of the aluminum is replaced with the steel, which leads to a higher increment in the axial plunge force. This can also be demonstrated by the calculated material distribution in Figure 3-14, where the plunge depth is 1.61mm. Similar to the previous tool geometry condition, the numerical analysis still calculated a larger force at the end of the welding stage.

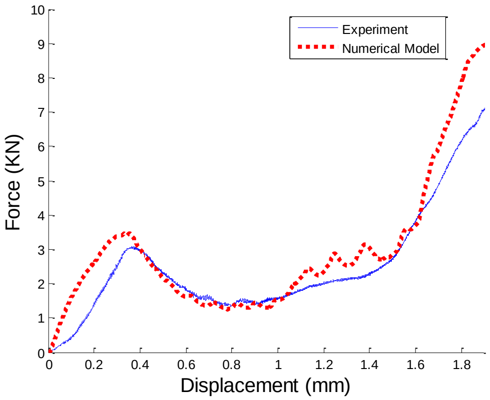

Figure 3-13. Comparison between experimental results with calculated force history with shoulder diameter of 6.5mm

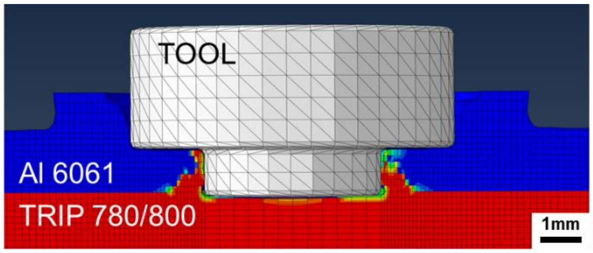

Figure 3-14. Material distribution of extruded steel at a plunge depth of 1.61mm

3.6 Conclusions

The welding process of FSSW between the aluminum alloy 6061-T6 and TRIP 780 steel is analyzed based on CEL method and mixture theory. The calculated force and temperature are shown together with the material flow during the welding process. The following conclusions can be drawn:

1. The modeling of the friction stir spot welding between aluminum alloy 6061-T6 and TRIP 780 is successfully achieved while applying the Abaqus/Explicit with CEL approach.

2. The bulk material distribution of aluminum alloy and TRIP 780 steel in the modeling

work shows good agreement with the cross-section view of the experimental results, which includes the hook forms and inserts into the aluminum matrix, the aluminum alloy extruded by the tool shoulder.

3. The hook is observed on both sides of the welding nugget at the final stage of the welding process. However, the size of the hook in the modeling work is larger than the experimental observations, which is probably due to three main reasons, including the inaccurate material model, the ignorance of the formation of IMC and the simplified friction condition between the tool and workpiece materials.

4. Calculated force and thermal history from the modeling work correlate well with the experimental measurements. In the meantime, the change of the force and thermal history is investigated through the process while considering the interaction between the tool and workpiece.

5. The plunge force shows a rapid increase in both experimental results and modeling work at the plunge depth around 1.0mm. It can be explained from the modeling work that the tool shoulder touches the extruded aluminum matrix at the plunge depth of 1.0mm, which increases the contact area between the tool shoulder and the bulk material and leads to a higher resistance force.

6. A relatively larger plunge force and higher temperature are calculated at the end of the welding process. The possible reasons that lead to the discrepancies can be summarized as the following: the ignorance of the formation of IMC, the larger volume of the hook and the inaccurate material model for workpiece materials.

7. The developed model is validated with a new tool of a smaller shoulder diameter and the calculated axial force shows good agreement with experimental data.

CHAPTER 4
KEYHOLE REFILLED FRICTION STIR SPOT WELDING OF ALUMINUM ALLOY TO ADVANCED HIGH STRENGTH STEEL

4.1 Literature Review

The Friction Stir Spot Welding (FSSW) process has been introduced in the previous chapters, which is capable of making a solid joint between steel and aluminum. However, at the end of the conventional FSSW process, a large keyhole is left on the workpiece as an undesirable defect after retraction of the welding tool. To solve this problem, several keyhole removing approaches have been proposed in the literature. Zhao et al. [121] applied a refilled friction stir spot welding (RFSSW) process to weld 7B04-T74 aluminum alloy with the thickness of 1.9mm. Their welding tool was composed of three independent movable parts: a clamping ring, a sleeve and a pin. The process is illustrated in Figure 4-1 and the welding process can be described as the followings: In the first step, the clamping ring moves downward and presses the base material against the anvil on the bottom. In the second step, the sleeve rotates and plunges into the base material while the tool pin moves upward simultaneously. The frictional heat from the rotating sleeve plasticizes the workpiece materials and enables them to occupy the available space that is formed between the pin and sleeve. In the third step, the sleeve moves upward and the pin moves downward, which pushes the accumulated material back in to fill the keyhole. In the final step, the entire welding tool retracts without a keyhole left on surface. In their study, a tensile shear failure load of 11,921 N is reached for the joint when the plunge depth is 3mm. To eliminate the formation of the annular groove defect due to the material loss, a surface indentation with 0.2mm depth was required after the welding process. Reimann et al. [122] employed a similar RFSSW process to weld aluminum alloy 6061-T6 with the addition of a plug. The influence of gas shielding, heat treatments and the plug itself on the joint strength was analyzed based on the design of experiment and the analysis of variance (ANOVA) approach. The strengthened zone in the center of the welds increases joint strength but reduces the elongation. Cao et al. [123] welded 2mm thick aluminum alloy 6061-T6 sheet using the RFSSW process. They reported that the hook height in the weld structure was positively correlated with some process parameters including the rotation speed, joining time and plunge depth. After the statistical analysis of the data between the operating parameters and the welding strength, their ANOVA results showed that the plunge depth was the most dominant parameter in affecting the weld strength. This welding method is widely used by the other researchers[33, 63, 64, 124-129] to explore wider applications for this method.

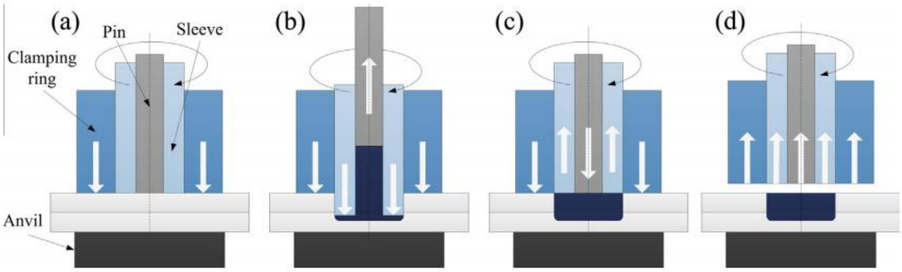

Figure 4-1 Schematic illustration of the refilled friction stir spot welding process [121]

In order to refill the keyhole associated with the regular FSSW process, several other approaches have been developed in addition to the RFSSW. Uematsu et al. [130] developed a probe hole refilled process to improve FSSW of T4 treated Al-Mg-Si aluminum alloy sheet with the thickness of 2mm. Their specially designed double-acting welding tool consists of an outside flat shoulder and an internal retractable probe. During the process, the welding tool is applied in the first step to perform the conventional FSSW. After that, the tool pin tip was retracted to the same height as the tool shoulder. The tool with the retracted pin, which forms a flat surface, is then plunged into the welding zone again to refill the keyhole. Joint tensile strength was shown to be improved by the re-filling process. However, the fatigue strength of the refilled joint remains approximately the same as that of regular FSSW joint. At high applied loads, the fatigue strength of the refilled joint is even lower, which can be explained from the observed plug type fracture.

Zhou et al.[131] developed a self-refilling friction stir welding (SRFSW) process to weld 316L stainless steel plate with a thickness of 10mm. As shown in Figure 4-2, the SRFSW process consists of multiple steps. In the first step, conventional FSSW process is performed, which includes plunging, stirring and retracting of the welding tool. In the following steps, the refilling process is carried out by a series of specially designed tools, which plasticizes the materials surrounding keyhole and gradually squeezes them back in. No obvious macro defects can be observed. Besides, the tensile strength and elongation of the refilled joint reached 112% and 82% of the base material. Sajed [132] developed a two-stage refilled friction stir spot welding (TFSSW) process to weld aluminum alloy 1100 with the thickness of 2mm. This process is quite similar to the SRFSW process. Instead of using a series of the welding tools, only two independent tools are required, including a conventional tool and a non-pin refilling tool. Their study showed that the rotation speed had the strongest effect on the joint strength for both conventional and refilled FSSW processes. The maximum tensile shear force of their obtained joints was 6.96kN.

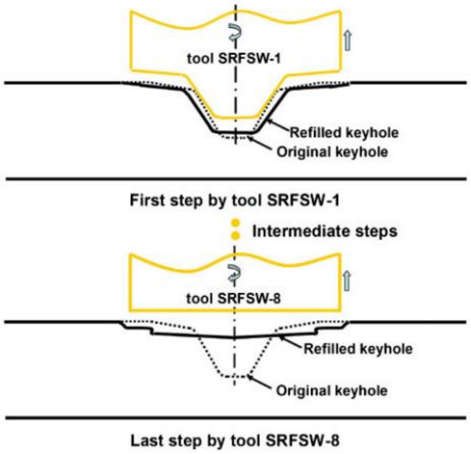

Figure 4-2 Schematic illustration of SRFSW process[131]

Among the existing works that improve the FSSW process by removing the keyhole, most of the applications focused on joining of aluminum alloys. A limited amount of the literature discussed improved technique for welding dissimilar materials. Chen et al. [133] applied RFSSW to make a joint between ZEK 100 Mg alloy and DP 600 steel. Their maximum tensile shear force of the joints reached 4.7kN. $FeAl_2$ was identified at the Mg/Fe interface, which significantly enhances the bonding between the insoluble Mg and Fe matrix. Dong et al. [134] applied RFSSW for joining Novelist AC 170 PX aluminum alloy to ST06 Z galvanized steel. Their maximum tensile shear force was 4.5kN and the majority of the samples failed in a shear brittle fracture mode. Regarding the cross-tension fracture of the joint, the maximum load reached 359N.

Despite the advantages of these improved FSSW processes that can eliminate keyholes, there are several related limitations. The RFSSW process requires a specially designed weld machine and welding tool, which directly increases the cost [132]. Besides, severe tool wear will occur when high strength materials are involved [133]. Regarding the TFSSW process, switching between different welding tools is time-consuming and the cost of tools is high [132].

In this research, a new keyhole refilled FSSW process is developed and applied for joining aluminum alloy 6061-T6 to Transformation Induced Plasticity (TRIP) 780 steel. This developed process is cost effective as it can be implemented on any CNC machine with a welding tool of simple geometry. Besides, a single welding tool can fulfill the joining process and switching welding tools is unnecessary. The joint strength is compared between refilled joint and the conventional FSSW joint. The geometry of the obtained weld is studied and the microstructure of the weld is characterized. Bonding mechanisms of the joint are further analyzed.

4.2 Experimental Configuration

4.2.1 Welding Procedure

In order to refill the keyhole after the welding process, a newly developed keyhole refilled FSSW process is performed in this chapter, which consists of two steps. In the first step, the regular FSSW is performed, where a rotating cylindric tool plunges into the base materials at a desired depth, dwells a certain amount of time and then retracts from the workpiece. In the second step, the retracted welding tool is shifted to a certain location away from the original keyhole. The tool then plunges into the base materials with a smaller depth and travels along a circular path surrounding the keyhole with a preassigned radius and traveling speed. In this way, the original keyhole can be refilled and finally the tool retracts with a much smaller new keyhole left on the weld. The process described above is shown in Figure 4-3. Principles of this joining process are further explained with a schematic illustration of the weld cross section in Figure 4-4. In Figure 4-4 (a), the original keyhole that corresponds to the geometry of the FSSW tool, including both the shoulder and pin features, is located in the center of the joint after the conventional FSSW step. In

Figure 4-4(b), after the keyhole refilled step is performed, the original keyhole is filled with aluminum alloy and a new small keyhole is left on top of the aluminum sheet.

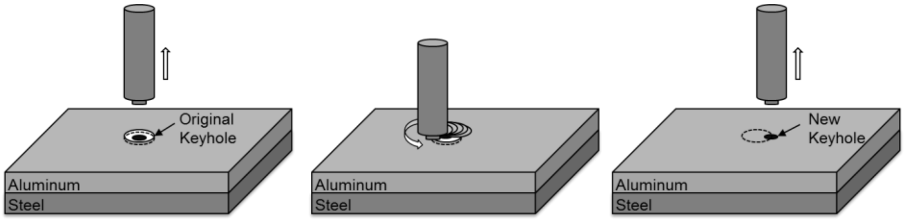

Figure 4-3. Schematic illustration of keyhole refilled FSSW process

Figure 4-4. Schematic illustration of the weld cross section of the keyhole refilled FSSW

4.2.2 Experimental Setup

The base materials in this study are aluminum alloy 6061-T6 and TRIP 780 steel with the thickness of 1.5mm. Chemical compositions of the aluminum alloy 6061-T6 are listed in Table 2-1. The yield strength of the aluminum alloy 6061-T6 is 241MPa. According to the previous works from Liu et al.[85], the yield strength of the TRIP 780 steel is around 780 Mpa and the ultimate tensile strength is around 1300MPa. Geometry and dimensions of the welding tool used in this study are same as the previous one, which is shown in Figure 2-1. In the same time, the samples are prepared according to the dimension specified in Figure 2-2. To evaluate the strength of the joints, lap shear tensile tests are performed using the 810 Material Test System (MTS) together with a digital controller. The specimen is loaded at a constant tensile speed of 1mm/min. To ensure the repeatability of the collected data, at least six replicates were performed in each welding condition. The weld samples are sectioned in the center. Then, they are mechanically ground with

300, 600, 1200 emery paper. After that, they are polished with 3μm, 1μm diamond and 0.03μm colloidal silica. Both optical microscope and scanning electron microscope (SEM) are applied for the characterization of the joint cross section. The energy dispersive X-ray spectroscopy (EDS) is utilized to analyze the elemental distributions at the interface between the steel and aluminum. Since the keyhole refilled FSSW consists of two steps, the operation parameters of each step are summarized in Tables 4-1 and 4-2 respectively. To find out a proper rotation speed for the refilled step, several trials have been made at the beginning stage of the experiment. When the rotation speed is chosen as 1000 rpm, the refilling quality is low due to lots of voids and a rough surface. The reason behind this is that the low rotation speed generates less heat, which in return constrains the material flow and lead to a poor joint quality. Thus, a higher rotational speed helps to enhance the material flow and to improve the joint quality. Therefore, a higher rotational speed is chosen in the refilled step. The traveling radius in Table 4-2 refers to the radius of the circular path during the keyhole refilling step. It is equal to the offset distance that the tool moves away from the center of the original keyhole after the regular FSSW step. In this study, the plunge depth is defined as the distance between the end surface of the tool pin and the original top surface of the aluminum sheet. During welding, the aluminum alloy sheet is placed on top of the TRIP 780 steel sheet and the experimental configuration is shown in Figure 4-5. As indicated in Figure 4-5, the welding tool is operated in the welding region for both the welding and refilling process.

Table 4-1. Process parameters for the conventional FSSW step

Rotation speed (rpm)	Plunge speed (mm/min)	Plunge depth (mm)	Dwell time (s)
1000	30	1.9	3

Table 4-2. Process parameters for the keyhole refilling step

Rotation speed (rpm)	Travelling speed (mm/min)	Plunge depth (mm)	Traveling radius (mm)
2000	30	1.3	6

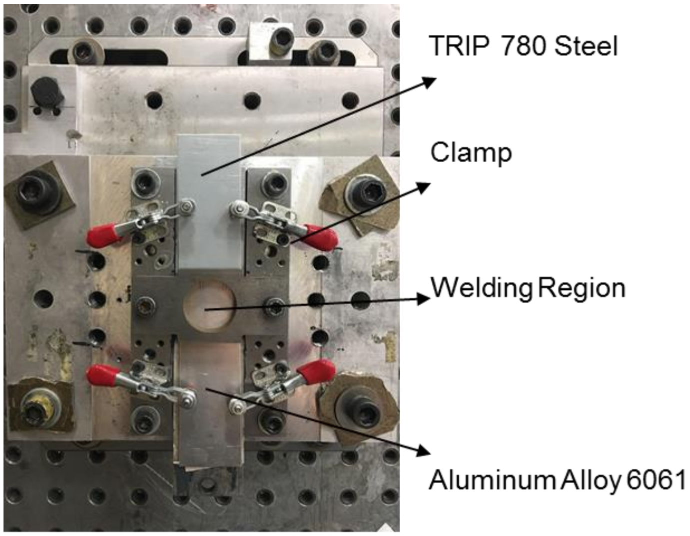

Figure 4-5. Fixture setup for the keyhole refilled FSSW

4.3 Investigation of the Keyhole Refilled FSSW

4.3.1 Weld Geometry

Successful joints can be obtained from the keyhole refilled FSSW process and macroscopic views of the weld are shown in Figure 4-6. Overall, no obvious cracks or other defects are observed at the contact interface between steel and aluminum. Regarding the refilling quality, it can be noticed from both the top view and the cross-sectional view of the weld that the original keyhole is basically filled with the aluminum alloy. On the other hand, a new small keyhole is left at the location where the welding tool retracts at the final stage. Based on the cross-section view of the weld, material flow during the entire process can be considered as the followings: In the conventional FSSW step, the aluminum is squeezed out and accumulates around the welding tool. After the tool is shifted to the periphery of the original keyhole and then plunges back into the aluminum sheet again in the refilling step, these accumulated aluminum is compressed beneath the tool shoulder surface. As the tool travels along the circular path, the compressed aluminum distributes uniformly under the tool and fills the original keyhole.

In this study, to ensure the aluminum can completely refill the original keyhole, the traveling radius (6mm) of the circular path is selected at a slightly smaller value than the tool shoulder radius (6.35mm), such that an overlapping region exists in the weld center. Despite the refilled keyhole, the top view and the cross-sectional view showed some defects on the top surface of the weld, which are generally located on the opposite side of the new keyhole relative to the original one. Magnified views of material distribution around the original keyhole region are shown in Figure 4-7(b)-(e). Voids are absent at the right and bottom sides of the original keyhole, which are located in the new keyhole region. However, some voids exist on the left bottom side of the original keyhole and the left region of the hook, which are located near the surface weld defect. These voids together with the surface weld defect are generated mainly due to the lack of base materials. The better filling quality near the new keyhole region can be explained based on two possible reasons. First, the generated new keyhole enables more aluminum to fill the original keyhole. Second, after the regular FSSW step, certain amount of aluminum materials are accumulated in the periphery of the original keyhole. At the beginning of the refilling step, the offset welding tool plunges into the aluminum alloy sheet, which compresses the accumulated aluminum back into the weld. This increases the amount of available aluminum materials that can be supplied to fill the space in this region where the tool retracts and the new keyhole forms. On the other hand, as the tool travels to the opposite side of the weld center, the accumulated aluminum is actually scraped off due to the motion of the tool instead of being smeared back into the weld. This reduces the amount of available materials to fill this side of the keyhole. Further experiments were performed by varying the starting position of the tool in the refilling step, or equivalently the position of the new keyhole. The geometry of the obtained welds shows that the surface defect is always located on the opposite side of the new keyhole regardless of its initial position, which helps validate the above explanations. To characterize the bonding condition between the steel and aluminum at the bottom region of the original keyhole, EDS analysis is performed along the line from point A to point B, as marked out in Figure 4-7(a). Corresponding results are shown in Figure 4-8. At the Al-Fe interface in this region, IMCs are hardly observable, which indicates that no chemical reactions occur between the steel and aluminum at the bottom region of the original keyhole. A previous study has been conducted in Chapter 2 to exam the welding quality of the conventional FSSW process [135]. A typical cross-section view of the conventional FSSW joint is shown in Figure 2-6. Comparing to the conventional welding process, the keyhole is effectively refilled after the refilling process, as shown in Figure 4-6 (b). Another feature that should be mentioned is the bonding area between the steel and aluminum increases. According to Figure 2-6(c), there is a gap label B located outside the tool shoulder region, which indicates that there is no bonding between the steel and aluminum. In contrast, in the keyhole refilled FSSW joint, the bonding area between the steel and aluminum significantly increases and covers the entire original tool shoulder region, as can be observed in Figure 4-6 (b).

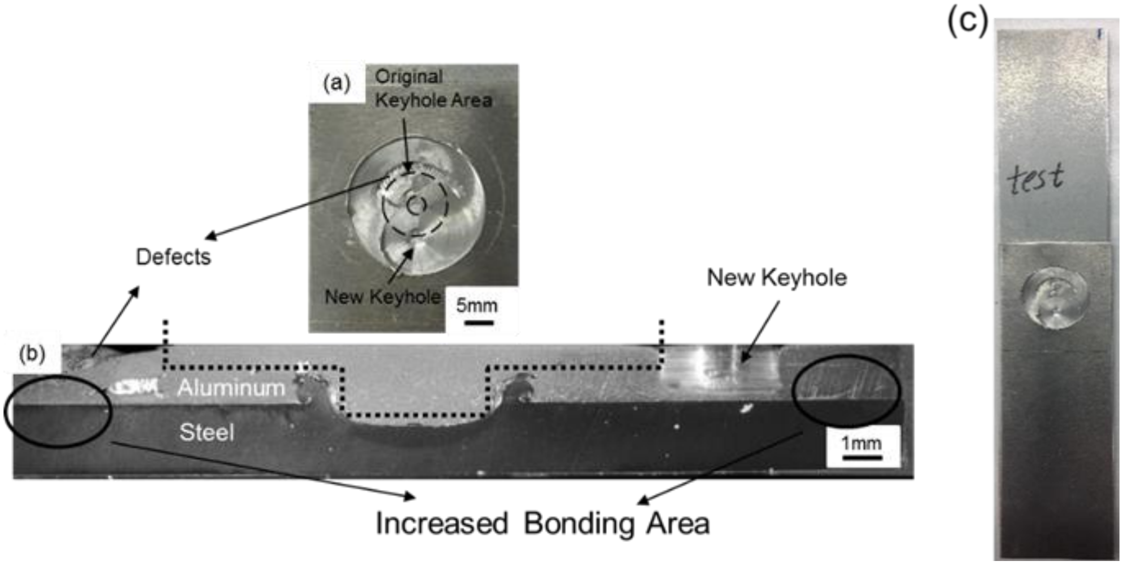

Figure 4-6. Macroscopic view of the keyhole refilled FSSW (a) Top view (b) Cross section view (c) Welded sample before the tensile test

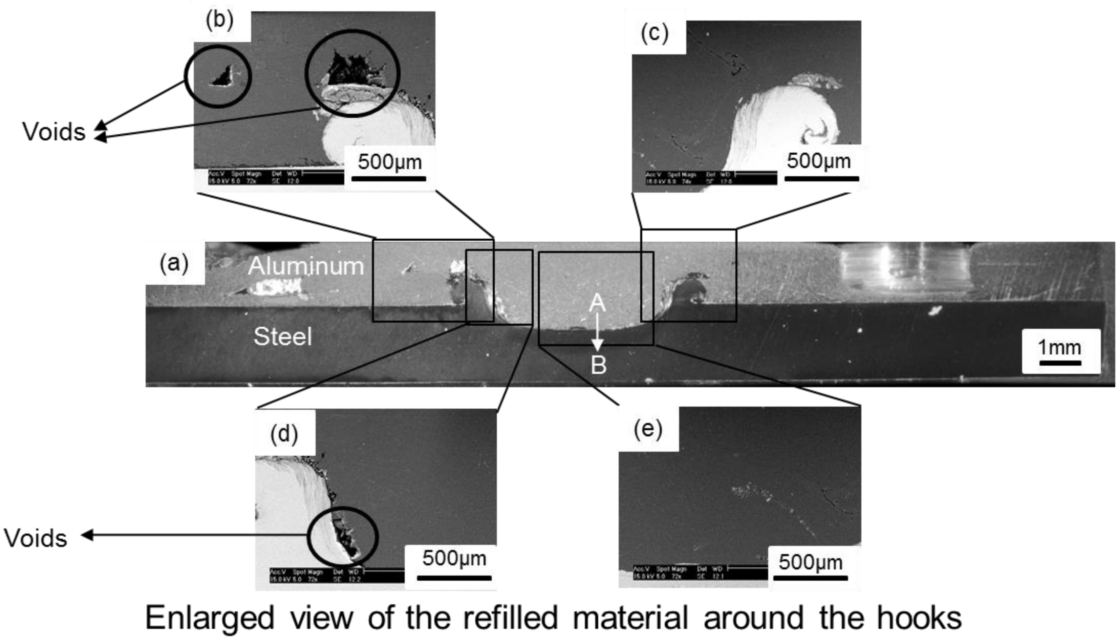

Figure 4-7. Enlarged view of material distribution around the original keyhole region

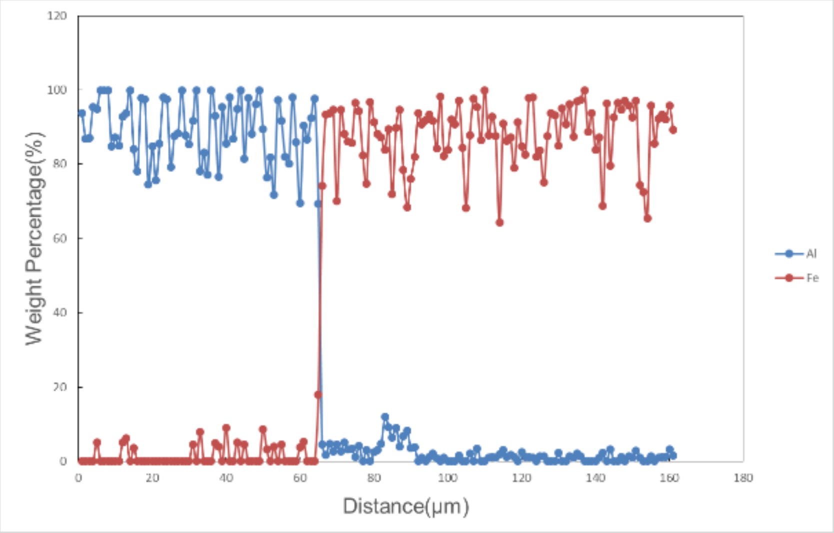

Figure 4-8. EDS analysis at the Al/Fe interface along line A-B in Figure 4-8 (a)

4.3.2 Metallographic Analysis

To further analyze the material flow of the steel during the welding process, the grain structures of the hook around the welding nugget are shown in Figure 4-9. It can be observed in Figure 4-9 (A) that the material flows along the path of the hook generation. To better understand the microstructure of this part, magnified views of area B and area C in Figure 4-9 (A) are provided in Figure 4-9 (B) and Figure 4-9 (C). The observed results show that the hook be classified into three layers according to the positions and different morphologies of grain structures. They are defined as the chip layer, the elongation layer and the recrystallization layer. The chip layer is located on the outside of the bottom region of the hook, where the grains have a similar size and shape as those of the original material. It indicates that this layer only experiences a small amount of plastic deformation and relatively low temperature. In the elongation layer, elongated columnar grains can be observed. These long thin grains are associated with the plastic flow of the steel, which is extruded upward due to the downward motion of the tool. In the recrystallization layer, fine and undistorted small grains can be observed. This layer is located on the inner side of the hook, which directly contacts the tool during the plunge stage. Principles for the formation of these three layers can be described as the followings: During the plunge stage of the regular FSSW step, materials adjacent to the tool pin are squeezed out to flow in radial and upward directions. The portion of the materials that directly surrounds the tool is subjected to the largest amount of plastic deformation. Besides, the temperature is high in this region due to the direct frictional heat generated between the tool and the workpiece as well as the heat from plastic deformation of the materials. When the temperature reaches a certain level, the high energy state of the grains under severe plastic deformation is released through recrystallization. Fine recrystallized grains therefore formed in this layer. This recrystallization layer is similar to the stirring zone of the friction stir welds. For the materials located further away from the tool, the temperature is relatively lower and the strain of plastic deformation is smaller, which are insufficient to induce recrystallization. The deformed grains remained in the elongated morphology after the welding process. Accordingly the elongation layer is formed, which is similar to the heat affected zone of friction stir welds. For the materials located further away from the tool, their movement is basically due to the plastic flow of the adjacent materials. The deforming effect of the tool is minimal in this area. The material flow is relatively rigid and involves little amount of plastic deformation. Accordingly, the grain structure remains similar to that of the unaffected base material, which forms the chip layer. Comparing the grain structures between region B and region C, it can be noticed that the fraction of the recrystallization layer in region B is smaller than that in region C. The extruded steel in region B is formed at the earlier stage of the welding process, where the temperature is relatively lower compared with that in the later stage of the plunge step, which corresponds to region C. As a result, less amount of recrystallization occurs and the layer is thinner in region B. Region D is located on the top surface of the original steel sheet and adjacent to the curling root of the hook structure. A magnified view of this area is provided in Figure 4-9 (D). It can be observed that at the connection area between the base material and the hook, the grain is compressed and distorted on the right side of Figure 4-9(D), which is a result from deformation force from the welding tool. While on the left side of Figure 4-9(D), a much uniform grain size can be found. The difference between the orientation of the grains also indicates a severe plastic deformation of the hook.

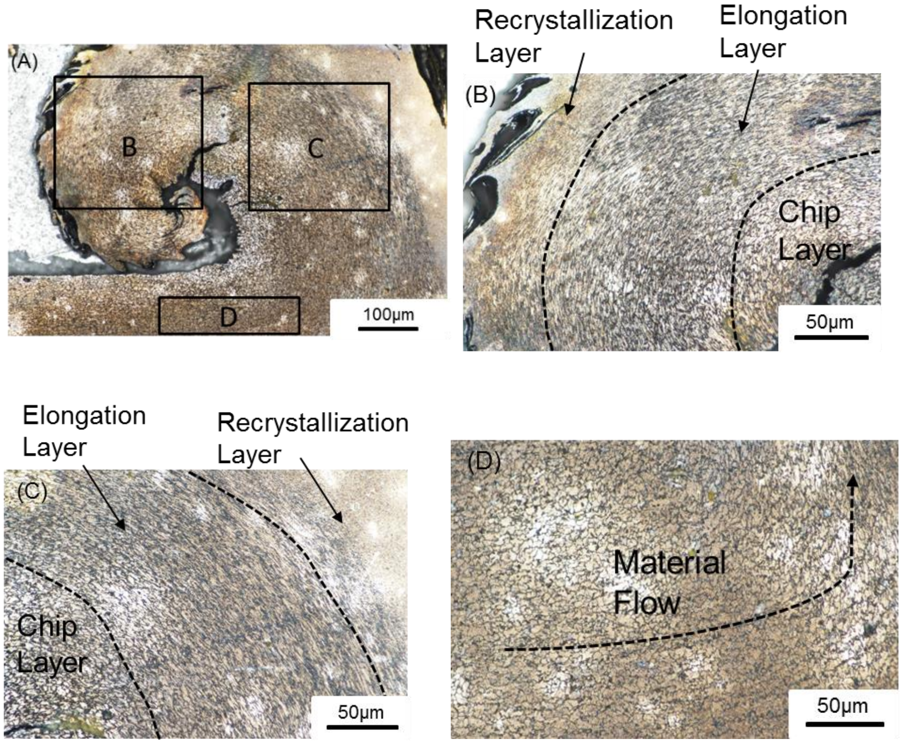

Figure 4-9. Cross section view of etched specimen: (A) Overall view of the hook on the left side (B) Enlarged view of region B (C) Enlarged view of region C (D) Enlarged view of region D

4.3.3 Joint Lap Shear Force

After the tensile test, the force-displacement curves of the conventional FSSW and keyhole refilled FSSW joints are shown in Figure 4-10. The test results reveal that the keyhole refilled

FSSW process can achieve both a higher maximum shear force and larger fracture elongation compared with the conventional FSSW process. A detailed comparison of the maximum lap shear force is shown in Figure 4-11 (a). The shear force value for the refilled joint is 6.91 ± 0.27KN while that for the regular joint is 4.42 ± 0.93KN, which shows an increase of 56.33% with the newly developed keyhole refilled FSSW process. Furthermore, the smaller variation of the joint strength indicates improved process reliability. Table 4-4 compares the lap shear force of the joints between aluminum alloy and steel obtained from different variants of FSSW process in literature. It can be observed that the joint strength achieved in this study is competitive when compared with the reported values from most of the literature. Even though the materials and method applied in this study are not exactly the same as what is reported in the literature, the data can also provide some insights about the achieved joint strength.

This enhanced joint strength can be attributed to the multiple bonding mechanisms introduced in this process. The first one is the original keyhole that has been refilled. In conventional FSSW joints, two fracture modes are generally observed during lap shear tests, including shear fracture and tensile/shear fracture [25]. Both of these occur near the keyhole region. Since the keyhole is refilled in this study, fracture near this area can be restrained. The second reason for the improvement of joint strength is the increase of the bonding area between the aluminum and steel sheet as the welding tool travels along the circular path surrounding the original keyhole, which is also illustrated from previous section. In addition to the increase of joint strength, Figure 4-10 shows the force displacement curve of the keyhole refilled FSSW joint has a significantly longer plastic deformation period before the failure occurs, which indicates a ductile fracture behavior and it is more desirable for engineering applications.

On the other hand, the curve corresponding to the conventional FSSW joint immediately decreases to zero after the force reaches the maximum value. The horizontal distance between the start of the test and failure of the joint is small. This indicates a brittle fracture, which is also shown in the SEM images from our previous studies on FSSW of Aluminum to TRIP steel [135]. In this study, the elongation of the joint is defined at the position of the maximum lap shear force. As shown in Figure 4-11 (b), the keyhole refilled FSSW process can significantly increase the joint elongation from 0.32 ± 0.04mm to 0.58 ± 0.03mm.

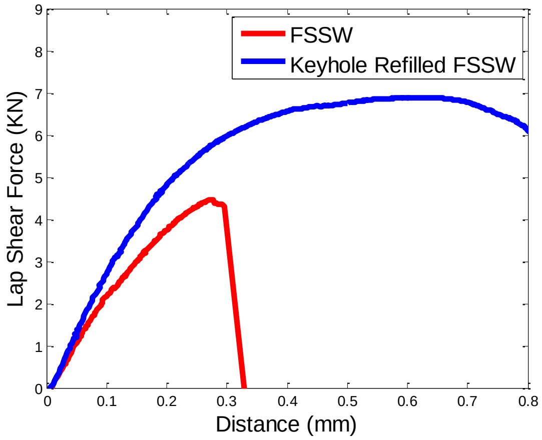

Figure 4-10. Force displacement curve with/without refilled keyhole during the lap shear test

Table 4-3. Comparisons of the lap shear force for Al/Fe FSSW

Joint Method	Base Material (Thickness)	Maximum Lap Shear Force (kN)
FSSW [136]	Aluminum 6000 series alloy and coated steel (1.3mm, 0.8mm)	3.1
FSSW [86]	Al 6016 and IF-steel (1.2mm, 2mm)	4.5
FSSW [137]	Aluminum alloy 6111 and low carbon steel (1.15mm, 1.2mm)	3.6
FSSW [135]	Aluminum 6061 and TRIP 780 steel (1.5mm)	4.0
Refilled FSSW [134]	Superlite 200ST aluminum and ST06 Z galvanized steel (1.5mm, 1.2mm)	4.5
Abrasion circle FSSW [138]	Aluminum alloy 6111-T4 and steel DC04 (1mm, 1mm)	3.5
FSSW by scroll grooved tool without probe [139]	6061-T6 and low carbon steel (2mm, 2mm)	4.9
Flat FSSW [140]	Aluminum alloy 6061-T6 and mild steel (1mm, 1mm)	3.6

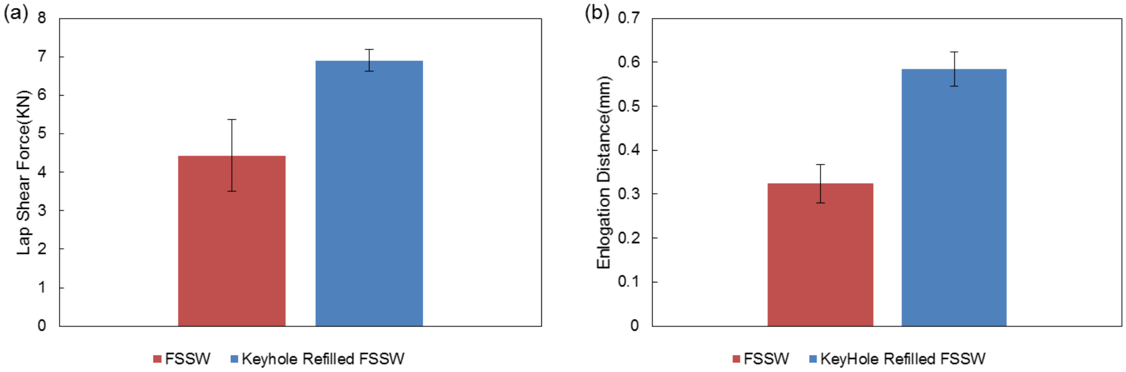

Figure 4-11. Comparison of (a) Lap shear force and (b) Elongation distance with/without the refilled keyhole

4.3.4 Pure Circular Path Welding

As described in the previous session, the keyhole refilled FSSW process consists of two independent steps: the conventional FSSW step and the keyhole refilling step. The tensile results show that the additional refilling step significantly improves the joint mechanical behavior. To separately evaluate the contributions of the refilling step to the final joint performance, a pure circular path welding is performed under the same set of process parameters as the second step, including the plunge depth, position and diameter of the circular tool path, tool rotating speed and traveling speed. Figure 4-12 shows the top view of the joint obtained from the pure circular path welding. Since the diameter of the circular tool path is smaller than the tool diameter, the center of the weld is subjected to the overlapping action of the tool shoulder. Weld flash is observed both along the outer periphery of the welding area and at the final position of the tool shoulder, which is composed of aluminum that is squeezed out by the FSSW tool during the process. No cracks and defects can be seen on the surface of the welding. However, a small keyhole is left after the final retraction of the tool from the aluminum sheet. Figure 4-13 shows the force-displacement curves of the conventional FSSW joint, the pure circular path joint and the keyhole refilled FSSW joint during lap shear tensile tests. It can be observed that both of the lap shear force and ductility from the pure circular path welding process are the lowest among the three. In the meantime, it can be noticed that both the pure circle path welding and conventional FSSW show a brittle fracture behavior, which also indicates a weak bonding between the steel and aluminum. The maximum lap shear force and elongation distance obtained from the lap shear tests for these three conditions are further compared in Figure 4-14. The lap shear force of the pure circular path weld is 3.3 ± 0.37kN and the joint elongation distance is 0.16 ± 0.01mm. From all of the data obtained through the experiment, it indicates that the pure circle path welding is not a desirable welding method for joining aluminum to steel and the second step of the keyhole refilled FSSW process itself is hardly a determining factor for the final joint performance. The conclusion from the discussion above can be drawn as the following: the significant improvement of joint quality between the steel and aluminum from the keyhole refilled FSSW process relies on not only the refilled keyhole and the increased bonding area from the circular path of the tool, but also the hook structure generated from the conventional FSSW process in the first step. From the first welding step, when the welding tool plunges into the steel sheet, the steel is extruded and inserted into the aluminum matrix, which forms the hook structure and produces a strong mechanical bonding. Based on this hook structure, the circular path welding in the second step then further enhances the joint mechanical behavior by refilling the keyhole. Besides, the bonding forms between the steel and aluminum through the purely circular path welding, which indicates that the aluminum and steel can be joined together even without the tool pin penetrating into the steel on the bottom.

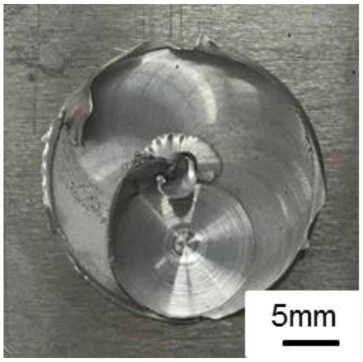

Figure 4-12. Top view of the joint geometry from the pure circular path welding

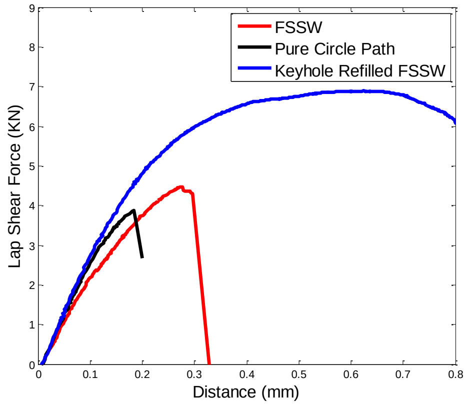

Figure 4-13. Comparison of force-displacement curves with different welding processes

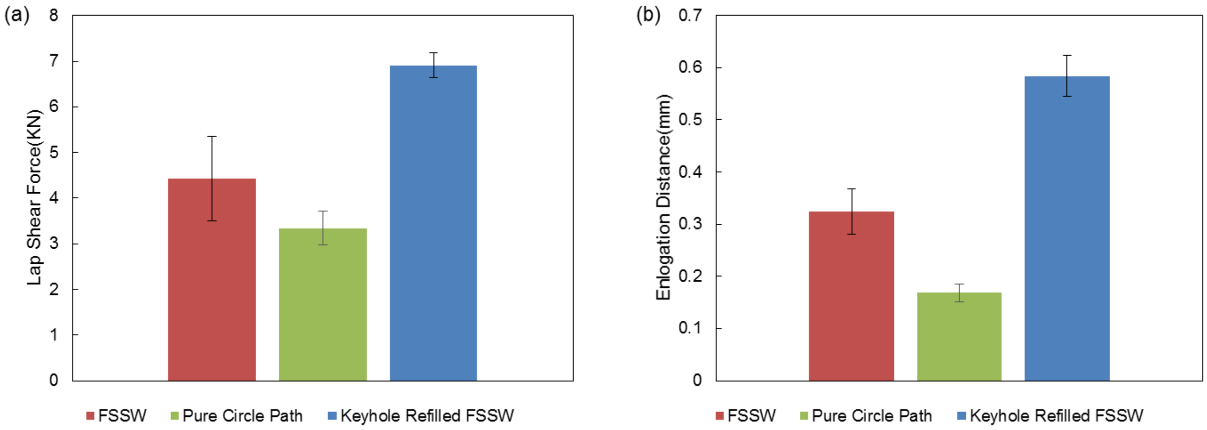

Figure 4-14. Comparisons of (a) Lap shear force and (b) Elongation distance with different welding processes

4.3.5 Joint Failure Mode

Failure modes for the conventional FSSW, pure circular path welding and keyhole refilled FSSW joints are compared in Figure 4-15, which shows the bottom surface of the aluminum sheet and the top surface of the steel sheet of each weld after lap shear tensile tests. For the conventional FSSW joint in Figure 4-15(a), the bonding between steel and aluminum can be noticed to primarily rely on the hook structure, which is also observed in our previous studies in Chapter 2 [135]. A small extruded hook remains on the top surface of steel after the fracture of the joint. The bonding at steel and aluminum interface outside of this hook structure is insignificant. Regarding the weld from the pure circular path as shown in Figure 4-15(b), only a small quantity of aluminum sticks on the top surface of steel, which indicates insufficient bonding. This is because the plunge depth in the circular path welding or the second step of the keyhole refilled FSSW is small and the pin induces little plastic deformation on steel. During the process, only aluminum alloy is compressed and stirred. The bonding is generated at the interface between aluminum and steel basically from the compression force, which is relatively weak and no strong mechanical constraints are generated. It can also be an explanation for the low joint strength and brittle failure of the pure circle welding.

Different from the fracture behaviors of the conventional FSSW and pure circular path welds, the keyhole refilled FSSW process is capable of achieving a much stronger bonding between the steel and aluminum, as shown in Figure 4-15(c). During lap shear tests, the cracks propagate along the periphery located outside of the original keyhole area. After the joint failed, a large amount of aluminum can be observed to stick on the fractured surface of the steel, which indicates a strong bonding between the steel and aluminum after the welding process. The diameter of this sticking aluminum is around 1.6mm. The fracture mechanism of the keyhole refilled FSSW joint during lap shear tensile tests is illustrated in Figure 4-16. From Figure 4-16 (a), it can be noticed that the force applied on the aluminum points to right while the force on the steel is on the left. As a result of the increase in the applied force, the cracks initiate at the position of the surface defects, which has been described in the previous session and is labeled as region A in Figure 4-16(a) and Figure 4-16(b). After the externally applied force and the pulling distance of the joint further increases, the cracks propagate along the outer periphery of the original keyhole area and lead to a final failure at region B, which is located at the boundary of the new small keyhole.

The failure of the keyhole refilled FSSW joint is closely related to the welding defects as well as the new keyhole. In order to improve the joint quality of the keyhole refilled FSSW process, the improvement of these two features can be a possible direction. The fractographical analysis is performed at position A in Figure 4-16(b) and the results are shown in Figure 4-17. Features of dimples and microvoids can be observed on the fractured surface. This further shows the joint failed in a ductile mode and is consistent with the observations from the force-displacement curve. This newly developed keyhole refilled FSSW process can transform the relatively brittle aluminum to steel FSSW joint into a ductile behavior, which can be anticipated to further benefit the joint fatigue life and is highly desirable in various applications.

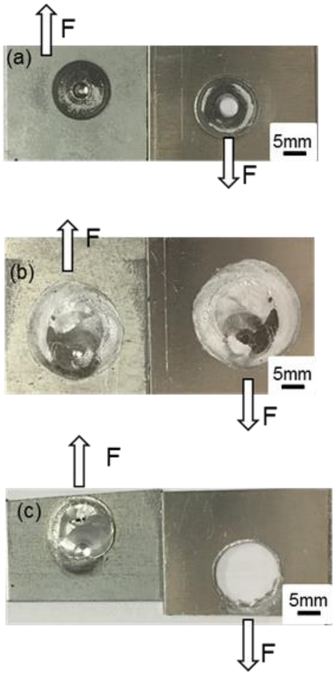

Figure 4-15. Failure modes for (a) FSSW (b) Pure circle path welding (c) Keyhole refilled FSSW

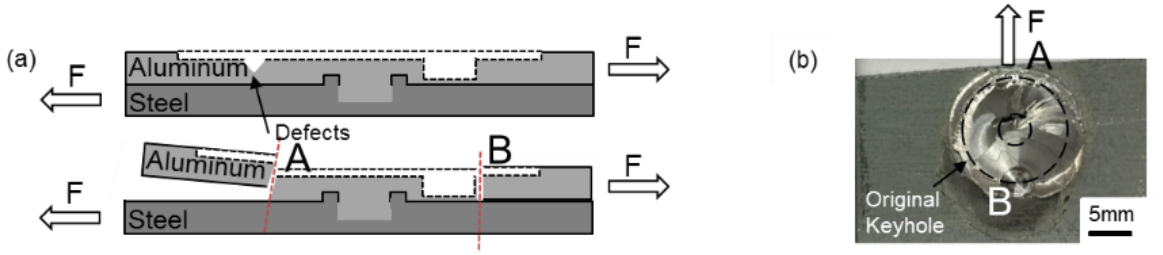

Figure 4-16. (a) Schematic illustration of the failure (b) Top view of the failure on steel side

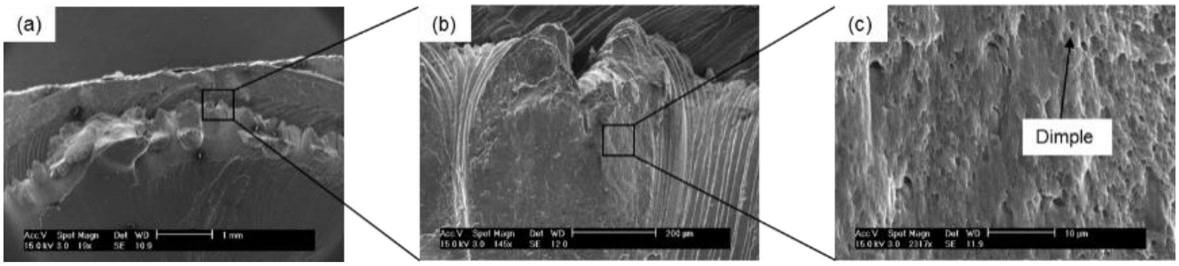

Figure 4-17. Scanning Electron Microscopy (SEM) images on the fracture surface

4.4 Conclusions

In this study, a keyhole refilled friction stir spot welding has been developed and applied to join aluminum alloy 6061 to TRIP 780 steel. The process contains two steps. In the first step, regular FSSW is performed. The keyhole is refilled in the second step by traveling the tool along a predefined circular path. Joint performance is improved in the aspects of both joint strength and elongation when compared with conventional FSSW welds. Following conclusions can be made through this study:

1. The developed keyhole refilled FSSW process can effectively refill the original keyhole with aluminum. Cracks are absent at the contact surface between steel and aluminum. However, some defects exist at the top surface of the weld, which is due to the lack of refilling material and should be removed in future improvements.

2. The lap shear tests show that the keyhole refilled FSSW increases the joint shear force by 56.33% compared with conventional FSSW joint. The joint elongation is improved by 81.25% and the refilled FSSW joint fails in a ductile mode despite the existence of some surface defects.

3. In the steel hook structure, three layers can be identified based on different morphologies of the grain structure, including the chip layer, the elongation layer and the recrystallization layer. It is found that a larger recrystallization layer exists on the final stage of the welding, which is due to the large deformation of the crystal structure and great amount of heat generation during this period. It is also noticed that the formation of different layers is the results of various combinations of the thermal and stress contribution during the welding process.

4. Pure circular path welding was performed to evaluate the contribution of the refilling step to the final joint strength. The corresponding joint shear force and elongation show the lowest value, which indicates the second step itself of the keyhole refilled FSSW process is not the dominant factor in determining the joint strength.

5. Three bonding mechanisms contribute to the improved performance of the keyhole refilled FSSW joints. First, the original keyhole is refilled, which restrains the initiation of cracks in this region. Second, the bonding area between steel and aluminum is increased as the welding tool travels along a circular path. Finally, the hook structure generated in the regular FSSW step is indispensable for a strong joint.

CHAPTER 5
FRICTION STIR RESISTANCE SPOT WELDING OF ALUMINUM ALLOY TO ADVANCED HIGH STRENGTH STEEL

5.1 Literature Review

From the previous chapters, the friction stir spot welding is shown to be capable of joining dissimilar materials without any consumptions and a reasonable high strength can be achieved through the keyhole refilled welding process. However, since materials are undergoing severe plastic deformation during the solid state welding process in FSSW, it brings several inherent disadvantages, including a large axial plunge force, a relatively long welding time and insufficient material flow. To overcome these difficulties and enhance the weld performance, some novel improvements have been employed in the friction stir welding (FSW) process. Sun et al. [141] applied laser as a preheating source to improve the friction stir welding of S45C steel plates. In their study, different positions of the laser focal points were tested, and the welding speed could reach up to 800mm/min when the laser beam was focused at the joint line. In addition, they indicated that the friction heat generated between the tool and the workpiece was reduced when preheating was applied on the advancing side. Chang et al. [142] studied the laser-assisted friction stir welding between aluminum alloy 6061-T6 to Mg alloy AZ31. To get a strong welding between the dissimilar materials, they inserted a Ni foil between the faying surfaces, and the resulted weld strength was 66% of the Mg base metal tensile strength. Merklein et al. [143] applied laser-assisted friction stir welding to weld deep drawing steel DC04 and the aluminum alloy AA6016-T4. With the application of laser, the welding feed speed increased up to 2000 mm/min and the welded tensile strength reached 80% of the aluminum base material. They also mentioned that there were no intermetallic phases generated even when applying the laser during the welding process. Several similar researches [57, 144-150] have been published to investigate the advances of the laser-assisted FSW.

Besides the laser-assisted FSW, ultrasonic assisted FSW was developed and studied to enlarge the welding process window and enhance the material flow. Park et al. [151] did ultrasonic assisted friction stir welding of aluminum alloys. The welding force was reduced and the mechanical properties of the welded part were improved, including both the elongation and yield strength. Besides, the chance of forming a welding defect was decreased. Ahmadnia et al. [152] applied a vertical high-frequency vibration on the friction stir tool to weld aluminum 6061. Effects of four major process parameters on the welding quality were studied, including ultrasonic power, tool rotating speed, traverse speed and axial force. The vibration power was shown to be the most dominant factor in determining the mechanical properties of the weld.

In addition to laser assisted and ultrasonic assisted process, researches were performed to investigate effects of the electrical current on friction stir welding process. Luo et al. [153] did electrically assisted friction stir welding of similar materials, including Mg alloy AZ31B, Al alloy 7075 and steel Q235B. They found that the resistant heat produced by the electrical current refined the grain size and increased the hardness of the welding nugget. Liu et al. [61] performed electrically assisted friction stir welding of aluminum alloy 6061 to TRIP 780 steel. Two electrodes were placed at the sides and moved along with the welding tool during the welding process. From their study, the axial welding force was reduced.

Since a high electrical current density is required to pass through the welding zone for the electrically assisted FSSW process, this creates challenges for the design of the experimental system. The experimental configuration of Luo et al. [153] is shown in Figure 5-1. Regarding the electrode configuration, one electrode was connected to the welding tool through a brush and the other electrode was connected to the conductive brick attached to the backing plate. Mica sheets were used to insulate the workpiece from the backing plate. The designed current path allowed the current to flow through the workpiece in front of welding, which pre-heated the workpiece and reduced the welding force. The magnitude of electrical current varied from 0A to 150A, which was a relatively small value when compared to that in the resistance spot welding process.

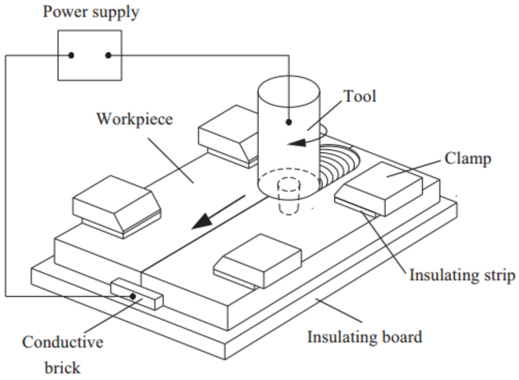

Figure 5-1 Schematic illustration of electrically assisted FSW by Luo et al. [153]

Santos et al. [154] designed a dedicated tool and fixture for the electrically assisted friction stir welding of aluminum alloy AA6082-T6. A schematic illustration of their experimental setup is shown in Figure 5-2. A copper core was inserted in the center of the welding tool and connected to one electrode. The end of the other electrode was connected to a copper that was embedded in the backing plate beneath the workpiece. The applied current flowed along the copper in the welding tool and then passed through the workpiece to the backing plate. The designed current path maximized the current density and Joule heating effect on the welded material, and the corresponding maximum current density reached 800A. However, one of the possible limitations of this experimental setup is that it could not support a large plunge force, since the hardness of the copper on the backing plate and tool center was insufficient.

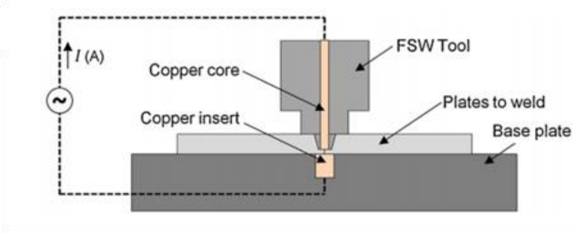

Figure 5-2. Schematic illustration of electrically assisted FSW by Santos et al.[154]

Liu et al. [61] also performed electrically assisted friction stir welding, which mainly focused on the dissimilar materials joining. Their experimental setup is shown in Figure 5-3. The two electrodes were placed on the top surface of the welding materials and traveled together with the FSW tool during the welding process. In this configuration, the applied current flowed through the two base materials and the FSW tool was only passively involved in the circuit. This system works effectively for butt joint configuration of thin sheets. However, for a spot joint, the current density is insufficient as discussed in the following session.

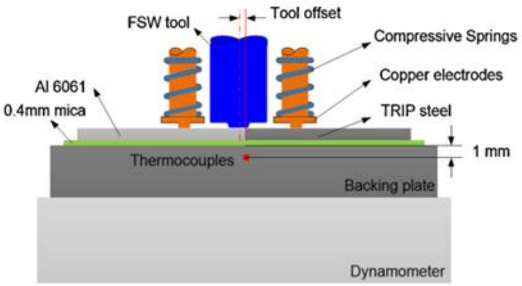

Figure 5-3. Schematic illustration of electrically assisted FSW by Liu et al. [61]

In this research, an improved electrically assisted experimental system is developed for spot joining configuration based on our previous studies. During conventional resistance spot welding (RSW) process, the applied current is usually in the range of 10^3 Amps [155]. As a comparison, the current applied in the hybrid friction stir resistance spot welding in this study is only in the order of 10^2 Amps. This relatively low electrical current input aims to avoid bulk melting and to suppress formation of large amount of IMCs.

5.2 Experimental Configuration

5.2.1 Experimental Setup Details

The base materials applied in this experiments are Al alloy 6061-T6 and TRIP 780 steel. The thickness of both materials is 1.5mm, and the aluminum sheet is placed on top of the steel as the welding configuration. During the experiment, the tool axis was aligned with the center of the overlapped area. To measure the axial plunge force, a Kistler dynamometer (type 9255ASP) was mounted below the workpiece. The measurement range is -20kN to 20kN in the x and y directions and -10kN to 40kN in the z-direction. Obtained welds were sectioned in the center and then mounted, ground and polished for microstructure analysis. Optical microscope and scanning electron microscope (SEM) were applied to characterize the joint cross section. In the meantime, the energy dispersive X-ray spectroscopy (EDS) was employed to determine the elemental distributions at the Al/Fe interface. The welding tool used in this study is made of tungsten carbide with 10% cobalt and the hardness is 91.8HRA. The tool has the feature of a non-threaded cylindrical pin and a flat shoulder. Other specific dimensions are shown in Figure 5-4. An electrical power supply that can provide both direct current and pulsed current with different frequencies is employed in this experiment. The magnitude of the current can vary from 0 to 1000 amps and the pulse on/off times can be set independently anywhere between 0.001 to 6.5 s. This power supply can also be programmed to produce customized waveform profiles. Different forms of current were applied in the experiment for understanding the possibly different effects of the DC and pulses on the joint performance. In this study, the plunge depth is defined as the distance between the end surface of the tool pin and top surface of the original aluminum sheet. Zero plunge depth is where the pin tip starts to touch the aluminum top surface, which is also illustrated in Figure 5-4.

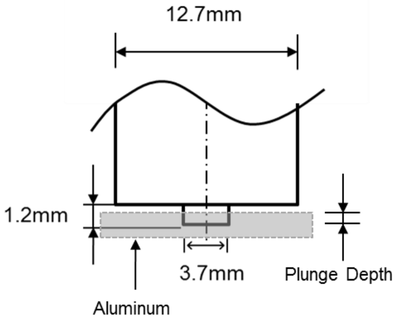

Figure 5-4. Illustration of FSSW tool dimension and the definition of the plunge depth

5.2.2 Initial Experimental Setup Design

The initial investigation of electrically assisted FSSW is made with an experimental setup similar to that of Liu et al. [61]. The overall experimental configuration is shown in Figure 5-5. Two electrodes are placed on the two sides of the welding tool, as the current flows through the electrodes, the applied current will also go through the stirring region. To insulate the workpiece from the backing plate, the mica film is inserted below welding materials. Two electrode configurations were investigated, as shown in Figure 5-6 from a top view. On the left side condition, both the electrodes are placed on the aluminum top surface. On the right side, one of the electrodes on aluminum is moved to the steel surface.

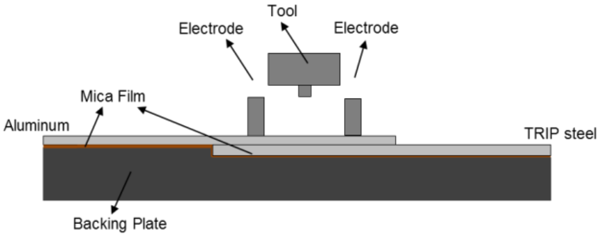

Figure 5-5. Illustration of the initial experimental setup for the electrically assisted FSSW

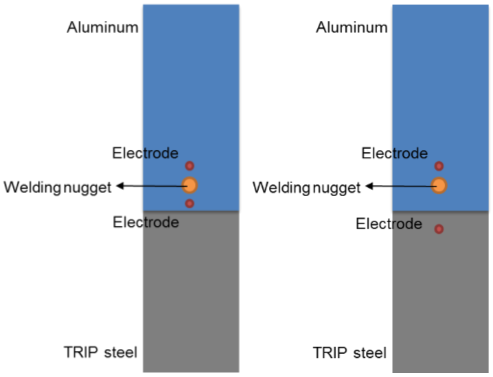

Figure 5-6. Schematic illustration of different electrode positions for electrically assisted FSSW

Based on the two configurations, axial welding force is measured and compared between conventional FSSW and electrically assisted conditions. When both the electrodes are placed on the top surface of the aluminum, the result shows negligible change in the peak force. The possible explanation can be stated as the following: as the aluminum has a much larger electrical conductivity than steel, a large portion of the current flows through the aluminum other than the steel. In this way, the effect of the current is not significant to the steel, which results in a negligible force reduction. In the other configuration where one electrode is placed on the steel surface, the maximum plunge force decreases from 9.49±0.19 kN to 8.71±0.44 kN, which is also not a desirable result.

5.2.3 Experimental Setup Design Improvement

The initial experimental design did not provide a significant evidence of decreasing the plunge force during the welding process. The possible reason is that the current density flowing through the steel is insufficient. To understand the current density distribution with different electrode configurations, a numerical analysis is performed with the COMSOL Multiphysics program. The model is simplified, which only includes the base materials and the electrodes. Besides, the simulation is based on the initial status of the workpiece and the actual material deformation during FSSW process is not taken into consideration. The contact properties between steel and aluminum, workpiece materials and the electrodes are considered as a perfect contact. One of the electrodes is assigned as a constant current source with a current amplitude of 560A, and the other electrode is treated as ground. The bottom surface of the workpiece, which is in contact with the mica film in the experimental setup, is assumed as electrically insulated.

The calculated current density distributions for the initial experimental designs are shown in Figures 5-7(a) and (b). It can be observed that a high current density concentrates near the electrode region. Moreover, in both conditions the current density in the steel sheet is less than 10 A/mm^2. According to the works from Perkins et al. [156] in electrically assisted forging process of steel, a current density larger than 17.8 A/mm^2 can result in visible softening effects on the steel, as shown in Figure 5-8. Another research from Liu et al. [85] indicated that the electro-plastic effect can be observed when the current density is larger than 11.4 A/mm^2. Both of them indicate that the current density in the initial experimental design produces a trivial softening effect for steel during the welding process and therefore the reduction of axial force is insignificant.

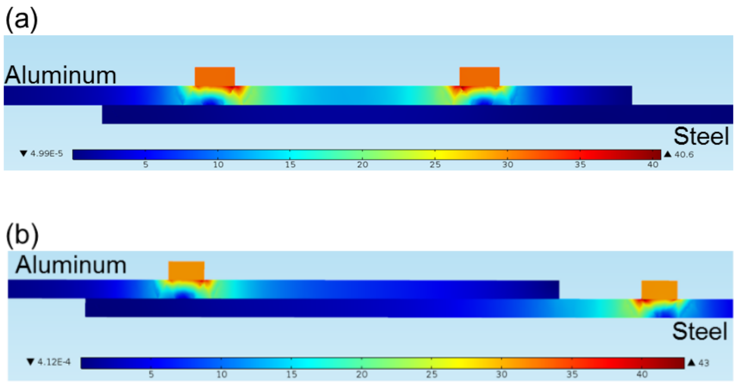

Figure 5-7. (a) Current density distribution when both electrodes are placed on the top aluminum side (b) Current density distribution when the electrodes are placed on different base materials

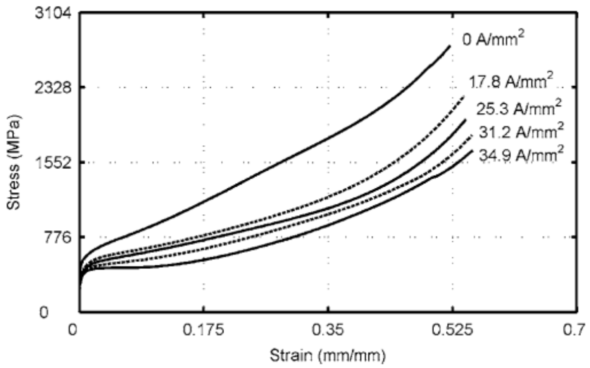

Figure 5-8. Stress-strain curve during electrically assisted forging process of steel [156]

To increase the current density in the steel, the experimental system is improved as shown in Figure 5-9(a). In this setup, instead of flowing between two electrodes on both sides of the welding tool, the electrical current is applied to an independent electrode with a ring geometry and the backing plate serves as the second electrode. The ring electrode is placed on the top surface of the aluminum sheet with the FSSW tool in the center. The inner diameter of this ring is slightly larger than the diameter of the welding tool shoulder, and the tool is only passively involved in the electrical circuit. During clamping, only the bottom side of the metal ring is in contact with the top surface of the aluminum, and it applies a compressive force for clamping the aluminum and steel sheet. On the top surface of the backing plate, a cylinder with the height of 0.1mm, diameter of 3.7mm protrudes out. The center of this cylinder is aligned with the tool axis. The rest region of the backing plate is covered with an insulating mica sheet, which is to guarantee that all the electrical current flows through this cylinder and therefore the current density can be maximized. Regarding the electrode connection, one electrode is connected to the metal ring, and the other is attached to the backing plate. The current path can be described as followings: the electrical current enters into the metal ring to the workpiece from one electrode. The current flows out from the workpiece to the cylinder protrusion on the backing plate, which is connected to the other electrode. The current flow path during the welding process is also illustrated in Figure 5-9(b).

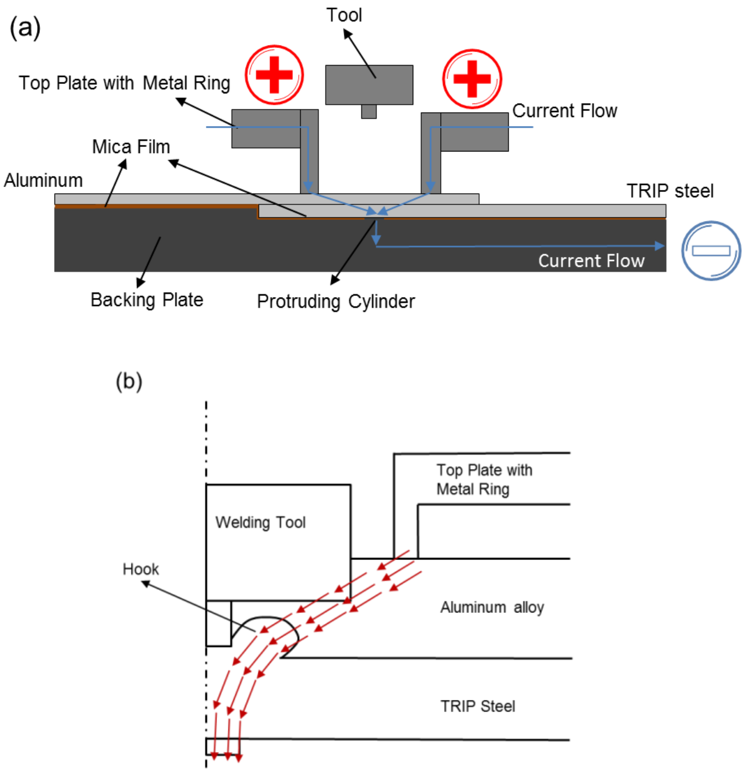

Figure 5-9. (a) Illustration of the experimental setup for electrically assisted FSSW (b) Schematic illustration of the current flow during the welding process

The current density distribution for the new fixture design is again analyzed using the COMSOL Multiphysics software, and the corresponding calculated result is shown in Figure 5-10. Under a DC input of 560A, the maximum current density reaches 73.5A/mm^2 at the bottom surface of the steel. The calculated current density should therefore be capable of ensuring the softening effect on the steel according to Perkins et al. [156] and Liu et al. [85]. All the following results and discussions are based on this experimental configuration. The actual setup and welded sample are shown in Figure 5-11. From Figure 5-11, the mica film is placed between the screws and the clamping ring, which is to ensure the current will not flow through the screws to the backing plate other than the metal ring. The top side view of the welded sample is also shown in Figure 5-11(b). Geometry and dimensions of the welding tool are previously shown in Figure 5-4.

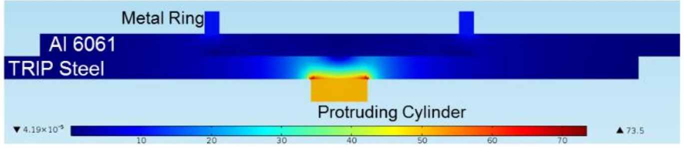

Figure 5-10. Simulation results for the current density distribution of the experimental setup

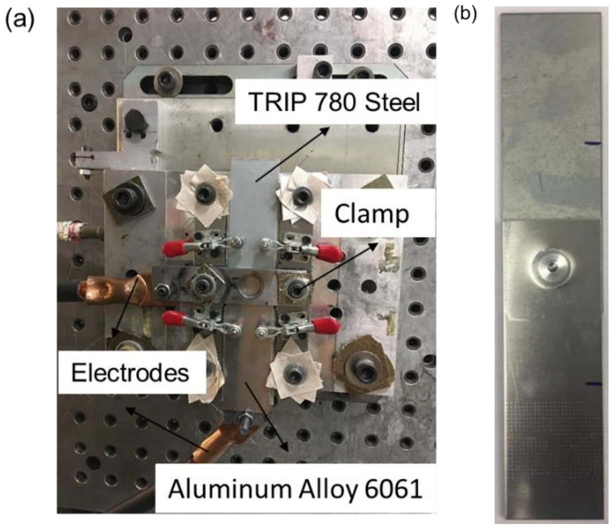

Figure 5-11. (a) Experimental setup for the electrically assisted friction stir spot welding (b) A typical welded sample

To investigate effects of the electrical pulses on the FSSW process, the magnitude of the pulse is selected at 900A with a turn-on time of 1ms and duty cycle of 50%. Preliminary experiments were performed where the electrical current was applied under conditions of different tool rotational and plunge speeds. The reduction of the welding force was shown to be more significant under lower rotational speed and faster plunge speed. The final process parameters for a detailed comparison between electrically assisted and conventional FSSW process are listed in Table 5-1. The current is turned on immediately as the tool starts to touch the aluminum top surface, and it is stopped at the end of the plunge stage before the dwell stage.

Table 5-1. Process parameters for the electrically assisted FSSW

Rotational speed (rpm)	Plunge speed (mm/min)	Plunge depth (mm)	Dwell time (s)
1000	30	1.9	3

5.3 Results and Discussion

5.3.1 Effect of Electrical Pulse on Axial Welding Force

Typical axial plunge force curves measured in conventional FSSW and electrical pulse assisted conditions are compared in Figure 5-12. The two force histories follow a similar trend. In the beginning of the plunge stage, the rotating pin starts to deform aluminum on the top surface and gradually moves into the workpiece. The plunge force increases due to the growing amount of deformation materials. As the pin travels deeper, the heat generated from both friction and plastic deformation in the workpiece softens aluminum to an overheated level, which makes it easier for the pin to plunge further into workpiece and the axial plunge force stops increasing.

Then as the tool shoulder surface begins to touch the squeezed out aluminum, plunge force increases again. As the rotating shoulder moves deeper into aluminum, the heat generated from friction and severe plastic deformation again reaches an overshoot level and the force stops increasing. Finally, the tool pin starts to deform the steel and the plunge force increases again. During the entire process, the axial plunge force with the application of electrical current is smaller than that in the conditions without current. To quantitively compare the force histories obtained from the two conditions, the mean absolute percentage difference is calculated from Equation (5-1). n is the total number of data points on the curve. A_t is the corresponding value when no current is applied and F_t is the value when pulses are applied. The mean absolute percentage difference between the electrically assisted and conventional condition is 12.84%. Repeated experiments were performed for statistical analysis. The maximum plunge force reaches 15.67±0.13 kN in conventional FSSW, while it decreases to 14.10±0.01 kN after the electrical pulses are employed. This indicates that the electrical current can effectively decrease the axial plunge force during the welding process.

$$M = \frac{100}{n}\sum_{t=1}^{n}\frac{|A_t - F_t|}{A_t} \qquad \text{Eq. 5-1}$$

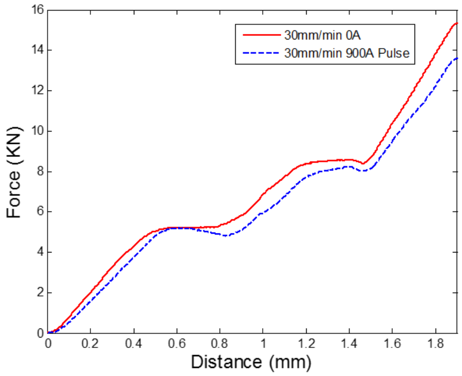

Figure 5-12. Comparison of the axial plunge force with and without the electrical current

5.3.2 Comparison Between the Effects of Electrical Pulse and Direct Current

There are two types of theories explaining the material softening induced by electrical current. One is the thermal softening due to the associated Joule heating. The other is the electro-plastic effect, which describes that the electrical current can directly reduce material deformation resistance without increasing the bulk temperature. Siopis et al. [157] applied electrical current during compression tests on the pure copper and the deformation force is reduced. The maximum temperature is 280ºC, which is well below the hot working temperature of pure copper. They also reported that a finer grain size could achieve a greater stress reduction from electrical current. Perkins et al. [156] applied current for forging various materials and a better formability could be achieved. The reduction of flow stress exceeds those achieved by purely increasing the temperature at the same level. They reported the moving electrons could directly transfer the energy to dislocations and increase the local stress and strain fields. In this study, to differentiate between thermal softening and electro-plastic effect and to understand the underlying mechanisms of the observed force reduction in electrically assisted FSSW process, a direct current (DC) with an equal amount of energy input as the pulsed condition in the previous session is applied. The amplitude of the corresponding equivalent DC is calculated based on the following equation:

$$I_{dc}^{2} \cdot t_{tot} = \int I^{2} dt \qquad \text{Eq. 5-2}$$

where I is the magnitude of the electrical pulses and I_{dc} is the magnitude of the equivalent DC. The total time duration t_{tot} is selected as the length of plunge stage. During experiments, the actual pulses are associated with a ramping up period and can hardly achieve an ideal rectangular shape. The corresponding recorded current is shown in Figure 5-13. Based on Equation (5-2), the equivalent I_{dc} is then calculated to be 560A.

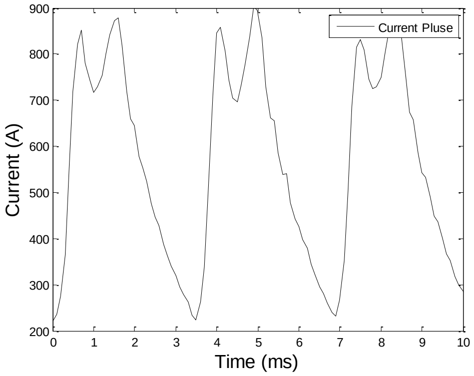

Figure 5-13. Recorded current pulse signal during the FSSW welding process

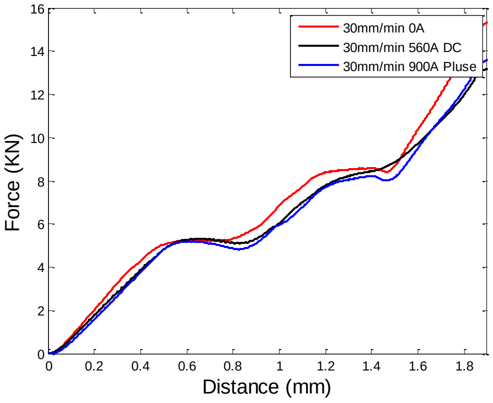

Figure 5-14. Comparison of axial plunge force with the 560A DC, 900A pulse and zero current condition

The equivalent DC is then applied during the FSSW process, and the corresponding axial welding force is compared with that from both zero current and pulse conditions in Figure 5-14. It can be noticed that the difference between the two curves is trivial. The mean absolute percentage difference between the two force histories is 7.42%, which is calculated based on Equation (5-1). The maximum plunge force for 560A DC is 13.47±0.05 kN while that for the pulse condition is 14.10±0.01 kN. This indicated that with the same amount of energy input, the force reduction is about the same. In other words, thermal effect dominates and there is no strong evidence to prove the electro-plastic effect when the pulses are applied during the FSSW process. One of the possible explanations is that the material is deformed under a condition of high pressure as well as high temperature, which impairs the electro-plastic effect on the steel.

5.3.3 Effect of Current on Material Flow

An overview of a typical joint cross section is provided in Figure 5-15(a). The marked area in rectangle is enlarged in Figure 5-15 (b), where a groove line can be observed in the thermo-mechanically affected zone (TMAZ). This line is located at a certain distance away from the tool shoulder. To identify the element composition of the groove line, an EDS analysis is performed along a straight line from point A to point B, as indicated in Figure 5-15(c). The analysis results are shown in Figure 5-16. The number of counts for Zn within the region of interest increases when the test passes through the groove line, which shows the groove line is composed of Zn and it comes from the coating of the TRIP steel sheet. During the plunge stage at the interface between the bottom surface of aluminum and the top surface of steel, the Zn coating on the surface of the steel is likely to be bonded to the bottom surface of aluminum under the combined state of high pressure and temperature. The mixed Zn and aluminum then move together with each other during the welding process. In this perspective, Zn can be treated as a tracer for the material flow in the bottom region of the aluminum sheet.

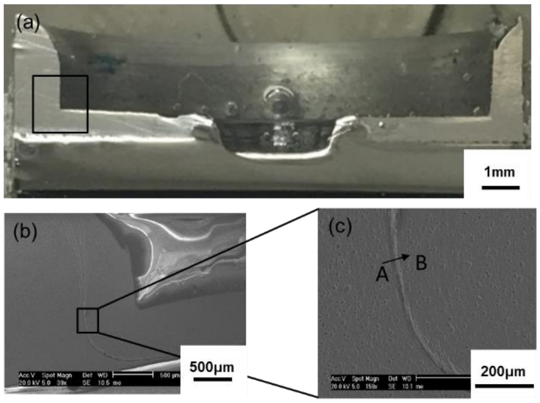

Figure 5-15. (a) General cross section view of the welding region (b) Enlarged cross section view of the sample (c) EDS line test from point A to B

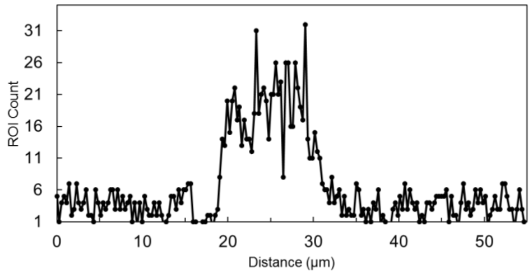

Figure 5-16. ROI counts for Zn through EDS line test

Figure 5-17 further compares the region of Figure 5-15 (b) between traditional FSSW process and electrically assisted conditions. In Figure 5-17 (a), the Zn line starts from the bottom of the aluminum sheet and then extends upward. Regarding the aluminum flow during the welding process, the top region of aluminum is pushed outward as the welding tool plunges into the materials. As the flowing aluminum reaches the relatively cold area in the heat affected zone (HAZ), it moves upward due to the constraints of cold materials that have a higher deformation resistance. The material flow in the bottom region follows a similar pattern. For a qualitative description of the amount of material flow during the welding process, the distance L is measured from the outer boundary of the tool shoulder to the Zn line and it is also parallel to the original Al/Fe interface, as shown in Figure 5-17 (a). Comparing Figure 5-17 (a) with Figure 5-17 (b), a larger distance L is observed when there is a 560A DC applied during the welding process, which has a value of 0.63±0.04 mm and that without the current is 0.41±0.03 mm. The larger value of L indicates a better material flow in the electrically assisted conditions.

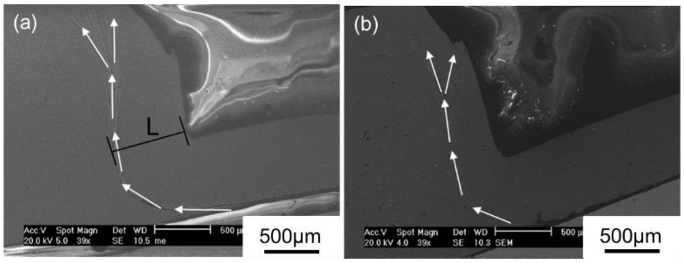

Figure 5-17. Zn flow pattern during the welding process (a) with direct current (b) without current

5.3.4 Effect of Current on Welding Strength

The joint shear strength of the weld samples obtained from conventional, direct current assisted and pulse current assisted conditions are compared in Figure 5-18. The application of direct current increases the joint strength by around 43% while the pulses increase that by 28%. This improvement can be contributed from different interaction mechanisms between aluminum and steel during the conventional and electrically assisted welding processes.

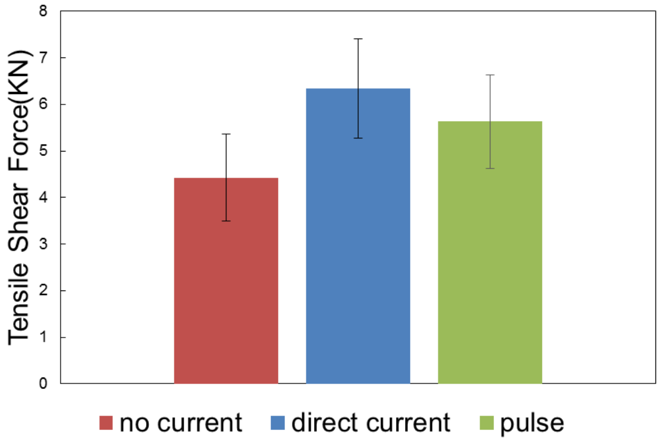

Figure 5-18. Comparison of shear strengths under the conditions of no current, 560A DC and pulse

Figure 5-19 schematically illustrates the hook formation and material interactions at the boundary of the hook during the welding process. As the welding tool moves downward, the tool shoulder compresses the aluminum matrix and the steel is extruded upward by the tool pin. As the tool reaches a deeper position, the aluminum is pushed towards the outside and more amount of steel is extruded to generate a larger hook. The new layer of extruded steel flows along the edge of the existing hook. In the meantime, a portion of the aluminum is embedded below this new steel layer. The embedded aluminum reacts with the steel under certain temperature and pressure state, which results in the formation of IMC. As the tool plunge depth increases and more layers of steel are extruded, a periodic vortex morphology can be observed at the top side of the hook. Figure 5-20 shows the interaction layer between steel and aluminum of the conventional FSSW joints.

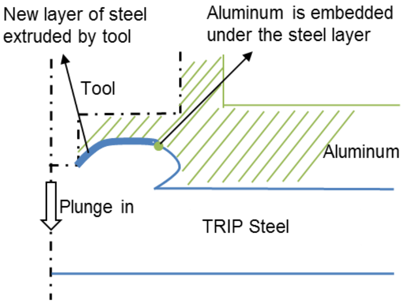

Figure 5-19. Illustration of the material interaction between steel and aluminum

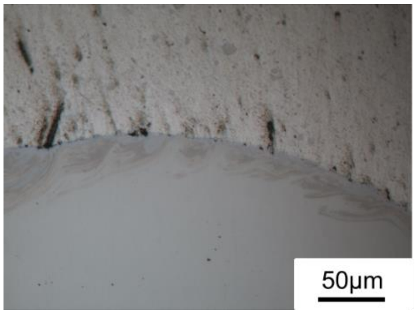

Figure 5-20. Vortex shape generated at the top of the hook (no current)

As the plunge depth further increases, a larger hook is formed and less amount of aluminum is allowed between tool shoulder and hook based on the geometrical constraints. It can be illustrated in Figure 5-21 (a), where the inside area is labeled as 1 and outside is labeled as 2. On the other hand, at this specific tool position, it is difficult for the aluminum surrounding the tool pin to flow outside. Accordingly, this amount of aluminum is compressed downward into the hook. At the same time, the extruded steel is pushed upward by the tool pin, which leads to a severe mixture between steel and aluminum at the inside region of the hook, as shown in Figure 5-21 (b). The mechanical mixing of the base materials also generates a large deformation resistance.

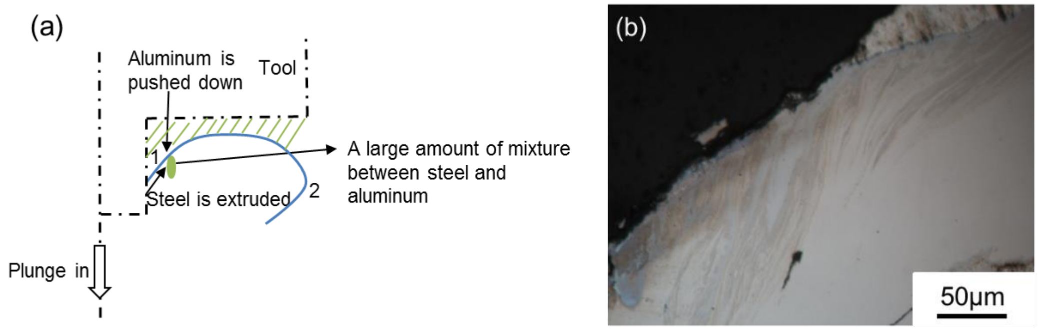

Figure 5-21. (a) Illustration of the mixing pattern between aluminum and steel at a deeper plunge depth (b) Cross section view of the inside of the hook (no current)

For the standard FSSW, the material interaction between aluminum and steel is dominated by the bulk material flow, which is driven by the motion of the welding tool. The application of electrical current provides extra heat energy and enhances the atomic diffusion rate, which is referred as the electro-migration effect. According to Chen et al. [158, 159], the flux of atoms is driven by both the chemical potential and the electric field, which can be expressed as:

$$J_i = \frac{-D_i N_i}{kT}\left(z_i^* e \rho_e j + kT \frac{\partial \ln N_i}{\partial x} \right) \qquad \text{Eq. 5-3}$$

where the first term represents atomic flux induced by electrical current and the second term corresponds to atomic flux driven by composition gradient. D_i is the diffusion coefficient, N_i is the mole fraction of each element, T is the temperature, k is the Boltzman constant, z_i^* is the effective charge of atom, e is the charge per electron, ρ_e represents material electrical resistivity and j is the current density. To compare the atomic diffusion in these three welding conditions, the outside boundary of the hook structure, marked as region 2 in Figure 5-21 (a), is further examined with a higher magnification using SEM. The results are shown in Figure 5-22.

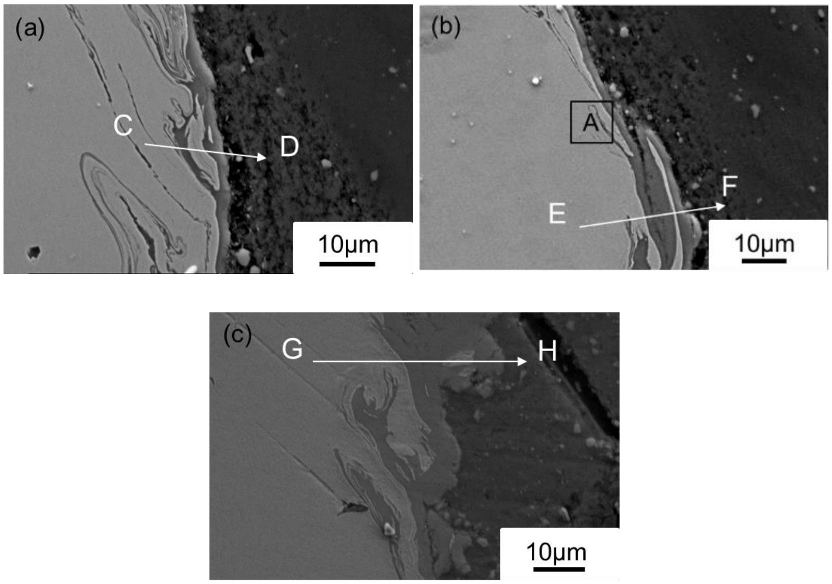

Figure 5-22. Enlarged cross section view of Fe/Al interface (a) without current (b) with direct current (c) with pulses

Under the non-electrically assisted condition, a certain amount of aluminum penetrates into the steel matrix and forms an intercalation structure as shown in Figure 5-22 (a). This can be explained based on the mechanisms shown in Figure 5-19 that the aluminum is embedded under a new layer of the extruded steel. After the application of the direct current, the steel matrix is relatively intact. The penetration depth of aluminum into steel is much smaller, marked out as region A in Figure 5-22(b). However, the thickness of the IMC layer at the Al-Fe interface increases. These observations can be explained based on the hook formation mechanisms illustrated in Figure 5-19. The additional Joule heat from electrical current enhances the flow of steel materials and softens the extruded steel, which ensures a smoother fusion between the newly extruded steel and the existing hook and restrains the penetration of aluminum. On the other hand, the associated higher temperature promotes reaction between aluminum and steel and accelerates the growth of the IMC layer.

The Al-Fe interface under the pulse condition is shown in Figure 5-22(c), the observations are similar to those obtained from the direct current condition. The penetration depth of aluminum into the steel matrix is smaller compared with the conventional FSSW process. On the other hand, the thickness of the IMC layer is even larger than that under the direct current condition. This indicates that the electro-plastic effect is more phenomenal from electrical pulses compared with that from the direct current with the same amount of total energy input. Diffusion rates of the atoms are increased due to the electro-plastic effect at the pulse condition, which forms a thicker IMC layer. In return, the thicker IMC layer accordingly results in a lower joint strength.

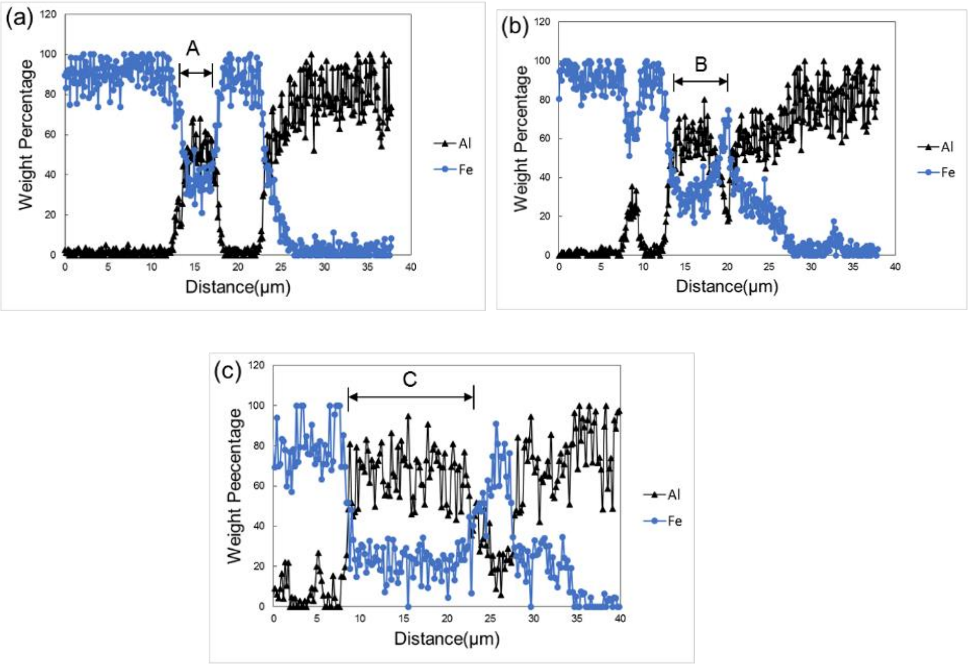

Figure 5-23. Corresponding EDS line test results along Fe/Al interface (a) without current (b) with direct current (c) with pulses

To compare the compositions at the Fe/Al interface between conventional FSSW and electrically assisted conditions, EDS line analysis is performed. The test path is from point C to point D in Figure 5-22(a), point E to point F in Figure 5-22(b) and G to H in Figure 5-22(c). Corresponding results are provided in Figure 5-23. As marked out as regions A, B and C for all these three conditions, the compositions are relatively parallel horizontal lines, indicating the formation of IMCs at the Fe/Al interface. This is also consistent with the layer of grey color on the SEM images. In Figure 5-23 (a), the Fe element composition goes back to around 100% after region A. Referring back to Figure 5-22 (a), a small steel island can be observed between points C and D, surrounded by the grey layer of possible intermetallic. After passing this region, the Fe composition gradually goes down while that of Al increases. This indicates an inter-diffusion layer of Al-Fe mixture. However, it should be noticed that the resolution of EDS is limited and tends to average the composition based on the excitation volume. The EDS spatial resolution can be determined based on the Castaing's formula as the followings[160, 161]:

$$\mathrm{Z}_m = 0.033\left(E_0^{1.7} - E_c^{1.7}\right)\frac{A}{\rho Z} \qquad \text{Eq. 5-4}$$

$$\mathrm{D} = 2.2\frac{0.187Z^{2/3}}{1+0.187Z^{2/3}}Z_m \qquad \text{Eq. 5-5}$$

Where Z_m is the depth of the X-ray excited volume in um, E_0 is the acceleration voltage in keV, E_c is the critical excitation voltage in keV and ρ is the material density in kg/m3, Z is the atomic number, A is the atomic mass, D is the spatial resolution in um. The acceleration voltage used in the EDS analysis is 15keV. Based on this calculation, the EDS spatial resolution for Fe is around 0.92um while that for Al is 2.78um. Accordingly, the IMC layer with thickness of less than 1um is hardly distinguishable as a horizontal line in the EDS composition analysis.

Similar patterns can be observed in Figures 5-23 (b) and (c) as well. After the IMC regions B and C, the Fe composition increases a little. Both of which can be referred to the SEM images in Figure 5-22, where the EDS analysis line passes through the isolated small piece of Fe. After that, the Al-Fe composition then gradually changes suggesting an inter diffusion transition layer with Al-Fe mixture. Still, this could also be induced by the insufficient resolution of EDS.

The compositions of the IMC layer are different under the three conditions. In the standard FSSW process in Figure 5-23 (a), the IMC layer has a thickness of around 2 μm and the corresponding weight percentage of aluminum is around 42%. After the application of the direct current, the IMC thickness increases to 6μm, and the weight percentage of aluminum is approximately 60%, as shown in Figure 5-23 (b). For the pulse condition, the IMC thickness is 15μm and the percentage of the aluminum is 60%, which is approximately equal to that of the DC condition. This indicates that the compositions of the IMC layer from the direct and pulsed current assisted processes are the same. But the electro-plastic effect increases the diffusion rate and results in a thicker IMC layer.

At the inside of the hook, the aluminum is heavily mixed with steel under a large compression force from the tool shoulder in the conventional FSSW joint, as shown in Figure 5-21. The corresponding position from the electrically assisted condition is shown in Figure 5-24. It can be observed that the amount of aluminum mixed with steel is relatively smaller. This phenomenon can be explained similarly to the aluminum flow behavior at the TMAZ: The electrical current enhances the flow of aluminum materials that are located between the tool shoulder and hook. A larger fraction of aluminum is therefore capable of flowing outward, which results in less aluminum mixing with the inner side of the hook. The reduced mixing between aluminum and steel can also lead to a smaller plunge force.

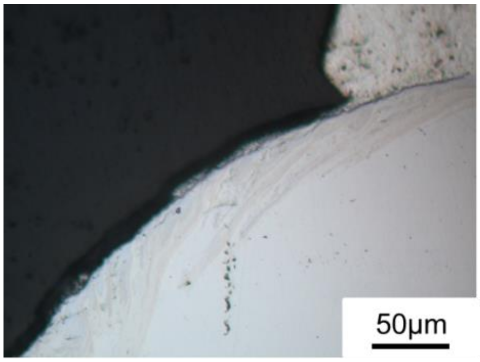

Figure 5-24**.** Cross-section view at the left side of hook (560A DC)

5.4 Conclusions

This chapter studies a hybrid friction stir resistance spot welding process for joining aluminum alloy 6061-T6 to TRIP 780 steel. An effective electrically assisted FSSW experimental system has been developed, which enables a high density electrical current in the weld zone with the tool passively involved in the circuit. Compared with the conventional RSW process, the applied current is lower and avoids bulk melting. Compared with conventional FSSW process, the axial plunge force reduces by 12.84% and the joint strength increases by 43% with the application of the direct current. The electro-plastic effect, which is the direct material softening effect from electrical current, is studied by comparing direct and pulsed current conditions, where the total amount of energy input is equal. Regardless of the form of the electrical current, the force reduction is the same, which indicates the electro-plastic effect is insignificant and Joule heating is the dominant material softening mechanism during the FSSW process. Microstructure analysis on the joint cross section reveals that the electrical current enhances the material flow of aluminum and a more uniform hook is generated at the Fe/Al interface. The penetration of aluminum into steel is smaller and the intercalation structure is less obvious. However, the diffusion rate is increased with the electrical current due to the electro-plastic effect and an IMC layer with larger thickness is observed. The thickness of the IMC layer is larger in the pulsed condition compared with the direct current condition.

CHAPTER 6
CONCLUSIONS AND FUTURE WORK

6.1 Conclusions

This research focuses on improving the friction stir spot welding process of aluminum 6061 to TRIP 780 steel. Three major parts have been accomplished through this research, including the study of fundamental working mechanisms of the FSSW of dissimilar materials, modeling the FSSW process and introducing innovative FSSW methods to improve the joint quality. The major accomplishments are summarized as the followings:

1. The friction stir spot welding has been shown to be applicable for joining aluminum alloy 6061 to TRIP 780 steel. Hook feature is observed in the weld microstructure, which serves as the mechanical interlocking between steel and aluminum alloy. The cross nugget failure is identified as the only observed failure mode. In addition, DOE results show that the dwell time is a critical process parameter in determining the joint strength when comparing to other parameters.

2. Process models for FSSW of dissimilar materials are developed, which include: (a) Coupled Eulerian-Lagrangian (CEL) approach to solve the FSSW problem with severe mesh distortion of the base material; (b) Penalty method to calculate the interaction force between the Lagrangian body and the Eulerian elements; (c) Mixture theory to account for the dissimilar materials involved in the weld zone. The models reveal hook formation mechanisms and the calculated force and thermal history agrees with the experimental data

3. An innovative keyhole refilled FSSW shows to effectively eliminate the keyhole defect associated with the conventional FSSW process. Significant improvements of aluminum to steel joint properties are achieved, including higher strength, better ductility and higher reliability. Underlying principles of these enhancements are related to the refilled keyhole along with the increased bonding area from the circular motion of the tool pin after the conventional FSSW step.

4. Electrically assisted FSSW system has been developed, which can provide high-density electrical current in the stirring zone. Compared with conventional FSSW of aluminum alloy 6061 to TRIP 780 steel, the electrically assisted FSSW reduces the overall axial plunge force by 12.84% and the joint strength increases by 43%. Experimental results also indicate that the electro-plastic effect is insignificant and Joule heating is the dominant softening mechanism during the FSSW process.

6.2 Future Work

The developed FSSW process is proved to be reliable to join the dissimilar materials, which can be extended to other dissimilar materials welding. The keyhole refilled method and the electrical assisted FSSW shows improvements on the FSSW process. However, overcoming other shortages of the FSSW is still necessary, the possible directions can be listed as followings:

1. The IMC formed during the welding process plays an important role in determining the joint strength. Bozzi et al.[40] welded the Al6061 with IF steel, it was found that most of the IMCs were formed at the interface between the steel and aluminum. The authors mentioned that the IMC layer thickness increased with the rotation speed and the penetration depth. They also pointed out that the IMC layer was necessary to improve the weld strength. On the other hand, a larger IMC

thickness will deteriorate the joint strength. The relationship between the process parameters and the amount of IMCs still remains unknown. The corresponding effects of the IMCs on the joint strength are also a promising research direction. Regarding the welding process, it takes much longer time than the RSW, decreasing the welding time and maintaining the high joint strength will be a potential topic.

2. The model developed in this research can be extended to the tool design optimization. As the tool geometry is essential in determining the material flow during the welding process, which in return affects the joint strength. Tool geometries can be incorporated in the model to investigate the possible improvement in the tool geometry design.

3. Regarding the keyhole refilled FSSW, a simple solution is provided for refilling the keyhole without requiring special machine or multiple FSSW tools. However, several aspects should be further investigated. First, the effects of the welding parameters on the joint strength are unclear, including the rotation speed, plunge speed, plunge depth, traveling speed and other related process parameters. Second, the new keyhole is also a major defect for the joint quality. One of the possible improvements is shown in Figure 6-1. A tilt angle has been introduced for the welding tool, besides, the welding tool traverses away from the welding region at the final stage, which can eliminate the final keyhole defect from the original keyhole refilled process. Third, some defects are generated on the welding surface, which is undesirable. Eliminating these defects will result in a better joint strength. Finally, a spiral retreat motion has been conducted during the welding process, which is based on the purpose of eliminating the keyhole when the tool retreats. Figure 6-2 shows the joints of different retreat modes in the welding process. However, there is no improvement in the joint strength. Improvements such as refining the surface finish and finding the optimal retreating process should also be a potential topic. Finally, external heat can be applied

for the weld to reach the same temperature profile during the refilling process, the microstructure of the hook and aluminum might show differences when comparing to the key hole refilled FSSW process.

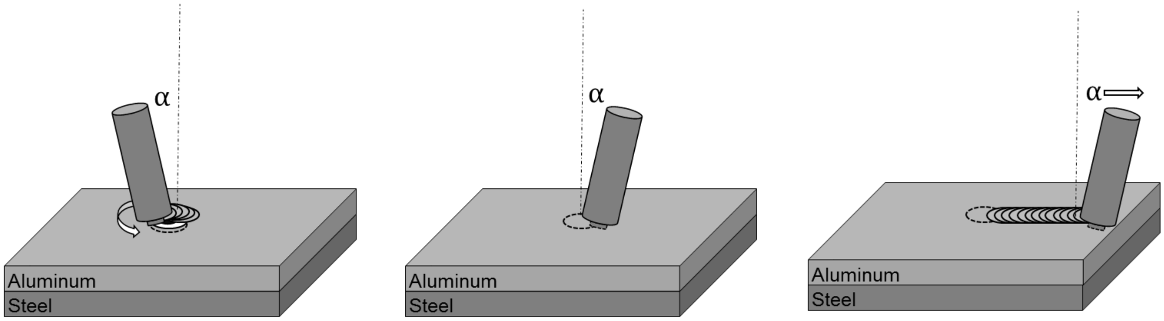

Figure 6-1 Illustration of the improved key-hole refilled FSSW process

Figure 6-2 Illustrations of keyhole refilled FSSW with spiral retreat configuration

4. For the dissimilar material welding process. Many researches have been done to investigate the possibility of welding the aluminum to polymer. Amancio-Filho, S. T., et al. [162] performed friction spot joining between magnesium AZ31 and the carbon fiber reinforced poly. In their experimental configuration, the magnesium was placed on the top and the corresponding strength is around 20-28MPa. Goushegir, S. M. et al.[163] performed the friction spot joining of the AA2024-T3 to the carbon fiber reinforced poly. They found that the carbon fiber was embedded in the deformed aluminum in the nub region and the direct contact between the aluminum and the carbon fibers contributed to the final joint strength. Liu et al.[164] applied

friction stir welding to join the AA6061 to the MC Nylon 6. The aluminum is placed on the top for the welding configuration. The obtained joint strength is around the range of 5-8MPa. To investigate the possibility of applying the FSSW to joining the metal to composite materials, few initial investigations have been conducted. A short carbon fiber reinforced Nylon 6 composite with a weight fraction of fibers of 30% (30% CF Nylon 6) is selected as the base material for the welding process. It has excellent formability and low cost for the mass production [165]. Trial experiments with different combinations of process parameters and welding configurations have been conducted. Figure 6-3 shows the fracture surfaces for the different welding configurations. Figure 6-3 (a) shows the failure surface when the aluminum is placed on the top. As the tool plunges into the aluminum on the top, the excessive heat generated by the tool shoulder melts the aluminum when the tool is at a desired plunge depth. It results in a defect for the joint, which is shown on Figure 6-3 (a). Besides, when the Nylon 6 is placed on the top, the extruded hook cannot generate a strong bonding with the Nylon 6, which also results in a weak joint as indicated by Figure 6-3(b). To make a solid joint, a friction welding process may be a possible welding technology to welding the aluminum to Nylon 6.

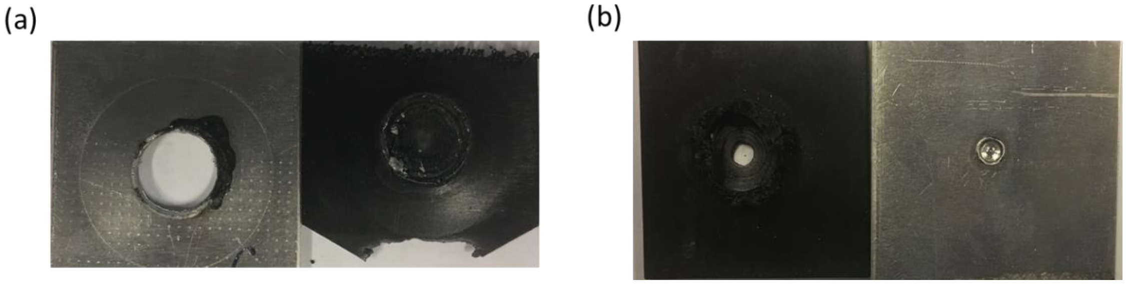

Figure 6-3 Fracture surface of different welding configurations (a) Aluminum on the top (b) Aluminum on the botto

BIBLIOGRAPHY

[1] Badarinarayan, H., Yang, Q., and Zhu, S., 2009, "Effect of tool geometry on static strength of friction stir spot-welded aluminum alloy," International Journal of Machine Tools and Manufacture, 49(2), pp. 142-148.

[2] Ambroziak, A., and Korzeniowski, M., 2010, "Using resistance spot welding for joining aluminium elements in automotive industry," Archives of civil and Mechanical Engineering, 10(1), pp. 5-13.

[3] Hao, M., Osman, K., Boomer, D., and Newton, C., 1996, "Developments in characterization of resistance spot welding of aluminum," Welding Journal-Including Welding Research Supplement, 75(1), pp. 1-4.

[4] Florea, R., Bammann, D., Yeldell, A., Solanki, K., and Hammi, Y., 2013, "Welding parameters influence on fatigue life and microstructure in resistance spot welding of 6061-T6 aluminum alloy," Materials & Design, 45, pp. 456-465.

[5] Lindenburg, R., and Braton, N., 1976, "Aluminum welding, welding and other joining processes," Allyn and Bacon, Inc.

[6] Han, L., Thornton, M., Boomer, D., and Shergold, M., 2010, "Effect of aluminium sheet surface conditions on feasibility and quality of resistance spot welding," Journal of Materials Processing Technology, 210(8), pp. 1076-1082.

[7] Fukumoto, S., Lum, I., Biro, E., Boomer, D., and Zhou, Y., 2003, "Effects of electrode degradation on electrode life in resistance spot welding of aluminum alloy 5182," WELDING JOURNAL-NEW YORK-, 82(11), pp. 307-S.

[8] Florea, R., Solanki, K., Bammann, D., Baird, J., Jordon, J., and Castanier, M., 2012, "Resistance spot welding of 6061-T6 aluminum: Failure loads and deformation," Materials & Design, 34, pp. 624-630.

[9] Han, L., Thornton, M., Li, D., and Shergold, M., 2011, "Effect of governing metal thickness and stack orientation on weld quality and mechanical behaviour of resistance spot welding of AA5754 aluminium," Materials & Design, 32(4), pp. 2107-2114.

[10] Sun, X., Stephens, E. V., and Khaleel, M. A., 2008, "Effects of fusion zone size and failure mode on peak load and energy absorption of advanced high strength steel spot welds under lap shear loading conditions," Engineering Failure Analysis, 15(4), pp. 356-367.

[11] Kuziak, R., Kawalla, R., and Waengler, S., 2008, "Advanced high strength steels for automotive industry," Archives of civil and mechanical engineering, 8(2), pp. 103-117.

[12] Kwon, O., Lee, K. Y., Kim, G. S., and Chin, K. G., 2010, "New trends in advanced high strength steel developments for automotive application," Materials Science Forum, Trans Tech Publ, pp. 136-141.

[13] Matlock, D. K., Speer, J. G., Moor, E. D., and Gibbs, P. J., 2012, "Recent developments in advanced high strength sheet steels for automotive applications: an overview," Jestech, 15(1), pp. 1-12.

[14] Long, X., and Khanna, S. K., 2007, "Fatigue properties and failure characterization of spot welded high strength steel sheet," International journal of fatigue, 29(5), pp. 879-886.

[15] Qiu, R., Iwamoto, C., and Satonaka, S., 2009, "The influence of reaction layer on the strength of aluminum/steel joint welded by resistance spot welding," Materials Characterization, 60(2), pp. 156-159.

[16] Qiu, R., Iwamoto, C., and Satonaka, S., 2009, "Interfacial microstructure and strength of steel/aluminum alloy joints welded by resistance spot welding with cover plate," Journal of Materials processing technology, 209(8), pp. 4186-4193.

[17] Sun, X., Stephens, E. V., Khaleel, M. A., Shao, H., and Kimchi, M., 2004, "Resistance spot welding of aluminum alloy to steel with transition material-from process to performance-Part I: experimental study," WELDING JOURNAL-NEW YORK-, 83, pp. 188-S.

[18] Qiu, R., Satonaka, S., and Iwamoto, C., 2009, "Effect of interfacial reaction layer continuity on the tensile strength of resistance spot welded joints between aluminum alloy and steels," Materials & Design, 30(9), pp. 3686-3689.

[19] Mishra, R. S., and Ma, Z., 2005, "Friction stir welding and processing," Materials Science and Engineering: R: Reports, 50(1), pp. 1-78.

[20] Rhodes, C., Mahoney, M., Bingel, W., Spurling, R., and Bampton, C., 1997, "Effects of friction stir welding on microstructure of 7075 aluminum," Scripta materialia, 36(1), pp. 69-75.

[21] Zhang, Z., Yang, X., Zhang, J., Zhou, G., Xu, X., and Zou, B., 2011, "Effect of welding parameters on microstructure and mechanical properties of friction stir spot welded 5052 aluminum alloy," Materials & Design, 32(8-9), pp. 4461-4470.

[22] Freeney, T., Sharma, S., and Mishra, R., 2006, "Effect of welding parameters on properties of 5052 Al friction stir spot welds," No. 0148-7191, SAE Technical Paper.

[23] Badarinarayan, H., Shi, Y., Li, X., and Okamoto, K., 2009, "Effect of tool geometry on hook formation and static strength of friction stir spot welded aluminum 5754-O sheets," International Journal of Machine Tools and Manufacture, 49(11), pp. 814-823.

[24] Pathak, N., Bandyopadhyay, K., Sarangi, M., and Panda, S. K., 2013, "Microstructure and mechanical performance of friction stir spot-welded aluminum-5754 sheets," Journal of materials engineering and performance, 22(1), pp. 131-144.

[25] Tozaki, Y., Uematsu, Y., and Tokaji, K., 2007, "Effect of tool geometry on microstructure and static strength in friction stir spot welded aluminium alloys," International Journal of Machine Tools and Manufacture, 47(15), pp. 2230-2236.

[26] Wang, D.-A., and Lee, S.-C., 2007, "Microstructures and failure mechanisms of friction stir spot welds of aluminum 6061-T6 sheets," Journal of Materials Processing Technology, 186(1), pp. 291-297.

[27] Wang, D.-A., and Chen, C.-H., 2009, "Fatigue lives of friction stir spot welds in aluminum 6061-T6 sheets," journal of materials processing technology, 209(1), pp. 367-375.

[28] Awang, M., and Mucino, V. H., 2010, "Energy generation during friction stir spot welding (FSSW) of Al 6061-T6 plates," Materials and Manufacturing Processes, 25(1-3), pp. 167-174.

[29] Rodrigues, D., Loureiro, A., Leitao, C., Leal, R., Chaparro, B., and Vilaça, P., 2009, "Influence of friction stir welding parameters on the microstructural and mechanical properties of AA 6016-T4 thin welds," Materials & Design, 30(6), pp. 1913-1921.

[30] Shen, Z., Yang, X., Yang, S., Zhang, Z., and Yin, Y., 2014, "Microstructure and mechanical properties of friction spot welded 6061-T4 aluminum alloy," Materials & Design (1980-2015), 54, pp. 766-778.

[31] Mitlin, D., Radmilovic, V., Pan, T., Chen, J., Feng, Z., and Santella, M., 2006, "Structure–properties relations in spot friction welded (also known as friction stir spot welded) 6111 aluminum," Materials Science and Engineering: A, 441(1), pp. 79-96.

[32] Su, J.-Q., Nelson, T., Mishra, R., and Mahoney, M., 2003, "Microstructural investigation of friction stir welded 7050-T651 aluminium," Acta materialia, 51(3), pp. 713-729.

[33] Shen, Z., Yang, X., Zhang, Z., Cui, L., and Li, T., 2013, "Microstructure and failure mechanisms of refill friction stir spot welded 7075-T6 aluminum alloy joints," Materials & design, 44, pp. 476-486.

[34] Karthikeyan, R., and Balasubramanian, V., 2010, "Predictions of the optimized friction stir spot welding process parameters for joining AA2024 aluminum alloy using RSM," The International Journal of Advanced Manufacturing Technology, 51(1-4), pp. 173-183.

[35] Yuan, W., Mishra, R. S., Webb, S., Chen, Y., Carlson, B., Herling, D., and Grant, G., 2011, "Effect of tool design and process parameters on properties of Al alloy 6016 friction stir spot welds," Journal of Materials Processing Technology, 211(6), pp. 972-977.

[36] Bilici, M. K., 2012, "Application of Taguchi approach to optimize friction stir spot welding parameters of polypropylene," Materials & Design, 35, pp. 113-119.

[37] Tozaki, Y., Uematsu, Y., and Tokaji, K., 2007, "Effect of processing parameters on static strength of dissimilar friction stir spot welds between different aluminium alloys," Fatigue & Fracture of Engineering Materials & Structures, 30(2), pp. 143-148.

[38] Bilici, M. K., and Yükler, A. I., 2012, "Influence of tool geometry and process parameters on macrostructure and static strength in friction stir spot welded polyethylene sheets," Materials & Design, 33, pp. 145-152.

[39] Gerlich, A., Su, P., Yamamoto, M., and North, T. H., 2007, "Effect of welding parameters on the strain rate and microstructure of friction stir spot welded 2024 aluminum alloy," Journal of Materials Science, 42(14), pp. 5589-5601.

[40] Bozzi, S., Helbert-Etter, A., Baudin, T., Criqui, B., and Kerbiguet, J., 2010, "Intermetallic compounds in Al 6016/IF-steel friction stir spot welds," Materials Science and Engineering: A, 527(16), pp. 4505-4509.

[41] Liyanage, T., Kilbourne, J., Gerlich, A. P., and North, T. H., 2009, "Joint formation in dissimilar Al alloy/steel and Mg alloy/steel friction stir spot welds," Science and Technology of Welding and Joining, 14(6), pp. 500-508.

[42] Taban, E., Gould, J. E., and Lippold, J. C., 2010, "Dissimilar friction welding of 6061-T6 aluminum and AISI 1018 steel: Properties and microstructural characterization," Materials & design, 31(5), pp. 2305-2311.

[43] Chen, Y. C., Gholinia, A., and Prangnell, P. B., 2012, "Interface structure and bonding in abrasion circle friction stir spot welding: A novel approach for rapid welding aluminium alloy to steel automotive sheet," Materials Chemistry and Physics, 134(1), pp. 459-463.

[44] Da Silva, A., Aldanondo, E., Alvarez, P., Arruti, E., and Echeverria, A., 2010, "Friction stir spot welding of AA 1050 Al alloy and hot stamped boron steel (22MnB5)," Science and Technology of Welding and Joining, 15(8), pp. 682-687.

[45] Fereiduni, E., Movahedi, M., and Kokabi, A., 2015, "Aluminum/steel joints made by an alternative friction stir spot welding process," Journal of Materials Processing Technology, 224, pp. 1-10.

[46] Mandal, S., Rice, J., and Elmustafa, A. A., 2008, "Experimental and numerical investigation of the plunge stage in friction stir welding," Journal of Materials Processing Technology, 203(1-3), pp. 411-419.

[47] Schmidt, H., and Hattel, J., 2005, "A local model for the thermomechanical conditions in friction stir welding," Modelling and Simulation in Materials Science and Engineering, 13(1), pp. 77-93.

[48] Zhang, Z., and Chen, J., 2008, "The simulation of material behaviors in friction stir welding process by using rate-dependent constitutive model," Journal of materials science, 43(1), pp. 222-232.
[49] Al-Badour, F., Merah, N., Shuaib, A., and Bazoune, A., 2013, "Coupled Eulerian Lagrangian finite element modeling of friction stir welding processes," Journal of Materials Processing Technology, 213(8), pp. 1433-1439.
[50] Qiu, G., Henke, S., and Grabe, J., 2011, "Application of a Coupled Eulerian–Lagrangian approach on geomechanical problems involving large deformations," Computers and Geotechnics, 38(1), pp. 30-39.
[51] Smojver, I., and Ivančević, D., 2011, "Bird strike damage analysis in aircraft structures using Abaqus/Explicit and coupled Eulerian Lagrangian approach," Composites Science and Technology, 71(4), pp. 489-498.
[52] Qiu, G., Henke, S., and Grabe, J., 2009, "Applications of Coupled Eulerian-Lagrangian method to geotechnical problems with large deformations," Proceeding of SIMULIA customer conference, pp. 420-435.
[53] Guilkey, J. E., Harman, T., Xia, A., Kashiwa, B., and McMurtry, P., 2003, "An Eulerian-Lagrangian approach for large deformation fluid structure interaction problems, Part 1: algorithm development," WIT Transactions on The Built Environment, 71.
[54] Hamann, T., Qiu, G., and Grabe, J., 2015, "Application of a Coupled Eulerian–Lagrangian approach on pile installation problems under partially drained conditions," Computers and Geotechnics, 63, pp. 279-290.
[55] Aota, K., Okamura, H., and Sato, K., 2004, "Friction stir welding method and apparatus for reducing the friction force," EP1430986.
[56] Mach, M., Schülbe, H., and Nacke, B., 2008, "Investigation and design of induction assisted welding processes," Przegląd Elektrotechniczny, 84, pp. 228-231.
[57] Song, K. H., Tsumura, T., and Nakata, K., 2009, "Development of microstructure and mechanical properties in laser-FSW hybrid welded Inconel 600," Materials transactions, 50(7), pp. 1832-1837.
[58] Sun, Y., Shen, J., Morisada, Y., and Fujii, H., 2014, "Spot friction stir welding of low carbon steel plates preheated by high frequency induction," Materials & Design (1980-2015), 54, pp. 450-457.
[59] Park, K., 2009, "Development and analysis of ultrasonic assisted friction stir welding process," University of Michigan.
[60] Ruilin, L., Diqiu, H., Luocheng, L., Shaoyong, Y., and Kunyu, Y., 2014, "A study of the temperature field during ultrasonic-assisted friction-stir welding," The International Journal of Advanced Manufacturing Technology, 73(1-4), pp. 321-327.
[61] Liu, X., Lan, S., and Ni, J., 2015, "Electrically assisted friction stir welding for joining Al 6061 to TRIP 780 steel," Journal of Materials Processing Technology, 219, pp. 112-123.
[62] Venukumar, S., Yalagi, S., and Muthukumaran, S., 2013, "Comparison of microstructure and mechanical properties of conventional and refilled friction stir spot welds in AA 6061-T6 using filler plate," Transactions of Nonferrous Metals Society of China, 23(10), pp. 2833-2842.
[63] Itapu, S., and Muci-Küchler, K., 2006, "Visualization of Material Flow in the Refill Friction Stir Spot Welding Process," No. 0148-7191, SAE Technical Paper.
[64] Tier, M., Rosendo, T., dos Santos, J., Huber, N., Mazzaferro, J., Mazzaferro, C., and Strohaecker, T., 2013, "The influence of refill FSSW parameters on the microstructure and shear

strength of 5042 aluminium welds," Journal of materials processing technology, 213(6), pp. 997-1005.
[65] Venukumar, S., Yalagi, S., Muthukumaran, S., and Kailas, S., 2014, "Static shear strength and fatigue life of refill friction stir spot welded AA 6061-T6 sheets," Science and Technology of Welding and Joining, 19(3), pp. 214-223.
[66] Li, Z., Gao, S., Ji, S., Yue, Y., and Chai, P., 2016, "Effect of rotational speed on microstructure and mechanical properties of refill friction stir spot welded 2024 al alloy," Journal of Materials Engineering and Performance, 25(4), pp. 1673-1682.
[67] Aota, K., and Ikeuchi, K., 2009, "Development of friction stir spot welding using rotating tool without probe and its application to low-carbon steel plates," Welding International, 23(8), pp. 572-580.
[68] Tozaki, Y., Uematsu, Y., and Tokaji, K., 2010, "A newly developed tool without probe for friction stir spot welding and its performance," Journal of Materials Processing Technology, 210(6-7), pp. 844-851.
[69] Bakavos, D., Chen, Y., Babout, L., and Prangnell, P., 2011, "Material interactions in a novel pinless tool approach to friction stir spot welding thin aluminum sheet," Metallurgical and Materials Transactions A, 42(5), pp. 1266-1282.
[70] Sun, Y., Fujii, H., Takaki, N., and Okitsu, Y., 2012, "Microstructure and mechanical properties of mild steel joints prepared by a flat friction stir spot welding technique," Materials & Design, 37, pp. 384-392.
[71] Lathabai, S., Painter, M. J., Cantin, G. M. D., and Tyagi, V. K., 2006, "Friction spot joining of an extruded Al–Mg–Si alloy," Scripta Materialia, 55(10), pp. 899-902.
[72] Lakshminarayanan, A. K., Annamalai, V. E., and Elangovan, K., 2015, "Identification of optimum friction stir spot welding process parameters controlling the properties of low carbon automotive steel joints," Journal of Materials Research and Technology, 4(3), pp. 262-272.
[73] Aldanondo, E., Taboada, A., Arruti, E., Alvarez, P., and Echeverria, A., 2014, "Friction stir spot welding of DP1200 steel," Proceedings of the 1st International Joint Symposium on Joining and Welding: Osaka, Japan, 6-8 November 2013, Woodhead Publishing, p. 179.
[74] Bilici, M. K., Yükler, A. İ., and Kurtulmuş, M., 2011, "The optimization of welding parameters for friction stir spot welding of high density polyethylene sheets," Materials & Design, 32(7), pp. 4074-4079.
[75] Bozkurt, Y., Salman, S., and Çam, G., 2013, "Effect of welding parameters on lap shear tensile properties of dissimilar friction stir spot welded AA 5754-H22/2024-T3 joints," Science and Technology of Welding and Joining, 18(4), pp. 337-345.
[76] Rao, H., Yuan, W., and Badarinarayan, H., 2015, "Effect of process parameters on mechanical properties of friction stir spot welded magnesium to aluminum alloys," Materials & Design (1980-2015), 66, pp. 235-245.
[77] Sato, Y., Shiota, A., Kokawa, H., Okamoto, K., Yang, Q., and Kim, C., 2010, "Effect of interfacial microstructure on lap shear strength of friction stir spot weld of aluminium alloy to magnesium alloy," Science and Technology of Welding and Joining, 15(4), pp. 319-324.
[78] Chowdhury, S., Chen, D., Bhole, S., Cao, X., and Wanjara, P., 2012, "Lap shear strength and fatigue life of friction stir spot welded AZ31 magnesium and 5754 aluminum alloys," Materials Science and Engineering: A, 556, pp. 500-509.
[79] Jana, S., Hovanski, Y., and Grant, G. J., 2010, "Friction stir lap welding of magnesium alloy to steel: a preliminary investigation," Metallurgical and Materials Transactions A, 41(12), pp. 3173-3182.

[80] Sun, Y. F., Fujii, H., Takaki, N., and Okitsu, Y., 2013, "Microstructure and mechanical properties of dissimilar Al alloy/steel joints prepared by a flat spot friction stir welding technique," Materials & Design, 47, pp. 350-357.
[81] Figner, M. S. G., Vallant, R., Weinberger, M. S. T., Enzinger, N., Schröttner, H., and Paśič, H., 2009, "Friction Stir Spot Welds between Aluminium and Steel automotive sheets: Influence of welding parameters on mechanical properties and microstructure," Welding in the World, 53(1-2), pp. R13-R23.
[82] Liu, X., Lan, S., and Ni, J., 2014, "Analysis of process parameters effects on friction stir welding of dissimilar aluminum alloy to advanced high strength steel," Materials & Design, 59, pp. 50-62.
[83] Hong, S. H., Sung, S.-J., and Pan, J., 2015, "Failure Mode and Fatigue Behavior of Dissimilar Friction Stir Spot Welds in Lap-Shear Specimens of Transformation-Induced Plasticity Steel and Hot-Stamped Boron Steel Sheets," Journal of Manufacturing Science and Engineering, 137(5), p. 051023.
[84] Baskoro, A. S., Suwarsono, Habibullah, M. D., Arvay, Z., Kiswanto, G., Winarto, and Chen, Z. W., 2015, "Effects of Dwell-Time and Plunge Speed during Micro Friction Stir Spot Welding on Mechanical Properties of Thin Aluminum A1100 Welds," Applied Mechanics and Materials, 758, pp. 29-34.
[85] Liu, X., Lan, S., and Ni, J., 2013, "Experimental Study of Electro-Plastic Effect on Advanced High Strength Steels," Materials Science and Engineering: A, 582, pp. 211-218.
[86] Bozzi, S., Helbert-Etter, A. L., Baudin, T., Criqui, B., and Kerbiguet, J. G., 2010, "Intermetallic compounds in Al 6016/IF-steel friction stir spot welds," Materials Science and Engineering: A, 527(16-17), pp. 4505-4509.
[87] Ozaki, H., and Kutsuna, M., 2012, Dissimilar Metal Joining of Zinc Coated Steel and Aluminum Alloy by Laser Roll Welding, INTECH Open Access Publisher.
[88] Ozaki, H., Kutsuna, M., Nakagawa, S., and Miyamoto, K., 2010, "Laser roll welding of dissimilar metal joint of zinc coated steel to aluminum alloy," Journal of Laser Applications, 22(1), pp. 1-6.
[89] Bozkurt, Y., and Bilici, M. K., 2013, "Application of Taguchi approach to optimize of FSSW parameters on joint properties of dissimilar AA2024-T3 and AA5754-H22 aluminum alloys," Materials & Design, 51, pp. 513-521.
[90] Fratini, L., Barcellona, A., Buffa, G., and Palmeri, D., 2007, "Friction stir spot welding of AA6082-T6: influence of the most relevant process parameters and comparison with classic mechanical fastening techniques," Proceedings of the Institution of Mechanical Engineers, Part B: Journal of Engineering Manufacture, 221(7), pp. 1111-1118.
[91] Nandan, R., Roy, G. G., Lienert, T. J., and Debroy, T., 2007, "Three-dimensional heat and material flow during friction stir welding of mild steel," Acta Materialia, 55(3), pp. 883-895.
[92] Zhu, X., and Chao, Y., 2004, "Numerical simulation of transient temperature and residual stresses in friction stir welding of 304L stainless steel," Journal of materials processing technology, 146(2), pp. 263-272.
[93] Cho, H.-H., Hong, S.-T., Roh, J.-H., Choi, H.-S., Kang, S. H., Steel, R. J., and Han, H. N., 2013, "Three-dimensional numerical and experimental investigation on friction stir welding processes of ferritic stainless steel," Acta Materialia, 61(7), pp. 2649-2661.
[94] Chiumenti, M., Cervera, M., de Saracibar, C. A., and Dialami, N., 2013, "Numerical modeling of friction stir welding processes," Computer methods in applied mechanics and engineering, 254, pp. 353-369.

[95] Kim, D., Badarinarayan, H., Kim, J. H., Kim, C., Okamoto, K., Wagoner, R. H., and Chung, K., 2010, "Numerical simulation of friction stir butt welding process for AA5083-H18 sheets," European Journal of Mechanics - A/Solids, 29(2), pp. 204-215.
[96] Jamshidi Aval, H., Serajzadeh, S., and Kokabi, A. H., 2011, "Experimental and theoretical evaluations of thermal histories and residual stresses in dissimilar friction stir welding of AA5086-AA6061," The International Journal of Advanced Manufacturing Technology, 61(1-4), pp. 149-160.
[97] Awang, M., Mucino, V., Feng, Z., and David, S., 2005, "Thermo-mechanical modeling of friction stir spot welding (FSSW) process: use of an explicit adaptive meshing scheme," SAE 2005 World Congress, Apr, Citeseer.
[98] Zhang, H., Zhang, Z., and Chen, J., 2007, "3D modeling of material flow in friction stir welding under different process parameters," Journal of Materials Processing Technology, 183(1), pp. 62-70.
[99] Assidi, M., Fourment, L., Guerdoux, S., and Nelson, T., 2010, "Friction model for friction stir welding process simulation: Calibrations from welding experiments," International Journal of Machine Tools and Manufacture, 50(2), pp. 143-155.
[100] Fourment, L., and Guerdoux, S., 2008, "3D numerical simulation of the three stages of Friction Stir Welding based on friction parameters calibration," International Journal of Material Forming, 1, pp. 1287-1290.
[101] Guerdoux, S., and Fourment, L., 2007, "Error estimation and accurate mapping based ALE formulation for 3D simulation of friction stir welding," AIP Conference Proceedings, AIP, pp. 185-190.
[102] Schmidt, H. N. B., and Hattel, J., 2004, "Modelling thermomechanical conditions at the tool/matrix interface in Friction Stir Welding," 5th International Friction Stir Welding Symposium, The Welding Institute.
[103] Zhang, Z., and Zhang, H., 2009, "Numerical studies on controlling of process parameters in friction stir welding," Journal of materials processing technology, 209(1), pp. 241-270.
[104] Zhang, H., Zhang, Z., and Chen, J., 2005, "The finite element simulation of the friction stir welding process," Materials Science and Engineering: A, 403(1), pp. 340-348.
[105] Guerdoux, S., and Fourment, L., 2009, "A 3D numerical simulation of different phases of friction stir welding," Modelling and simulation in materials science and engineering, 17(7), p. 075001.
[106] Zhang, Z., and Zhang, H., 2008, "A fully coupled thermo-mechanical model of friction stir welding," The International Journal of Advanced Manufacturing Technology, 37(3), pp. 279-293.
[107] Liu, X., Lan, S., and Ni, J., 2015, "Thermal Mechanical Modeling of the Plunge Stage During Friction-Stir Welding of Dissimilar Al 6061 to TRIP 780 Steel," Journal of Manufacturing Science and Engineering, 137(5), pp. 051017-051017.
[108] Benson, D., 1995, "A multi-material Eulerian formulation for the efficient solution of impact and penetration problems," Computational Mechanics, 15(6), pp. 558-571.
[109] Benson, D. J., 1997, "A mixture theory for contact in multi-material Eulerian formulations," Computer methods in applied mechanics and engineering, 140(1), pp. 59-86.
[110] Benson, D. J., and Okazawa, S., 2004, "Contact in a multi-material Eulerian finite element formulation," Computer methods in applied mechanics and engineering, 193(39), pp. 4277-4298.

[111] Brown, K. H., Burns, S. P., and Christon, M. A., 2002, "Coupled Eulerian-Lagrangian methods for earth penetrating weapon applications," US Department of Commerce.

[112] Aquelet, N., Souli, M., and Olovsson, L., 2006, "Euler–Lagrange coupling with damping effects: Application to slamming problems," Computer methods in applied mechanics and engineering, 195(1), pp. 110-132.

[113] McGlaun, J. M., Thompson, S., and Elrick, M., 1990, "CTH: a three-dimensional shock wave physics code," International Journal of Impact Engineering, 10(1-4), pp. 351-360.

[114] Awang, M., 2007, Simulation of friction stir spot welding (FSSW) process: study of friction phenomena, ProQuest.

[115] Sanjeev, N., Malik, V., and Hebbar, H. S., 2014, "Effect of Coefficient of Friction in Finite Element Modeling of Friction Stir Welding and its Importance in Manufacturing Process Modeling Applications," International Journal of Applied Science and Engineering Research, 3(4), pp. 755-762.

[116] Gueyffier, D., Li, J., Nadim, A., Scardovelli, R., and Zaleski, S., 1999, "Volume-of-fluid interface tracking with smoothed surface stress methods for three-dimensional flows," Journal of Computational physics, 152(2), pp. 423-456.

[117] Ulysse, P., 2002, "Three-dimensional modeling of the friction stir-welding process," International Journal of Machine Tools and Manufacture, 42(14), pp. 1549-1557.

[118] KISHTA, E. E., Farid, A., and DARRAS, B., 2014, "Nonlinear Finite Element Simulation of Friction Stir Processing of Marine Grade 5083 Aluminum Alloy," Engineering Transactions, 62(4), pp. 313–328.

[119] Hossfeld, M., and Roos, E., 2013, "A new approach to modelling friction stir welding using the CEL method," Advanced Manufacturing Engineering and Technologies NEWTECH 2013 Stockholm, Sweden 27-30 October 2013, p. 179.

[120] Al-Badour, F., Merah, N., Shuaib, A., and Bazoune, A., 2014, "Thermo-mechanical finite element model of friction stir welding of dissimilar alloys," The International Journal of Advanced Manufacturing Technology, 72(5-8), pp. 607-617.

[121] Zhao, Y. Q., Liu, H. J., Chen, S. X., Lin, Z., and Hou, J. C., 2014, "Effects of sleeve plunge depth on microstructures and mechanical properties of friction spot welded alclad 7B04-T74 aluminum alloy," Materials & Design (1980-2015), 62, pp. 40-46.

[122] Reimann, M., Gartner, T., Suhuddin, U., Göbel, J., and dos Santos, J. F., 2016, "Keyhole closure using friction spot welding in aluminum alloy 6061–T6," Journal of Materials Processing Technology, 237, pp. 12-18.

[123] Cao, J. Y., Wang, M., Kong, L., and Guo, L. J., 2016, "Hook formation and mechanical properties of friction spot welding in alloy 6061-T6," Journal of Materials Processing Technology, 230, pp. 254-262.

[124] Rosendo, T., Parra, B., Tier, M., Da Silva, A., Dos Santos, J., Strohaecker, T., and Alcântara, N., 2011, "Mechanical and microstructural investigation of friction spot welded AA6181-T4 aluminium alloy," Materials & design, 32(3), pp. 1094-1100.

[125] Oliveira, P., Amancio-Filho, S., Dos Santos, J., and Hage, E., 2010, "Preliminary study on the feasibility of friction spot welding in PMMA," Materials Letters, 64(19), pp. 2098-2101.

[126] Suhuddin, U., Fischer, V., Kroeff, F., and Dos Santos, J., 2014, "Microstructure and mechanical properties of friction spot welds of dissimilar AA5754 Al and AZ31 Mg alloys," Materials Science and Engineering: A, 590, pp. 384-389.

[127] Suhuddin, U., Fischer, V., and Dos Santos, J., 2013, "The thermal cycle during the dissimilar friction spot welding of aluminum and magnesium alloy," Scripta Materialia, 68(1), pp. 87-90.
[128] Campanelli, L. C., Suhuddin, U. F. H., Antonialli, A. Í. S., dos Santos, J. F., de Alcantara, N. G., and Bolfarini, C., 2013, "Metallurgy and mechanical performance of AZ31 magnesium alloy friction spot welds," Journal of Materials Processing Technology, 213(4), pp. 515-521.
[129] Li, Z., Ji, S., Ma, Y., Chai, P., Yue, Y., and Gao, S., 2016, "Fracture mechanism of refill friction stir spot-welded 2024-T4 aluminum alloy," The International Journal of Advanced Manufacturing Technology, 86(5-8), pp. 1925-1932.
[130] Uematsu, Y., Tokaji, K., Tozaki, Y., Kurita, T., and Murata, S., 2008, "Effect of re-filling probe hole on tensile failure and fatigue behaviour of friction stir spot welded joints in Al–Mg–Si alloy," International Journal of Fatigue, 30(10-11), pp. 1956-1966.
[131] Zhou, L., Liu, D., Nakata, K., Tsumura, T., Fujii, H., Ikeuchi, K., Michishita, Y., Fujiya, Y., and Morimoto, M., 2013, "New technique of self-refilling friction stir welding to repair keyhole," Science and Technology of Welding and Joining, 17(8), pp. 649-655.
[132] Sajed, M., 2016, "Parametric study of two-stage refilled friction stir spot welding," Journal of Manufacturing Processes, 24, pp. 307-317.
[133] Chen, Y., Chen, J., Shalchi Amirkhiz, B., Worswick, M. J., and Gerlich, A. P., 2015, "Microstructures and properties of Mg alloy/DP600 steel dissimilar refill friction stir spot welds," Science and Technology of Welding and Joining, 20(6), pp. 494-501.
[134] Dong, H., Chen, S., Song, Y., Guo, X., Zhang, X., and Sun, Z., 2016, "Refilled friction stir spot welding of aluminum alloy to galvanized steel sheets," Materials & Design, 94, pp. 457-466.
[135] Chen, K., Liu, X., and Ni, J., 2016, "Effects of Process Parameters on Friction Stir Spot Welding of Aluminum Alloy to Advanced High-Strength Steel," ASME 2016 11th International Manufacturing Science and Engineering Conference, American Society of Mechanical Engineers, pp. V001T002A011-V001T002A011.
[136] Tran, V. X., and Pan, J., 2010, "Fatigue behavior of dissimilar spot friction welds in lap-shear and cross-tension specimens of aluminum and steel sheets," International Journal of Fatigue, 32(7), pp. 1167-1179.
[137] Liyanage, T., Kilbourne, J., Gerlich, A., and North, T., 2009, "Joint formation in dissimilar Al alloy/steel and Mg alloy/steel friction stir spot welds," Science and Technology of Welding and Joining, 14(6), pp. 500-508.
[138] Chen, Y., Gholinia, A., and Prangnell, P., 2012, "Interface structure and bonding in abrasion circle friction stir spot welding: a novel approach for rapid welding aluminium alloy to steel automotive sheet," Materials Chemistry and Physics, 134(1), pp. 459-463.
[139] Uematsu, Y., Kakiuchi, T., Tozaki, Y., and Kojin, H., 2012, "Comparative study of fatigue behaviour in dissimilar Al alloy/steel and Mg alloy/steel friction stir spot welds fabricated by scroll grooved tool without probe," Science and Technology of Welding and Joining, 17(5), pp. 348-356.
[140] Sun, Y., Fujii, H., Takaki, N., and Okitsu, Y., 2013, "Microstructure and mechanical properties of dissimilar Al alloy/steel joints prepared by a flat spot friction stir welding technique," Materials & Design, 47, pp. 350-357.

[141] Sun, Y. F., Konishi, Y., Kamai, M., and Fujii, H., 2013, "Microstructure and mechanical properties of S45C steel prepared by laser-assisted friction stir welding," Materials & Design, 47, pp. 842-849.
[142] Chang, W.-S., Rajesh, S. R., Chun, C.-K., and Kim, H.-J., 2011, "Microstructure and Mechanical Properties of Hybrid Laser-Friction Stir Welding between AA6061-T6 Al Alloy and AZ31 Mg Alloy," Journal of Materials Science & Technology, 27(3), pp. 199-204.
[143] Merklein, M., and Giera, A., 2008, "Laser assisted Friction Stir Welding of drawable steel-aluminium tailored hybrids," International Journal of Material Forming, 1(1), pp. 1299-1302.
[144] Kohn, G., Greenberg, Y., Makover, I., and Munitz, A., 2002, "Laser-assisted friction stir welding," Welding journal, 81(2), pp. 46-48.
[145] Campanelli, S. L., Casalino, G., Casavola, C., and Moramarco, V., 2013, "Analysis and comparison of friction stir welding and laser assisted friction stir welding of aluminum alloy," Materials, 6(12), pp. 5923-5941.
[146] Able, N., and Pfefferkorn, F., 2005, "Laser-assisted friction stir lap welding of aluminum," 2005 ASME Summer Heat Transfer Conference, San Francisco, California.
[147] Palm, F., 2004, "Laser supported friction stir welding method," Google Patents.
[148] Daftardar, S., 2009, "Laser assisted friction stir welding: finite volume method and Metaheuristic optimization."
[149] Bang, H.-S., Bang, H.-S., Kim, H.-S., Kim, J.-H., Oh, I.-H., and Ro, C.-S., 2010, "A study on the weldability and mechanical characteristics of dissimilar materials butt joints by laser assisted friction stir welding," Journal of Welding and Joining, 28(6), pp. 70-75.
[150] Fei, X., Jin, X., Ye, Y., Xiu, T., and Yang, H., 2016, "Effect of pre-hole offset on the property of the joint during laser-assisted friction stir welding of dissimilar metals steel and aluminum alloys," Materials Science and Engineering: A, 653, pp. 43-52.
[151] Park, K., Kim, G.-Y., and Ni, J., 2007, "Design and analysis of ultrasonic assisted friction stir welding," ASME 2007 International Mechanical Engineering Congress and Exposition, American Society of Mechanical Engineers, pp. 731-737.
[152] Ahmadnia, M., Seidanloo, A., Teimouri, R., Rostamiyan, Y., and Titrashi, K. G., 2015, "Determining influence of ultrasonic-assisted friction stir welding parameters on mechanical and tribological properties of AA6061 joints," The International Journal of Advanced Manufacturing Technology, 78(9-12), pp. 2009-2024.
[153] Luo, J., Chen, W., and Fu, G., 2014, "Hybrid-heat effects on electrical-current aided friction stir welding of steel, and Al and Mg alloys," Journal of Materials Processing Technology, 214(12), pp. 3002-3012.
[154] Santos, T. G., Miranda, R. M., and Vilaça, P., 2014, "Friction Stir Welding assisted by electrical Joule effect," Journal of Materials Processing Technology, 214(10), pp. 2127-2133.
[155] Briskham, P., Blundell, N., Han, L., Hewitt, R., Young, K., and Boomer, D., 2006, "Comparison of self-pierce riveting, resistance spot welding and spot friction joining for aluminium automotive sheet," No. 0148-7191, SAE Technical Paper.
[156] Perkins, T. A., Kronenberger, T. J., and Roth, J. T., 2007, "Metallic Forging Using Electrical Flow as an Alternative to Warm/Hot Working," Journal of Manufacturing Science and Engineering, 129(1), p. 84.
[157] Siopis, M. S., and Kinsey, B. L., 2010, "Experimental investigation of grain and specimen size effects during electrical-assisted forming," Journal of Manufacturing Science and Engineering, 132(2), p. 021004.

[158] Chen, C.-M., and Chen, S.-W., 1999, "Electric current effects on Sn/Ag interfacial reactions," Journal of electronic materials, 28(7), pp. 902-906.
[159] Chen, S.-W., Chen, C.-M., and Liu, W.-C., 1998, "Electric current effects upon the Sn/Cu and Sn/Ni interfacial reactions," Journal of electronic materials, 27(11), pp. 1193-1199.
[160] Friel, J. J., 1994, X-ray and image analysis in electron microscopy, Princeton Gamma-Tech, Incorporated.
[161] Barkshire, I., Karduck, P., Rehbach, W. P., and Richter, S., 2000, "High-spatial-resolution low-energy electron beam X-ray microanalysis," Microchimica Acta, 132(2), pp. 113-128.
[162] Amancio-Filho, S., Bueno, C., Dos Santos, J., Huber, N., and Hage, E., 2011, "On the feasibility of friction spot joining in magnesium/fiber-reinforced polymer composite hybrid structures," Materials Science and Engineering: A, 528(10), pp. 3841-3848.
[163] Goushegir, S., Dos Santos, J., and Amancio-Filho, S., 2014, "Friction spot joining of aluminum AA2024/carbon-fiber reinforced poly (phenylene sulfide) composite single lap joints: microstructure and mechanical performance," Materials & Design, 54, pp. 196-206.
[164] Liu, F., Liao, J., and Nakata, K., 2014, "Joining of metal to plastic using friction lap welding," Materials & Design (1980-2015), 54, pp. 236-244.
[165] Wang, K., Shriver, D., Li, Y., Banu, M., Hu, S. J., Xiao, G., Arinez, J., and Fan, H.-T., 2017, "Characterization of weld attributes in ultrasonic welding of short carbon fiber reinforced thermoplastic composites," Journal of Manufacturing Processes, 29, pp. 124-132.